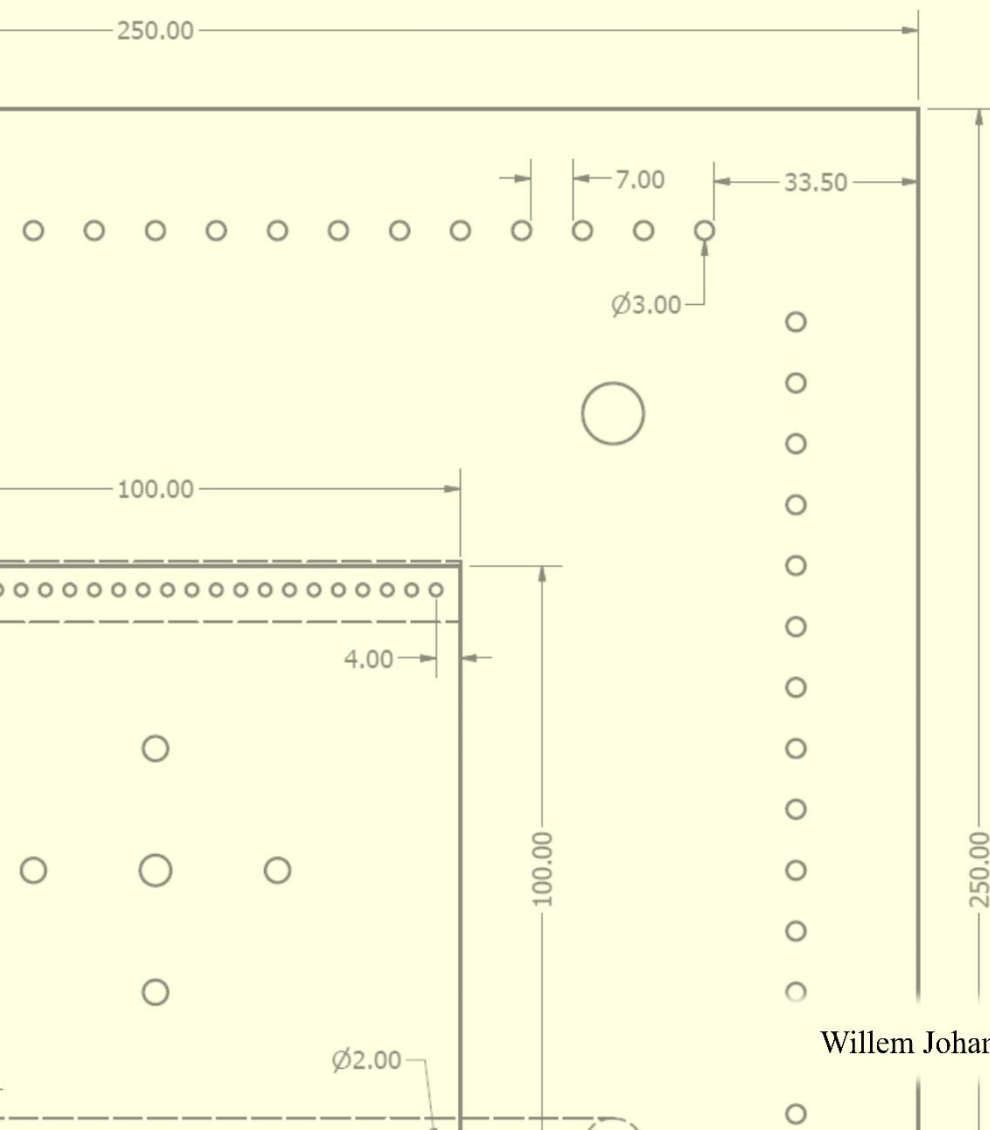


Concentration Gradient Flow Batteries

salinity gradient energy systems as environmentally
benign large scale electrical energy storage



Willem Johannes van Egmond

Concentration Gradient Flow Batteries

salinity gradient energy systems as environmentally benign large
scale electricity storage

Willem Johannes van Egmond

Thesis committee

Promotor

Prof. Dr. C.J.N. Buisman
Professor Biological Recycling Technology
Wageningen University & Research

Co-promotor

Dr. H.V.M. Hamelers
Scientific program director
Wetsus, European centre of excellence for sustainable water technology, Leeuwarden

Other members

Prof. Dr. K.J. Keesman, Wageningen University & Research
Prof. Dr. S.R.A. Kersten, University of Twente
Dr. E. Huerta Martinez, Fujifilm Manufacturing Europe B.V., Tilburg
Dr. G.D.M. Micale, Università degli Studi di Palermo, Italy

This research was conducted under the auspices of the Graduate School SENSE (Socio-Economic and Natural Sciences of the Environment).

Concentration Gradient Flow Batteries

salinity gradient energy systems as environmentally benign large
scale electricity storage

Willem Johannes van Egmond

Thesis

submitted in fulfilment of the requirements for the degree of doctor
at Wageningen University

by the authority of the Rector Magnificus,

Prof. Dr A.P.J. Mol,

in the presence of the

Thesis Committee appointed by the Academic Board

to be defended in public

on Wednesday 11 April 2018

at 11 a.m. in the Aula.

W.J. van Egmond

Concentration Gradient Flow Batteries, salinity gradient energy systems as environmentally benign large scale electricity storage, 162 pages.

PhD thesis, Wageningen University, Wageningen, the Netherlands (2018)

With references, with summary in English

ISBN 978-94-6343-842-1

DOI <https://doi.org/10.18174/444261>

Table of contents

Chapter 1 General introduction	11
1.1 General introduction	12
1.2 Large scale electrical energy storage (EES)	13
1.2.1 Pumped Hydro Storage (PHS).....	17
1.2.2 Compressed Air Energy Storage (CAES).....	18
1.2.3 Li-ion	18
1.2.4 Other energy storage systems	19
1.3 Concentration Gradient Flow Battery (CGFB).....	20
1.3.1 Battery concept	21
1.3.2 Membrane potential	22
1.4 Aim and outline of this thesis	24
1.5 References	27
Chapter 2 The Concentration Gradient Flow Battery as electricity storage system: Technology potential and energy dissipation	33
Abstract	34
2.1 Introduction	34
2.2 Theory	37
2.2.1 Solution characterization	37
2.2.2 Ionic fluxes and properties of ion-exchange membranes.....	37
2.2.3 Membrane potential and internal resistance	39
2.2.4 Energy dissipation mechanisms and system efficiencies.....	40
2.2.5 Concentration gradient flow battery efficiency	41
2.3 Materials and methods.....	41
2.3.1 Concentration gradient flow battery stack design and operation	41
2.3.2 Parameter estimation	42
2.4 Results and Discussion	43
2.4.1 Maximum energy density of the CGFB	43
2.4.2 Parameter estimation	44

2.4.3 Evaluation of the thermodynamic efficiency	46
2.4.4 Flux analysis of the CGFB	47
2.4.5 Influence of different sources of power dissipation at maximum CGFB efficiency.50	
2.5 Conclusions	52
Acknowledgements	53
2.6 References	53
Supplementary information chapter 2.....	55
S2.1 Pitzer model.....	55
S2.2 Salt transport	56
S2.3 Model flow chart summary	57
Chapter 3 Energy efficiency of a Concentration Gradient Flow Battery at elevated temperatures	59
Abstract	60
3.1 Introduction	60
3.2 Theory of a CGFB	62
3.2.1 Energy density	62
3.2.2 Mass transport	62
3.2.3 Power dissipation and (dis)charge efficiency	63
3.3 Materials and methods.....	64
3.1 Experimental setup	64
3.2 Experimental procedure.....	65
3.3 Data analysis.....	65
3.4 Results and Discussion	66
3.4.1 Energy capacity of and ideal CGFB	66
3.4.2 Power dissipation as function of Δm during charge and discharge	66
3.4.3 Charge efficiency and discharge efficiency as function of Δm	68
3.4.4 Effect of current density on power dissipation and (dis)charge efficiency	69
3.4.5 Effect of temperature on dissipation and (dis)charge efficiency.....	71
3.4.6 Water transport	72
3.5 Conclusions	74

Acknowledgements	75
3.6 References	76
Supplementary information chapter 3.....	78
Chapter 4 Tailoring ion exchange membranes to enable low osmotic water transport and energy efficient electrodialysis.....	79
Abstract	80
4.1 Introduction	80
4.2 Experimental.....	82
4.2.1 Meshed ion exchange membrane synthesis	82
4.2.2 Measurement of electrical resistance	83
4.2.3 Experimental setup	83
4.2.4 Energy efficiency calculations.....	84
4.2.5 Diluate yield and water transfer coefficient.....	85
4.3 Results and discussion	85
4.3.1 Osmosis through meshed ion exchange membranes at zero current condition.....	85
4.3.2 Electrical resistance of meshed membranes	88
4.3.3 Water and NaCl salt transport through meshed ion exchange membranes at non-zero current condition.....	89
4.3.4 Energy efficiency.....	92
4.3.5 Diluate yield	94
4.4 Conclusions	95
Acknowledgments	96
4.5 References	96
Chapter 5 Performance of an environmentally benign Acid Base Flow Battery at high energy density	99
Abstract	100
5.1 Background.....	100
5.2 Theory	102
5.3 Materials and Method	107
5.3.1 Experimental set-up	107
5.3.2 Experimental procedure	108

5.4 Results and Discussion	109
5.4.1 Charge and discharge characteristics.....	109
5.4.2 Main dissipation sources.....	110
5.5 Conclusions	113
Acknowledgements	114
5.6 References	114
Chapter 6 General discussion and outlook	119
6.1 Theory of energy flow, revenue and costs of a storage system	120
6.2 Sources of revenue for an energy storage system.....	123
6.2.1 Large scale energy trading.....	125
6.2.2 Externalities in electricity prices.....	127
6.3 Costs of storage technologies	128
6.3.1 Costs of a CGFB and ABFB system.....	128
6.3.2 Costs comparison of the CGFB and ABFB with other storage systems	130
6.4 Sensitivity analysis	131
6.5 Making a profit	135
6.6 Sustainability	137
6.7 Size of a CGFB.....	140
6.8 Concluding remarks.....	142
6.9 References	142
Summary	147
Samenvatting	151
Dankwoord	157

Chapter 1

General introduction

1.1 General introduction

Since the turn of the century photovoltaic power is growing rapidly. Worldwide total installed solar photovoltaic power has increased from 1-4 GW in 2000 to 227 GW in 2015 ¹⁻⁴. Similarly, total installed wind power has increased from 17 GW in 2000 to 433 GW in 2015 ^{1,5}. Figure 1.1 shows cumulative worldwide installed photovoltaic and wind power. Both renewable energy sources show steady growth. Compared to total global electricity production, the fraction of renewable electricity production by solar photovoltaics and wind is still modest (4.9% ¹). Nonetheless, the power market is already changing. In fact currently, annually worldwide more renewable power capacity is added than fossil fuel power capacity ¹. Costs of solar photovoltaic power and on-shore wind power are steadily dropping and are expected to become increasingly cost-competitive with fossil fuel power, empowering further growth of these types of renewable energy generation ⁶⁻¹⁰.

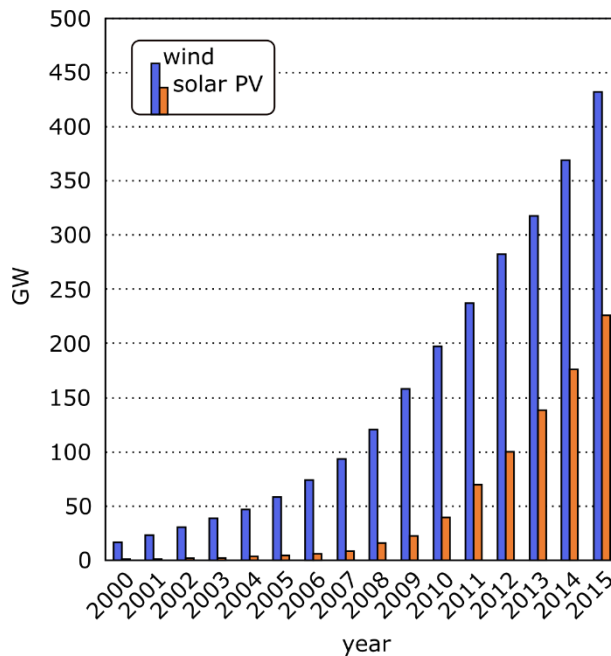


Figure 1.1. Global cumulative installed capacity of photovoltaic and wind power from 2000 till 2015 ^{1,2,5}.

Both sun and wind are intermittent energy sources. Increasing the fraction of energy supplied by intermittent sources of energy leads to increased difficulty in matching supply and demand on the electricity grid ^{3,11,12}. Assuming that the fraction of energy supplied by renewables continues to expand, a solution to the unbalance on the electricity grid is needed. There are three ways to solve this unbalance in supply and demand from the supply side perspective. The first solution (i) is to overdimension the renewable energy infrastructure (e.g. extra wind turbines, solar panels and long-distance transport). In this case even during periods when local energy supply is low (e.g. a windless night), energy is still supplied by importing energy from a distance. However, overdimensioning of infrastructure implies that during most time of the year, part of the

infrastructure is not in use and that in times of over supply curtailment is necessary. The second solution (ii) is to maintain fossil fuel powered power stations for providing backup power. In this case, when supply is low, the power stations can ramp up and supply energy. Yet, also here most time of the year the power stations will not be in use. Moreover, in this case we would still use fossil fuels which is unsustainable. The last option (iii) is to create energy storage ^{12–16}. Here, excess energy during period of over supply are stored for use when energy supply is too low. This energy storage should be sustainable however. There is no point in switching to sustainable energy generation if the accompanied storage is unsustainable. Besides the sustainability aspect, many other aspects (e.g. performance, safety, scalability etc.) need to be considered when designing an energy storage system.

This thesis explores the technological viability of a potentially safe, sustainable energy storage system, the concentration gradient flow battery (CGFB). The CGFB stores energy in a concentration difference between salt and fresh water solutions using membranes. To understand the need for such a safe and sustainable system, first the current options for large scale energy storage are explored, next the CGFB is described in detail with emphasis on the membrane potential.

1.2 Large scale electrical energy storage (EES)

There exists a myriad of energy storage technologies, however not every technology can be used for grid scale energy storage ¹⁷. Figure 1.2 shows general discharge time and power rating characteristics of several energy storage systems ^{18,19}.

The bottom x-axis of figure 1.2 shows the range of system module power ratings. The figure gives at a glance insight on the typical power and capacity ratings of different technologies but is meant for conceptual purpose only as the ratings could be stretched ¹⁹. The y-axis shows how long a storage system can maintain delivering the rated power before the system is completely discharged. As an example, consider high power supercapacitors. Supercapacitors are known to be able to charge and discharge quickly but are also known for their limited capacity compared to for example batteries ¹⁸. Figure 1.2 shows that a high-power supercapacitor system is able to discharge relatively fast (up to a MW), but can only sustain this power rating for a short period of time (in the order of seconds). Energy storage systems can have use in different parts of the energy infrastructure depending on their discharge power rating. The top x-axis divides the range of discharge power in three general categories of storage application size; uninterruptible power supply (UPS) and power quality (e.g. backup power for datacentres), transmission and distribution grid support (e.g. deferral of investment costs of energy infrastructure) and bulk power management (e.g. time shift of renewable energy on a grid scale) ^{18,19}. A more detailed analysis of the energy market and infrastructure can be found in chapter 6. There, the given examples are worked out in more detail and other applications are discussed as well. The division in figure 1.2 is an estimation and applications can overlap in reality. To buffer excess solar and wind energy for example on a grid scale, discharge times in the order of hours and power ratings of at least multiple MWs are required ^{19,20}. These types of systems are called large scale electrical

energy storage systems (EES). The red square in figure 1.2 shows the target range of large scale EES technologies ^{19,20} and shows that it overlaps with bulk power management and transmission and distribution grid support.

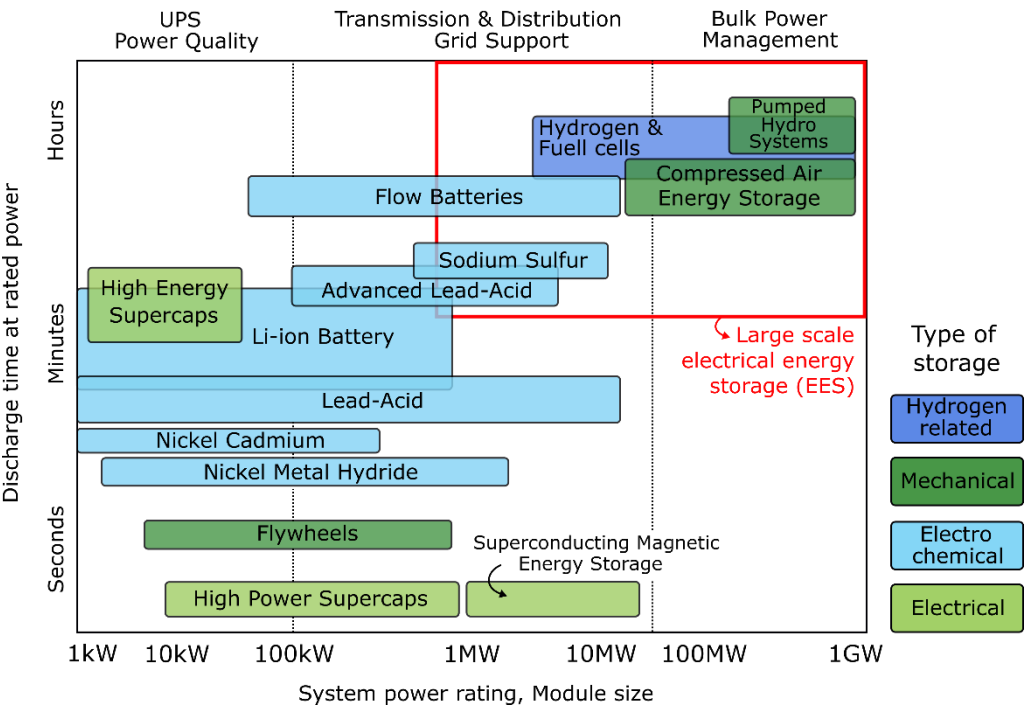


Figure 1.2. System characteristics of different energy storage technologies adapted from Taylor et al ¹⁸ and Akhil et al. ¹⁹. The red square highlights the required discharge time and power rating of a large scale electrical energy storage system.

Besides techno-economic considerations like costs, power rating and discharge times, also broader issues as sustainability, safety and governance that surround an EES are considered of major importance ^{21,22}. To deploy an energy storage technology on a global scale, also political aspects such as dependency of supply of materials from non-friendly nations, cross-border impacts etc. should be considered. Here, we will first compare the broader issues of different energy storage technologies and compare them to expected properties of the CGFB. The techno-economic evaluation of the CGFB will be dealt with in Chapter 6 in detail after Chapters 2 till 5 have determined typical performance. At this point a techno-economic evaluation would be of little substance as the CGFB is basically a new technology not yet studied in any detail.

To compare different energy storage technologies, an overview is compiled based on numerous studies as shown in table 1.1 and sections 1.2.1-1.2.4. Table 1.1 summarizes the technical specifications of most well-known large scale EES technologies including references. It also summarizes whether or not a technology complies with three broader issues relevant to a society;

that a technology is safe, sustainable and has no political issues. Subsequently, in sections 1.2.1-1.2.4 the technologies are discussed in more detail and additional references are provided on which results in table 1.1 are based.

Safety: This category indicates whether a storage technology is considered safe, including environmental safety. Examples of safety issues are fire- and explosion hazard. Some technologies rely on materials that are toxic to life or the environment. It is also possible that although the materials used themselves are not considered toxic, the production process of those material results in damage to the environment.

Sustainability: Energy storage systems are part of the energy infrastructure. It is of vital importance that the energy infrastructure as a whole produces more energy than it costs to construct, maintain and recycle its components. Therefore, consumption of energy during construction and recycling of energy storage systems is preferably low. This means for example that for technologies where recovery of all materials is very energy intensive, the overall energy balance could turn negative. This would make such a storage system unsustainable. Another possibility is that it is very energy intensive to mine certain materials, or that the production process does irreversible damage to the environment.

Politics: This category contains the main other non-financial factors that help or hinder the realization of wide scale introduction of energy storage. It indicates whether a storage technology is preferred from a political point of view as it is often the task of some governing body to make a decision, in this be it a local- or national authority or some other kind of agency. There can be different reasons why a storage technology could encounter political obstacles. Scalability and geographical limitations are two of those possible factors. Not all countries and regions are the same (mountainous, flat, concentrated or sparse population etc.). It is not always possible to place a technology in certain areas or regions. This could be because of technical reasons but also because people object (e.g. not-in-my-backyard effect) to it. Also, some energy storage systems cannot be easily scaled up (or down) to meet a specific application. Ideally, an energy storage system can be applied for different sized applications and can be installed anywhere on the world. Abundance and availability of raw materials could be another possible factor. Some energy storage technologies use scarce materials. It is also possible that materials are abundantly available to only a few (non-friendly) nations. Ideally, for an energy storage system to become widespread across the world, it is preferable that it is made of materials readily available to most nations. Another obstacle could be the requirement of large capital costs for which the government needs to step in.

Considering table 1.1, each row represents a different storage technology and each column a different aspect. The first four columns show technical performance characteristics (energy

density, power density, energy efficiency and estimated lifetime) including references. The remaining three columns show whether or not a technology complies with the three mentioned aspects relevant to society. If a technology complies a checkmark is given (✓). If a technology is considered to comply with caveats (e.g. it complies only in some specific cases or has the potential to comply in the near future), a tilde sign is given (~). Sections 1.2.1-1.2.4 discuss the assessment of these societal aspects of the mentioned technologies in more detail.

Table 1.1. Overview of electrical energy storage technologies studied. References used are indicated in superscript. (-) no data, (*) estimate., (✓) a technology is compliant, (~) a technology is near-compliant. Sections 1.2.1-1.2.4 provide references for assessment of societal aspects.




	Energy density (Wh L ⁻¹)	Power density (W L ⁻¹)	Energy efficiency (%)	Lifetime (no. cycles)	 Safety	 Sustainability	 Politics
Pumped Hydro (PHS)	0.5-1.5 15,20	0.5-1.5 15,23	70-85 15,24,25	10.000- 30.000 26		✓	
Compressed Air (CAES)	2-6 ^{23,27,28}	0.2-2 ^{27,29}	40-60 27,30,31	8.000- 12.000 ^{26,27}	✓	~	~
Li-ion	200-620 23,27,29	1.300- 10.000 27,29	85-98 20,29,32	1.000- 10.000 15,27		~	~
Lead-acid (PbA)	30-90 15,20,23,33	10-400 15,23	63-90 26,32,34,35	200-1.800 15,36	~		✓
Vanadium redox flow (VRFB)	16-35 ^{27,29}	<2 ^{23,28,29}	65-85 20,29,37	>12.000 15,23,29	✓	~	~
Sodium-Sulfur (NaS)	150-300 15,28	140-180 23,28	75-85 23,38	2.500- 4.500 ^{15,29}		✓	✓
Zinc-Bromine (ZnBr)	30-65 ^{15,28}	<25 23,28	65-80 15,26,29,35	>2.000 ^{15,29}	~		✓
Nickel-Cadmium (NiCd)	15-150 15,28	80-600 23,28	60-83 26,29,32	2.000- 3.500 ^{15,39}			✓
Hydrogen-Fuel Cell	500-3.000 15,23	>500 ^{15,23}	20-66 20,32,40	1.000- >20.000 15,41		~	✓
Concentration Gradient Flow Battery (CGFB)	0.1-1.3 42,43	0.01-0.2*	15-40*	-	✓*	✓*	✓*

Figure 1.3 is a Venn diagram consisting of three circles, visualising information from table 1.1. Each circle represents one of the three different aspects of energy storage system design relevant to society. All technologies of table 1.1 are inserted in figure 1.3 as black dots. If a technology is inserted inside the inner circle it is considered to comply (for example very safe, sustainable or no political issues). If a technology is placed in the outer circle, the technology is considered to comply with caveats. Note that the distance between dots and spheres do not have any meaning. The golden area in the middle of the Venn diagram is the ‘sweet spot’, any storage technology in this area complies with all three aspects and is considered desirable from societal point of view. So far, none of the existing technologies is located in the sweet spot. This thesis explores whether CGFB technology could fill this void. But first, three commonly referred energy storage systems (PHS, CAES and Li-ion) are discussed using table 1.1 and figure 1.3 (section 1.2.1-1.2.3). The other technologies mentioned in table 1.1 and figure 1.3 are discussed in the section after that (section 1.2.4).

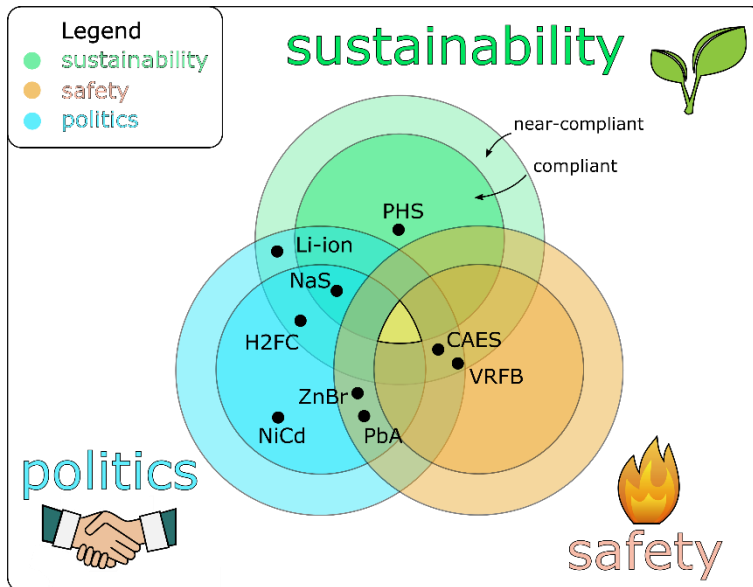


Figure 1.3. Venn diagram considering aspects sustainability, safety and politics. Commonly known energy storage systems from table 1.1 are displayed as black dots.

1.2.1 Pumped Hydro Storage (PHS)

Pumped Hydro Storage is by far the most important EES technology in the world. In 2015, worldwide cumulative installed PHS capacity accounted for 97% of total installed electrical storage capacity ⁴⁴. It has already been in use since at least 1890 ²⁴. A PHS system consists of a pump, a turbine and two large reservoirs at different height. Reservoirs can be available in nature (such as a mountain lake or underground cavity) or are man-made (for example by placing a dam in a valley). If excess electricity is available, water is pumped from the lower reservoir to the

higher reservoir. Electrical energy is thus stored as gravimetric potential energy. When power demand increases, water flows downhill through the turbine generating electricity. Because the technology uses mostly water it is considered sustainable (figure 1.3). In rare cases, dams can fail however. If this happens, damage is often very large. The most notable example of this, is the Banqiao reservoir dam disaster in 1975 in China. This disaster led to large loss of life and 11 million people lost their homes. Although the chance of dam failure is low, impact is high. Therefore PHS is placed outside of the safety circle. The reservoirs can have appreciable sizes and height differences and therefore high power is attainable (>100 MW^{26,29}). PHS systems have a long life time (>40 years²⁰) and energy efficiency is also high (70-85%^{15,24}). The most important disadvantages of PHS are the low scalability and geographical constraints^{20,24,26}. PHS systems are typically capital intensive and require large reservoirs at an appreciable height difference to be economically feasible^{20,24,26}. Therefore, the system cannot be built everywhere. For these disadvantages, PHS is placed outside of the political aspect circle in figure 1.3.

1.2.2 Compressed Air Energy Storage (CAES)

Compressed Air Storage (CAS) or Compressed Air Energy Storage (CAES) is a technology where excess electricity is used to drive electric compressors. The compressors pressurize air which is stored in a reservoir. In this way, electric energy is converted in potential energy. During discharge, the compressed air is allowed to expand in an air turbine and electric energy is recovered. When air is compressed, heat is generated. Conversely, when air is expanded it cools down. Depending on how this heat is handled, three subcategories can be distinguished; Diabatic CAES (D-CAES), Adiabatic CAES (A-CAES) and Isothermal CAES (I-CAES)³⁰. In D-CAES, the compressed air is cooled. During the expansion phase, fuel is consumed to heat the turbine and components to prevent freezing. The consumption of fuel places the CAES technology in the outer sustainability circle in figure 1.3. The other two categories try to avoid the waste of heat or consumption of fuel by adding thermal energy storage (TES), using heat exchangers or slowing down the process^{30,45}. Typically, the reservoir used for air storage is natural (e.g. salt domes, aquifers³⁴), meaning that CAES is also geographically constrained. This places the CAES in the outer political circle in figure 1.3. If high pressure vessels are used, costs increase significantly reducing economic feasibility³⁴. Another important challenge for CAES is to increase energy efficiency²³ which is currently around 40-60%^{27,30,31}.

1.2.3 Li-ion

Li-ion batteries are well-known by the general public and have formidable performance. The energy density is approximately $200-620$ kWh m⁻³^{23,27,29} and energy efficiency between 85-98%^{20,29}. A typical Li-ion battery consists of a lithium metal oxide (LiCoO₂) as cathode, graphitic carbon as anode and an organic electrolyte (alkyl carbonate) with dissolved Li salt (LiPF₆)^{23,46,47}. Charging and discharging is possible by reversible intercalation-deintercalation reactions occurring in the electrodes. The anode, cathode and electrolyte can be varied to tailor a battery for a specific purpose. Examples of alternative materials are; Olivine lithium metal phosphates or sulfur (cathode), lithium titanate (anode) or gel polymer (electrolyte)^{47,48}. Li-ion technology

is a good electrochemical energy storage technology and is now also making its way into stationary energy storage. Still, depending on choice of materials one or more important challenges remain; safety (fire- and explosion hazard place these batteries outside the safety circle in figure 1.3), cycle life, sustainability (e.g. difficult to recycle, using scarce resources) and costs^{21,36,46,47,49,50}. The difficulty in recycling and short life cycle places Li-ion batteries in the outer sustainability circle. The dependence on supply of scarce resources (e.g. cobalt) from other nations places Li-ion technology in the outer political circle in figure 1.3.

1.2.4 Other energy storage systems

Frenchman Gaston Planté developed the lead-acid battery in 1859. This system is based on the electrochemical conversion of lead oxide and lead to lead sulphate and typically uses sulfuric acid as electrolyte^{51,52}. Lead acid batteries are considered a mature technology and comprise a relatively low-cost energy storage system³². One of the downsides of traditional lead-acid battery systems is their poor cycle life, leading to low lifetimes^{23,51}. Yet, significant improvement in cycle life has taken place by for example addition of different forms of carbon^{53–55}. In the case of (over)charging, hydrogen gas can be generated. It is also possible that internal short circuit caused by for example a damaged separator could lead to thermal runaway. If not properly controlled both of these effects could lead to an explosion or acid spraying⁵². Another disadvantage of lead-acid battery systems is the use of lead which is toxic to humans and ecosystems. Lead recycling is very advanced and the vast majority of lead from lead acid batteries is recycled. Still, lead production and recycling faces issues such as the release of lead particulates and SO₂ in the atmosphere, high energy costs of recycling, production of lead containing slag, danger of long-time exposure to lead compounds for workers in the lead processing industry and leakage of lead from the technosphere to the ecosphere^{56–59}. The disadvantages place lead-acid batteries outside the sustainability sphere and in the rim of the safety sphere in figure 1.3. The vanadium redox flow battery (VRFB) is a redox flow battery based on VO²⁺/VO₂⁺ and V³⁺/V²⁺ redox couples⁵⁹. The electrolytes are typically separated by a cation exchange membrane⁶⁰. The high costs of the electrolyte is a known limiting factor in the commercial applicability of the system⁶⁰. Disadvantages of VRFB technology are the insecurity in long term access and supply of vanadium and energetic costs of production^{13,22,61}. Although operation of VRFB is generally viewed as safe^{62,63}, leakage of especially higher oxidation state vanadium might be an environmental issue⁶³. Sodium sulphur storage systems (NaS) use molten sulphur at the positive electrode and molten sodium at the negative electrode and the liquids are separated by a beta alumina ceramic electrolyte^{17,32}. Sodium sulphur batteries typically operate at temperatures of 300-350 °C to increase reaction kinetics and to maintain the molten state of the salts^{17,64}. The high availability of sodium and sulphur from nature is interesting from a sustainability point of view. Other advantages are high energy efficiency, high energy density and low material costs^{15,23,64}. A large disadvantage is safety. It contains highly corrosive sodium polysulfides and in the case of cell failure, contact between molten sulphides and molten sodium could lead to fire or explosions⁶⁴. Therefore, NaS batteries are placed outside the safety sphere. Another type of flow battery is the zinc bromine (ZnBr) battery. The battery consists of two

aqueous solutions based on zinc and bromine stored in external tanks. The liquids flow through a stack containing ion exchange membranes and electrodes where a reversible electrochemical reaction occurs. Zinc ions are converted to metallic zinc and bromide ions are converted to bromine and vice versa^{23,36,65}. Main disadvantages include the high energetic costs of production and recycling^{13,22} and possible safety issues related to toxic bromine^{66,67}. A redox reaction between nickel oxide hydroxide and cadmium is the basis for the nickel cadmium (NiCd) battery⁶⁸. Development of this battery started around 1950 and is a well-developed technology nowadays with good performance³⁶. The largest disadvantage of this technology is the toxicity of cadmium^{20,32,36,68}. Energy can also be stored in hydrogen. A combination between an electrolyser, a hydrogen fuel cell and some means of hydrogen storage is also referred to as a regenerative fuel cell system⁴¹. Excess electricity is converted into hydrogen and oxygen using the electrolyser. When power is needed, hydrogen (and oxygen) is converted into electric power using the fuel cell^{23,41}. At the moment, the regenerative fuel cell systems use precious materials such as palladium and platinum^{23,36}. Storage of large amounts of hydrogen brings a risk of fire or explosion. For this reason, hydrogen fuel cell technology (H2FC) is placed outside the safety sphere.

Analysis of existing technologies showed that none of them can satisfy demands of all three societal aspects (safety, sustainability and politics). In theory, a CGFB has the potential to meet these demands. The next section explains how a CGFB works. In the following chapters technological aspects are studied (chapters 2-5). Having learnt the technological performance of a CGFB, the environmental, safety and political aspects are finally discussed in chapter 6, to see whether the CGFB could be placed inside the golden area of figure 1.3.

1.3 Concentration Gradient Flow Battery (CGFB)

A good large scale EES fits in the sweet spot of figure 1.3. Besides from being competitive from an economical point of view (chapter 6), it has low self-discharge, low environmental impact, is recyclable, made of abundant materials, safe, scalable, consumes little energy to produce and recycle and is not geographically constrained. At the moment none of the technologies introduced in the previous section comply with all of these demands. The Concentration Gradient Flow Battery (CGFB) is a battery which has potential to meet the aforementioned demands. A CGFB is mostly made of environmental friendly and harmless NaCl solution that is abundantly available around the globe. It does not require scarce, precious or toxic materials. It can be applied anywhere and is scalable. It cannot catch fire or explode and has no self-discharge. In theory, the battery is recyclable and costs relatively little energy to produce and recycle. In this section first a general description on how the CGFB works is given, followed by basic theory on how a concentration gradient is transformed into a potential difference. In following chapters working of a CGFB is explained in detail, theory is expanded and verified with experimental work.

1.3.1 Battery concept

A typical CGFB consist out of at least two reservoirs filled with NaCl solutions, pumps, electrodes and ion exchange membranes. Figure 1.3 shows a diagram of the main components and both the charge and discharge step.

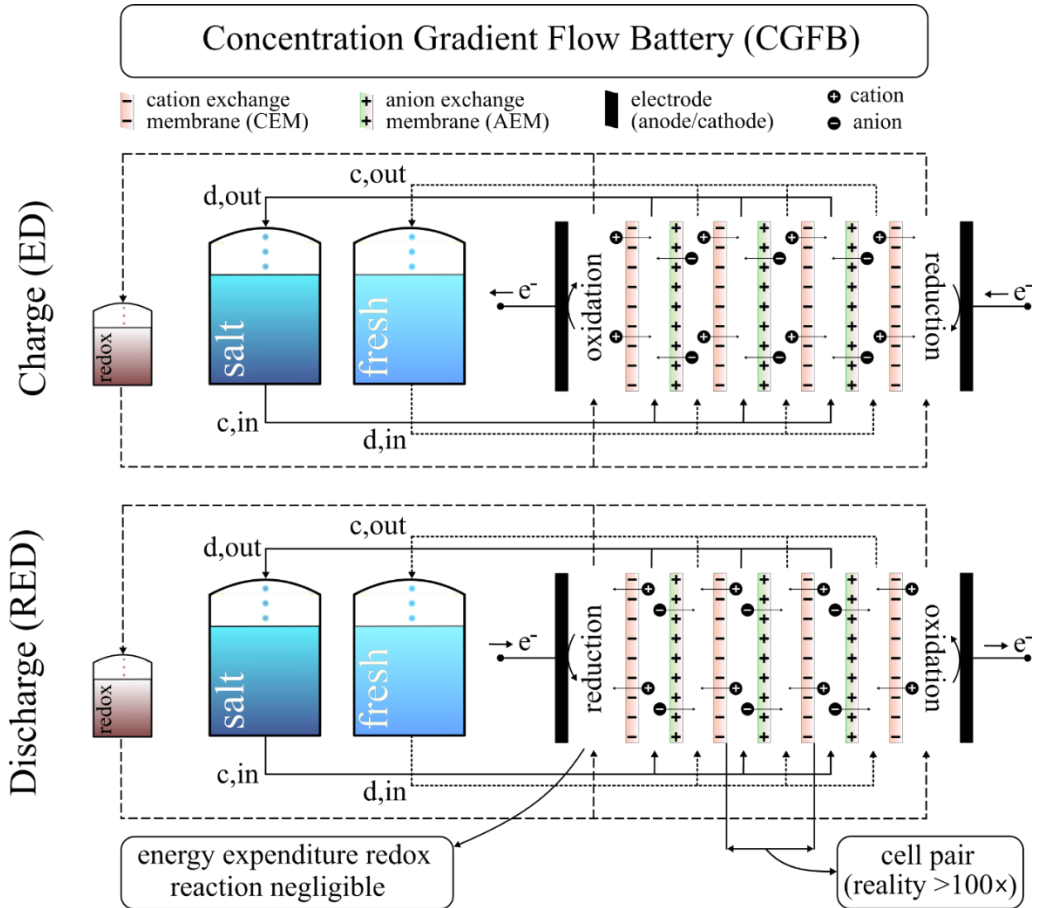


Figure 1.4. A diagram of a CGFB. At the top a legend is provided. The assembly of electrodes and membranes is referred to as 'stack'. The reservoirs at the right contain the salt solutions.

The membranes in figure 1.4 are separated by spacers (not shown). These spacers create space between the membranes and allow solutions to flow along the membranes. At the start of the charge process, the battery is completely empty. At this stage, both reservoirs named 'salt' and 'fresh' contain equal sodium chloride solutions. Once charging starts, both solutions are pumped through the assembly of electrodes and ion exchange membranes. This assembly is called a 'stack'. During the charge process, a potential is applied over the electrodes. As a result, salt is transported across the ion exchange membranes. This process is known as Electrodialysis (ED). The reservoir 'salt' will become more concentrated and reservoir 'fresh' will become more

diluted. Two solutions with different concentrations have a different chemical potential. During the charging process, the difference in electric potential is thus transformed into a chemical potential difference. The two solutions contain energy and can be stored indefinitely without self-discharge. Once the battery has been charged and the current is stopped, a voltage is measured over both electrodes. When an ion exchange membrane is immersed in a high concentration solution on one side and a low concentration solution on the other side, a membrane potential develops as result of the different Donnan potentials at the membrane-solution interfaces. When stacking multiple membranes alternately as is visualised in figure 1.4, the membrane potentials add to the measured voltage over the electrodes. During discharge, the process reverses. This reversed process is known as Reverse Electrodialysis (RED). In this case, salt is allowed to move across the ion exchange membranes from high concentration solution to low concentration solution. The voltage over the electrodes is used to supply energy back to the electricity grid. At the end of the discharge process, both solutions have their original concentrations again and the cycle can start again. The spaces between two membranes where solution flows are referred to as compartments. In figure 1.4 there is an ionic current across membranes and compartments. To convert the ionic current to electric current at the electrodes, a redox reaction (e.g. electrolysis) occurs at the electrodes. For this purpose, a solution is pumped along the electrodes which is recycled and stored separately in a (small) reservoir called ‘redox’. During both charge and discharge energy is lost in this redox reaction. However, since a real CGFB will have many cell pairs in series, the energy lost is negligible to the total amount of energy stored and harvested.

1.3.2 Membrane potential

In a CGFB, the ion exchange membrane is required for transforming the chemical potential difference of different solutions into an electric potential which can be harvested. This section explains in more detail how a membrane potential develops. Figure 1.5 shows a schematic of a cation ion exchange membrane immersed in electrolyte. Between both sides of the membrane there is a difference in salt concentration of the electrolytes. In this example a monovalent salt such as NaCl is considered. The salt is considered to be completely dissolved.

The electrolyte in figure 1.5 contains only mobile ions (e.g. Na^+ and Cl^-). The cation exchange membrane also contains next to the mobile ions (Na^+ and Cl^-) fixed charges (e.g. COO^-). The concentration of salt in the electrolyte is expressed as m_i^x , where the superscript shows location (L, left, R, right, M, membrane) and subscript shows charge. The concentration of fixed charges inside the membrane is denoted X. An equilibrium will develop between the concentration of ions in the electrolyte phase and the concentrations of ions in the membrane phase, known as Donnan equilibrium. Consider the left side membrane interface first. In this case Donnan equilibrium is defined as ^{69,70}

$$m_+^L m_-^L = m_+^{M,L} m_-^{M,L} \quad \text{eq. (1.1)}$$

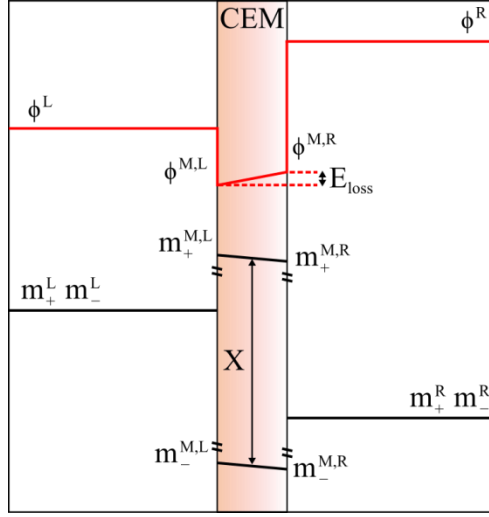


Figure 1.5. Schematic of cation exchange membrane (CEM) immersed in two different electrolytes. The left-hand side electrolyte is concentrated, the right-hand side electrolyte is diluted. Red lines are potentials (ϕ), black lines are molalities (m).

In the membrane also electroneutrality should be observed

$$m_+^{M,L} = X + m_-^{M,L} \quad \text{eq. (1.2)}$$

For a commercial ion exchange membrane a typical fixed charge concentration value is 5 M ⁷¹. Assuming $m_+^L = m_-^L$, inserting eq. 1.2 in eq. 1.1 and rearranging

$$(m_-^{M,L})^2 + X m_-^{M,L} - (m_+^L)^2 = 0 \quad \text{eq. (1.3)}$$

Solving eq. 1.3 for $m_-^{M,L}$ using the quadratic formula gives an equation for the co-ion concentration at the left-hand side interface of the cation exchange membrane in figure 1.5.

$$m_-^{M,L} = \frac{-X + \sqrt{X^2 + 4(m_+^L)^2}}{2} \quad \text{eq. (1.4)}$$

The procedure shown in eq. 1.1 to 1.3 can be repeated to obtain a similar equation for calculating co-ion concentration inside the membrane at the right-hand side membrane interface. To calculate the membrane potential, we can use the electrochemical potentials of all phases. The electrochemical potential is defined as ^{69,72}

$$\tilde{\mu}_i = \mu_i + z_i F \phi \quad \text{eq. (1.5)}$$

Where z_i is the valence of the ions, F is the Faraday constant and ϕ electric potential. The chemical potential μ_i for an ideal monovalent salt is defined as

$$\mu_i = \mu_i^0 + RT \ln(m_i) \quad \text{eq. (1.6)}$$

where m is the molality of the salt and i is ion species. When in equilibrium, the electrochemical potential is equal for all phases ^{70,73}

$$\tilde{\mu}^L = \tilde{\mu}^M = \tilde{\mu}^R \quad \text{eq. (1.7)}$$

Let us first consider the left membrane interface

$$\tilde{\mu}_+^L = \tilde{\mu}_+^{M,L} = \mu_+^{0,L} + RT \ln(m_+^L) + z_+ F \phi^L = \mu_+^{0,M,L} + RT \ln(m_+^{M,L}) + z_+ F \phi^{M,L} \quad \text{eq. (1.8)}$$

Rearranging eq. 1.8

$$\phi^{M,L} - \phi^L = E_{Donnanleft} = \frac{RT}{zF} \ln \left(\frac{m_+^L}{m_+^{M,L}} \right) \quad \text{eq. (1.9)}$$

Eq. 1.9 calculates the Donnan potential over the left-hand interface of the membrane. For the other interface on the right-hand side, a similar equation is derived

$$\phi^R - \phi^{M,R} = E_{Donnanright} = \frac{RT}{zF} \ln \left(\frac{m_+^{M,R}}{m_+^R} \right) \quad \text{eq. (1.10)}$$

Adding eqs. 1.9 and 1.10, inserting eqs. 1.2 and 1.4 and rearranging yields the membrane potential based on both Donnan potentials and assuming no diffusion potential to be present ^{72,74}

$$E_0 = E_{Donnanleft} + E_{Donnanright} = \frac{RT}{zF} \ln \left(\frac{m_+^L X + m_-^{M,R}}{m_+^R X + m_-^{M,L}} \right) = \frac{RT}{zF} \ln \left(\frac{m_+^L X + \sqrt{X^2 + 4(m_+^R)^2}}{m_+^R X + \sqrt{X^2 + 4(m_+^L)^2}} \right) \quad \text{eq. (1.11)}$$

This equation is equal to the simplified Teorell-Meyer-Sievers model ^{72,74} (chapter 2). To account for non-ideality of the solutions, molalities can be replaced by activities ^{69,72} (chapter 2-5). Description of the membrane potential is important for understanding the performance of CGFB.

1.4 Aim and outline of this thesis

This thesis aims to explore the potential of the CGFB as large-scale electricity storage technology. The goal is to determine (i) the theoretical limits of the system, (ii) to construct and determine performance characteristics of working prototypes, (iii) to identify and quantify energy losses and (iv) to find optimal working conditions. To aid in answering the aforementioned goals a theoretical working model will be developed, which is validated by experimental work. Finally, strategies are developed and tested to improve the performance of

the battery. The developments include the design of new materials and improved process operation.

In **Chapter 2** (The Concentration Gradient Flow Battery as electricity storage system: Technology potential and energy dissipation) a working prototype is constructed and tested. This chapter explains how a CGFB works in more detail and the theoretical maximum energy density of the battery is explored ($\sim 3.2 \text{ kWh m}^{-3}$ for NaCl). The maximum energy density is shown to vary as function of salt concentrations, volume ratio between salt and fresh solution and salt type. A model is introduced which includes the major dissipation factors; internal resistance, water transport and co-ion transport. Experimental work is performed to validate the model. A wide range of salt concentrations (0-3 m NaCl) and current densities (-49 to $+33 \text{ A m}^{-2}$) is chosen. From this work, an optimal working range is identified where the concentrate concentrations preferably do not exceed the 1 m. At higher concentrate concentrations water transport and co-ion transport are found to increase, heavily decreasing the energy efficiency of the battery.

In chapter 2 it was shown that the CGFB works best at low ($<1 \text{ m}$) concentrations. At low concentrations, internal resistance and water transport are shown to be the most important dissipation factors. In **chapter 3** (Energy efficiency of a Concentration Gradient Flow Battery at elevated temperatures), a more specific working range (0-1 m) is explored in more detail. Mass transport is measured accurately and an improved experimental approach allows to determine energy losses induced by water transport, internal resistance and co-ion transport in more detail. Chapter 3 shows for both the charge and discharge step the energy efficiency and quantifies the losses at each moment in time. The effect of current density and state-of-charge on power density and energy efficiency is analysed. It is shown that it is not efficient to either completely discharge or charge a CGFB. An optimal working domain is identified ($\Delta m > 0.5$ and $\eta > 0.4$) where the CGFB delivers best performance in terms of energy efficiency (max. discharge η of 72%) and power density (max. discharge power density, 1.1 W m^{-2}). Tests are also performed at different temperatures (10, 25 and 40°C) to measure the effect of temperature on mass transport, internal resistance and power density. Finally, it is shown that water transport is a major issue in the operation of a CGFB where it causes hysteresis (after discharge the battery does not return to its original state), lower efficiency and leads to decreased energy density.

To improve the performance of a CGFB, it is necessary to decrease water transport across the membranes. **Chapter 4** (Tailoring ion exchange membranes to enable low osmotic water transport and energy efficient electrodialysis) introduces modified membranes with a polymer mesh inside with very small open area (2, 10, 18 and 100% open area). The membranes are prepared by casting an ionomer solution over a polymeric mesh. The material, open area and surface properties of the mesh are changed and the effect on electrical resistance, water transport properties and the efficiency of the charge process are investigated. Comparing a meshed membrane with a homogeneous membrane, the osmotic water transfer coefficient of the meshed membrane is shown to be reduced up to a factor eight. Decreasing the open area of the mesh decreases the water permeability of the membrane but adversely increases electrical resistance.

The membranes are tested at different current densities ($5\text{--}47.5\text{ A m}^{-2}$). Chapter 4 shows that at low current densities ($5\text{--}25\text{ A m}^{-2}$) the meshed membranes outperform the homogeneous membranes in terms of energy efficiency (at a Δc of 0.7 M , maximum energy efficiency $\eta = 67\%$ for the meshed membranes and $\eta = 50\%$ for the homogeneous membranes). Using a meshed membrane in a CGFB will lead to less issue with hysteresis. In addition, the relation between material and surface property of the mesh and the ionomer resin is investigated. The type of material (PA or PET) is shown to affect the water permeability of the meshed membrane. It is shown that in some cases, compared to a non-treated mesh, a chemically treated mesh (2 M NaOH treatment) yields lower water permeability membranes. Finally, when optimized ion exchange resin is used it is expected that the water permeability can be reduced even further.

Chapter 2 and chapter 3 show that the CGFB is able to store energy in NaCl solutions which has significant environmental benefits. The measured power density is relatively low and energy density is limited because high concentrations cannot be used. In **chapter 5** (Performance of an environmentally benign Acid Base Flow Battery at high energy density) the process is changed to significantly improve power density and energy density while maintaining the environmental benefits. The adjusted system uses three energy storage solutions instead of two and stores most energy in a proton and hydroxyl ion concentration gradient. To create protons and hydroxyl ions (during charging) and to let the ions recombine to pure water again (during discharging) a bipolar membrane is added. Chapter 5 shows that the theoretical maximum energy density of the adjusted system (called Acid Base Flow Battery, ABFB) is over three times higher than the theoretical maximum of the original CGFB (chapter 2, maximum energy density of the CGFB is $\sim 3.2\text{ kWh m}^{-3}$ and $\sim 11.1\text{ kWh m}^{-3}$ for the ABFB). In addition, experiments demonstrate that the ABFB reaches a power density which is about a factor four higher compared to the original CGFB (3.7 W m^{-2} compared to 0.9 W m^{-2} of membrane area). The main dissipation sources are identified and quantified (energy lost by; co-ion transport 39–65%, ohmic resistance 23–45% and non-ohmic resistance 4–5%). The low selectivity of the membranes to protons and hydroxyls leads to a low coulombic efficiency (13–27 %). The ABFB has potential to be improved significantly. Development of better proton blocking anion exchange membranes and hydroxyl ion blocking cation exchange membranes would increase ABFB performance. Also decreasing the thickness of membranes and compartments would increase ABFB performance as it would lead to lower internal resistance energy losses. In addition, higher current densities would help reduce energy losses by co-ion transport.

Chapter 6 (General discussion and outlook) discusses important aspects of CGFB technology from a societal and commercial point of view. Costs and revenues of energy storage systems are very important drivers and can largely determine the chance of success for a storage technology. First a theoretical background of costs calculations for energy storage systems is presented. Next, the costs of future CGFB systems are calculated and compared to competing technologies. In terms of costs, the ABFB outperforms the CGFB system (0.259 and $0.366\text{ € kWh}^{-1}\text{ cycle}^{-1}$ respectively). Also, possible revenue sources are discussed. Stacking of multiple revenue streams

is possible and recommended to increase profitability. Both systems cannot yet generate a profit as costs are too high and single revenue streams are low. However, although difficult, based on the costs calculations, when performance is increased, costs can be reduced and multiple revenue streams are stacked, a commercially viable CGFB/ABFB system is estimated to be feasible. Besides technical and costs aspects, also sustainability of energy storage systems is of major importance. The energy consumption of the production and use of storage systems over their lifetime is analysed and the potential of a CGFB system is discussed. Also, choices in materials used and the system design are discussed. Finally, the size of storage technologies is important. Therefore, the size of a future CGFB system is estimated and discussed with the help of case studies. For diurnal energy storage, the size of a CGFB/ABFB is deemed acceptable given that performance is increased. Seasonal energy storage is not feasible in terms of size without significant technological improvement.

1.5 References

- (1) Sawin, L. *Renewables 2016 Global Status Report*; Paris, 2016.
- (2) Masson, G. *Global Market Outlook For Photovoltaics 2014-2018*; Brussels, 2014.
- (3) Haegel, N. M.; Margolis, R.; Buonassisi, T.; Feldman, D.; Froitzheim, A.; Garabedian, R.; Green, M.; Glunz, S.; Henning, H.-M.; Holder, B.; Kaizuka, I.; Kroposki, B.; Matsubara, K.; Niki, S.; Sakurai, K.; Schindler, R. A.; Tumas, W.; Weber, E. R.; Wilson, G.; Woodhouse, M.; Kurtz, S. *Science* (80-.). **2017**, 356 (6334), 141–143.
- (4) Brunisholz, M. *IEA-PVPS A Snapshot of Global Photovoltaic Markets 1992-2015*; St. Ursen, 2015.
- (5) Fried, L.; Qiao, L. *Global Wind Report 2015*; Brussels, 2016.
- (6) Kleiner, M. M. *Current and Future Cost of Photovoltaics. Long-term Scenarios for Market Development, System Prices and LCOE of Utility-Scale PV Systems.*; Berlin, 2015.
- (7) Priddle, R. *World Energy Outlook 2016*; Paris, 2016.
- (8) Dudley, B. *BP Statistical Review of World Energy June 2016*; London, 2016.
- (9) Dudley, B. *BP Energy Outlook 2017*; London, 2017.
- (10) Mayer, J. N. *Current and Future Cost of Photovoltaics. Long-term Scenarios for Market Development, System Prices and LCOE of Utility-Scale PV Systems*; Freiburg, 2015.
- (11) Su, Y.; Kern, J. D.; Characklis, G. W. *Appl. Energy* **2017**, 194, 172–183.
- (12) Carbajales-Dale, M.; Barnhart, C. J.; Benson, S. M. *Energy Environ. Sci.* **2014**, 7 (5), 1538–1544.

- (13) Barnhart, C. J.; Dale, M.; Brandt, A. R.; Benson, S. M. *Energy Environ. Sci.* **2013**, *6* (10), 2804–2810.
- (14) Dunn, B.; Kamath, H.; Tarascon, J.-M. *Science* (80-.). **2011**, *334* (6058), 928–935.
- (15) Chen, H.; Cong, T. N.; Yang, W.; Tan, C.; Li, Y.; Ding, Y. *Prog. Nat. Sci.* **2009**, *19* (3), 291–312.
- (16) Akinyele, D. O.; Rayudu, R. K. *Sustain. Energy Technol. Assessments* **2014**, *8*, 74–91.
- (17) Yang, Z.; Zhang, J.; Kintner-Meyer, M. C. W.; Lu, X.; Choi, D.; Lemmon, J. P.; Liu, J. *Chem. Rev.* **2011**, *111* (5), 3577–3613.
- (18) Taylor, P.; Bolton, R.; Stone, D.; Zhang, X.; Martin, C.; Upham, P.; Li Y.; Porter, R.; Bonvallet, E. *Pathways for energy storage in the UK*; York, 2012.
- (19) Akhil, A. A. et al. *DOE/EPRI Electricity Storage Handbook in Collaboration with NRECA*; Albuquerque, 2015.
- (20) Hameer, S.; van Niekerk, J. L. *Int. J. Energy Res.* **2015**, *39* (9), 1179–1195.
- (21) Larcher, D.; Tarascon, J. M. *Nat Chem* **2015**, *7* (1), 19–29.
- (22) Barnhart, C. J.; Benson, S. M.; Cui, Y.; McGregor, P. G.; Mulheran, P. a.; Hall, P. J.; Zavadil, B. *Energy Environ. Sci.* **2013**, *6* (4), 1083.
- (23) Luo, X.; Wang, J.; Dooner, M.; Clarke, J. *Appl. Energy* **2015**, *137*, 511–536.
- (24) Rehman, S.; Al-Hadhrami, L. M.; Alam, M. M. *Renew. Sustain. Energy Rev.* **2015**, *44*, 586–598.
- (25) Smith, S. C.; Sen, P. K.; Kroposki, B. In *2008 IEEE Power and Energy Society General Meeting - Conversion and Delivery of Electrical Energy in the 21st Century*; IEEE, 2008; pp 1–8.
- (26) Beaudin, M.; Zareipour, H.; Schellenberglobe, A.; Rosehart, W. *Energy Sustain. Dev.* **2010**, *14* (4), 302–314.
- (27) Castillo, A.; Gayme, D. F. *Energy Convers. Manag.* **2014**, *87*, 885–894.
- (28) Shannon et al. *Electrical Energy Storage: White Paper*; Geneva, 2011.
- (29) Chatzivasileiadi, A.; Ampatzi, E.; Knight, I. *Renew. Sustain. Energy Rev.* **2013**, *25* (0), 814–830.
- (30) Budt, M.; Wolf, D.; Span, R.; Yan, J. *Appl. Energy* **2016**, *170*.
- (31) Chen, L.; Zheng, T.; Mei, S.; Xue, X.; Liu, B.; Lu, Q. *J. Mod. Power Syst. Clean Energy* **2016**, *4* (4), 529–541.
- (32) T. Kousksou, P. Bruel, A. Jamil, T. El Rhafiki, Y. Z. *Sol. Energy Mater. Sol. Cells* **2014**, *120*, 59–80.
- (33) Farret, F. A.; Simões, M. G. *Integration of alternative sources of energy*; Farret, F. A., Simões, M. G., Eds.; Wiley - IEEE Press: Hoboken, 2006.

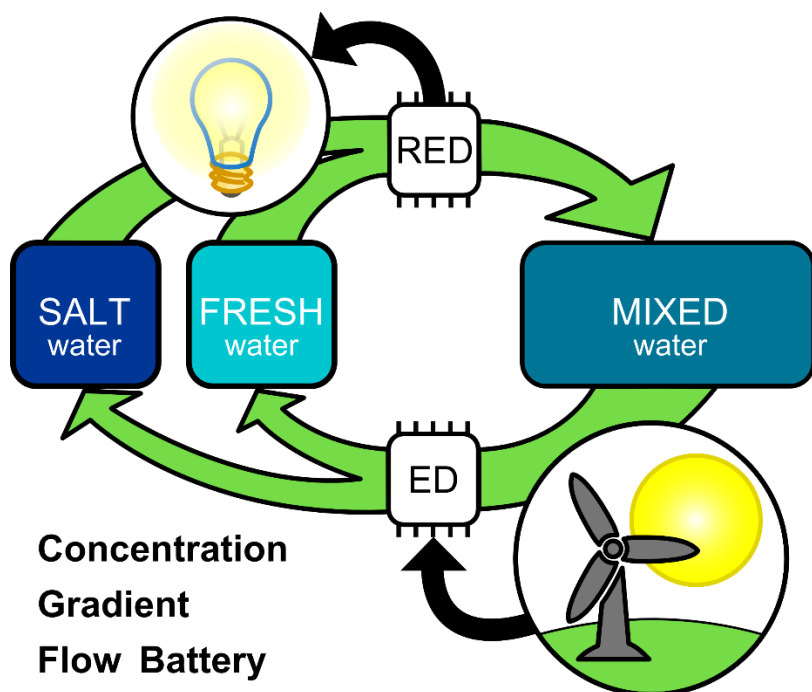
- (34) Hadjipaschalis, I.; Poullikkas, A.; Efthimiou, V. *Renew. Sustain. Energy Rev.* **2009**, *13* (6–7), 1513–1522.
- (35) Barton, J. P.; Infield, D. G. *IEEE Trans. Energy Convers.* **2004**, *19* (2), 441–448.
- (36) Díaz-González, F.; Sumper, A.; Gomis-Bellmunt, O.; Villafáfila-Robles, R. *Renew. Sustain. Energy Rev.* **2012**, *16* (4), 2154–2171.
- (37) Rastler, D. *Electricity Energy Storage Technology Options A White Paper Primer on Applications, Costs, and Benefits*; Palo Alto, 2010.
- (38) Kaldellis, J. K. *Z. D. Energy* **2007**, *32* (12), 2295–2305.
- (39) McDowell, J. J. *Power Sources* **2006**, *162* (2), 959–964.
- (40) Schaber, C.; Mazza, P.; Hammerschlag, R. *Electr. J.* **2004**, *17* (6), 21–29.
- (41) Smitha, W. *J. Power Sources* **2000**, *86* (1–2), 74–83.
- (42) van Egmond, W. J.; Saakes, M.; Porada, S.; Meuwissen, T.; Buisman, C. J. N.; Hamelers, H. V. M. *J. Power Sources* **2016**, *325*, 129–139.
- (43) van Egmond, W. J.; Starke, U. K.; Saakes, M.; Buisman, C. J. N.; Hamelers, H. V. M. *J. Power Sources* **2017**, *340*, 71–79.
- (44) Tableau Public. U.S. Department of Energy. Global Energy Storage Database http://www.energystorageexchange.org/projects/data_visualization.
- (45) Grazzini, G.; Milazzo, A. *Proc. IEEE* **2012**, *100* (2), 461–472.
- (46) Etacheri, V.; Marom, R.; Elazari, R.; Salitra, G.; Aurbach, D.; Cui, Y.; Julien, C. M.; Miners, J. H.; Poletto, L.; Grätzel, M.; Armand, M.; Zhou, Z.-B. *Energy Environ. Sci.* **2011**, *4* (9), 3243.
- (47) Bresser, D.; Paillard, E.; Passerini, S. In *Advances in Batteries for Medium and Large-Scale Energy Storage*; 2015; pp 125–211.
- (48) Bresser, D.; Paillard, E.; Passerini, S. In *Advances in Batteries for Medium and Large-Scale Energy Storage*; 2015; pp 213–289.
- (49) Kabir, M. M.; Demirocak, D. E. *Int. J. Energy Res.* **2017**.
- (50) Liu, J.; Zhang, J.-G.; Yang, Z.; Lemmon, J. P.; Imhoff, C.; Graff, G. L.; Li, L.; Hu, J.; Wang, C.; Xiao, J.; Xia, G.; Viswanathan, V. V.; Baskaran, S.; Sprengle, V.; Li, X.; Shao, Y.; Schwenzer, B. *Adv. Funct. Mater.* **2013**, *23* (8), 929–946.
- (51) Enos, D. G. In *Advances in Batteries for Medium and Large-Scale Energy Storage*; 2015; pp 57–71.
- (52) May, G.; Davidson, A.; Monahov, B. *J. Energy Storage* **2018**, *15*, 145–157.
- (53) Moseley, P. T.; Rand, D. A. J.; Peters, K. *J. Power Sources* **2015**, *295*, 268–274.
- (54) Moseley, P. T.; Nelson, R. F.; Hollenkamp, A. F. *J. Power Sources* **2006**, *157* (1), 3–10.

- (55) Shiomi, M.; Funato, T.; Nakamura, K.; Takahashi, K.; Tsubota, M. *J. Power Sources* **1997**, *64* (1–2), 147–152.
- (56) Zhang, W. et al. *Renew. Sustain. Energy Rev.* **2016**, *61*, 108–122.
- (57) Chen, L.; Xu, Z.; Liu, M.; Huang, Y.; Fan, R.; Su, Y.; Hu, G.; Peng, X.; Peng, X. *Sci. Total Environ.* **2012**, *429*, 191–198.
- (58) Sun, Z.; Cao, H.; Zhang, X.; Lin, X.; Zheng, W.; Cao, G.; Sun, Y.; Zhang, Y. *Waste Manag.* **2017**, *64*, 190–201.
- (59) Rydh, C. J. *J. Power Sources* **1999**, *80* (1), 21–29.
- (60) Kear, G.; Shah, A. A.; Walsh, F. C. *Int. J. Energy Res.* **2012**, *36* (11), 1105–1120.
- (61) Janoschka, T.; Martin, N.; Martin, U.; Friebe, C.; Morgenstern, S.; Hiller, H.; Hager, M. D.; Schubert, U. S. *Nature* **2015**, *527* (7576), 78–81.
- (62) Whitehead, A. H.; Rabbow, T. J.; Trampert, M.; Pokorny, P. *J. Power Sources* **2017**, *351*, 1–7.
- (63) Eckroad, S. et al. *Vanadium Redox Flow Batteries. An In-Depth Analysis*; Palo Alto, 2007.
- (64) Lu, X.; Yang, Z. In *Advances in Batteries for Medium and Large-Scale Energy Storage*; 2015; pp 91–124.
- (65) Li, X.; Ponce de Léon, C.; Walsh, F. C.; Wills, R. G. A.; Pletcher, D. In *Advances in Batteries for Medium and Large-Scale Energy Storage*; Elsevier, 2015; pp 293–315.
- (66) Rajarathnam, G. P.; Vassallo, A. M. In *The Zinc/Bromine Flow Battery*; Springer: Singapore, 2016; pp 11–28.
- (67) Butler, P. et al. In *Handbook of Batteries*; Linden, D., Ed.; McGraw-Hill: New York, 2002; p 1453.
- (68) Huang, Z.; Du, G. In *Advances in Batteries for Medium and Large-Scale Energy Storage*; 2015; pp 73–90.
- (69) Friedman, M. H. *Principles and Models of Biological Transport*, 1st ed.; Friedman, M. H., Ed.; Springer-Verlag: Heidelberg, 1986.
- (70) Lakshminarayanaiah, N. *Chem. Rev.* **1965**, *65* (5), 491–565.
- (71) Galama, A. H.; Post, J. W.; Stuart, M. A. C.; Biesheuvel, P. M. *J. Memb. Sci.* **2013**, *442*, 131–139.
- (72) Galama, A. H.; Post, J. W.; Hamelers, H. V. M.; Nikonenko, V. V.; Biesheuvel, P. M. *J. Membr. Sci. Res.* **2015**.
- (73) Strathmann, H. *Ion-exchange membrane separation processes*; Elsevier: Amsterdam, 2004; Vol. 9.
- (74) Hills, G. J.; Jacobs, P. W. M.; Lakshminarayanaiah, N. *Proc. R. Soc. London A Math.*

Phys. Eng. Sci. **1961**, 262 (1309).

Chapter 2

The Concentration Gradient Flow Battery as electricity storage system: Technology potential and energy dissipation



This chapter is published as

van Egmond, W.J.; Saakes, M.; Porada, S.; Meuwissen, T.; Buisman, C.J.N.; Hamelers, H.V.M. "The Concentration Gradient Flow Battery as Electricity Storage System: Technology Potential and Energy Dissipation". *J. Power Sources* **2016**, 325, 129–139.

Abstract

Unlike traditional fossil fuel plants, the wind and the sun provide power only when the renewable resource is available. To accommodate large scale use of renewable energy sources for efficient power production and utilization, energy storage systems are necessary. Here, we introduce a scalable energy storage system which operates by performing cycles during which energy generated from renewable resource is first used to produce highly concentrated brine and diluate, followed up mixing these two solutions in order to generate power. In this work, we present theoretical results of the attainable energy density as function of salt type and concentration. A linearized Nernst-Planck model is used to describe water, salt and charge transport. We validate our model over wide range of sodium chloride concentrations (0.025–3 m) and current densities (-49 to $+33$ A m⁻²). We find that depending on current density, charge and discharge steps have significantly different thermodynamic efficiency. In addition, we show that at optimal current densities, mechanisms of energy dissipation change with salt concentration. We find the highest thermodynamic efficiency at low concentrate concentrations. When using salt concentration above 1 M, water and co-ion transport contribute to high energy dissipation due to irreversible mixing.

2.1 Introduction

Due to the intermittent nature of renewable energy sources such as sun and wind, implementation of large scale electrical energy storage (EES) in the electricity grid is considered as a feasible solution to match power supply and demand. Additionally, EES is useful for preventing power outages and load levelling of the electricity grid ¹⁻¹¹. Currently, 99 % of the worldwide large scale electricity storage capacity is installed in pumped hydroelectric systems (PHS) with a total capacity of 127 GW ³. PHS store and recover energy by pumping water into an elevated reservoir and by flowing water down through a turbine. The energy density of PHS is determined by the height of the reservoir and is about 0.27 kWh m⁻³ for each additional 100 meters in height. A main limitation of PHS is the need for appropriate geographical conditions ¹. By contrast to PHS, battery storage is a new market development. Batteries are characterized by much higher energy densities and are suitable for mobile application. However, for large scale electricity storage batteries are less suitable due to high costs, safety issues and environmental concern caused by usage of toxic and scarce compounds ². Therefore, an opportunity exists for a storage system that is environmentally safe and can also be used in flat terrains.

Until now, Pressure Retarded Osmosis (PRO) which makes use of water flux through a semi-permeable membrane, and Reverse Electro Dialysis (RED) which uses the ion flux through ion-exchange membranes to produce power have been extensively studied ¹². Here, we study an energy storage system based on using two salt solutions of different concentrations not unlike the combination of RED and electrodialysis (ED) proposed in Ref. ¹³. Figure 2.1 shows a typical RED configuration used for extracting power by controlled mixing of two solutions. The same cell design can be used to split the previously mixed solution back into two solutions with different salinity. By operating the proposed system, first in RED mode (discharging step) and

then in ED mode (charging step) a closed-system battery is created. This system we call the “concentration gradient flow battery” (CGFB). Advantages of the CGFB are that it is scalable and can be used in small households as well as in large scale grid storage. Moreover, the energy-containing solutions can be made of cheap, environmentally friendly and abundant materials and the CGFB systems can be installed at any location. The solutions are also very safe.

In this work we choose to work with NaCl salt, because of its high theoretical energy density (see the results section), and because it is one of the safest, cheapest, and most abundant salts on our planet. In ideal solution the chemical potential of salt in the concentrated solution (concentrate) is higher than in the diluted solution (diluate). Interestingly, this difference of chemical potential across ion-exchange membranes (IEMs) can be utilized to extract power by transferring salt from concentrate to diluate. This is possible because IEMs allow passage of either positively charged ions (using a cation-exchange membrane, or CEM) or negatively charged ions (in an anion-exchange membrane, AEM), giving rise to a membrane potential when the salt concentration is different between the two sides. When AEMs and CEMs are combined such that half of the flow channels are fed by a concentrated solution, while the other half of the channels has a flow of diluate, an energy as high as 0.21 kWh per m³ of mixed sea and river water solution can be extracted (see Figure 2.1) ¹⁴.

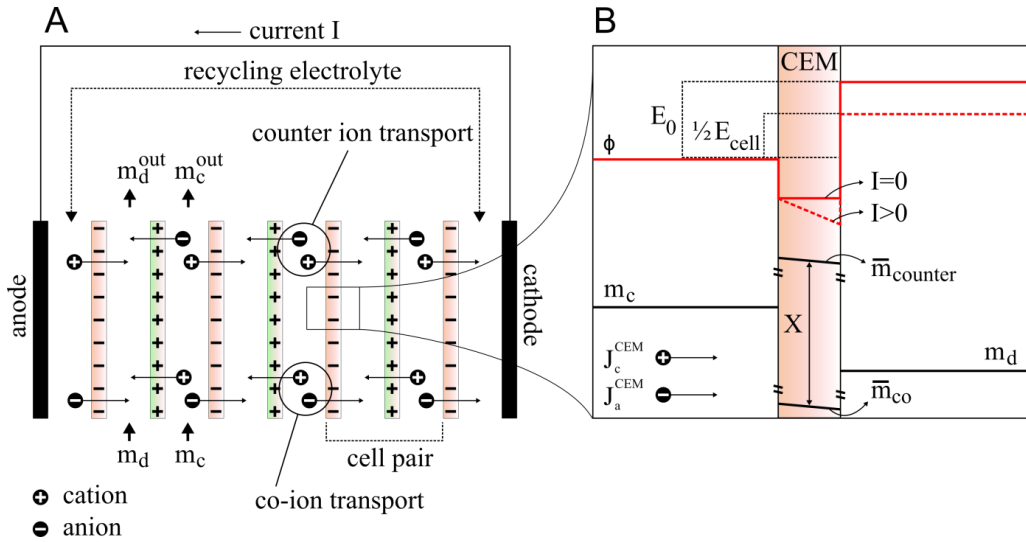


Figure 2.1. (A) Discharging step of a concentration gradient flow battery (CGFB). Due to a chemical potential difference between ingoing solutions, counterions are transported from the concentrate (m_c) to the diluate (m_d) solution, resulting in ionic current. Please note that the membrane fixed charge is denoted by black minus (-) and plus (+) signs. Two IEMs and two adjacent compartments are called a cell pair. This figure describes a stack with 3 cell pairs. Osmotic flow of water is always in the direction of the concentrate. Electro-osmosis goes in the direction of co-ion and counterion transport. For charging mode of operation, Figure 2.1A is identical, except for the direction of current and counterion transport which is reversed, and both electrodes change their polarity. (B) Illustrative picture of potential (ϕ) and concentration (m) profiles over one IEM ¹⁵ in discharge mode. Diffusion

boundary layers, diffusion potentials and potential drop in solutions are not depicted. Fixed membrane charge density is denoted as X . During charging mode Figure 2.1B is identical except for the fact that counterion transport (J_c^{CEM}) reverses its direction and potential increases.

In case of an ideal IEM, the membrane potential can be calculated using the Nernst equation ¹⁵,

$$E_m = \frac{RT}{zF} \ln \left(\frac{\gamma_c m_c}{\gamma_d m_d} \right) \quad \text{eq. (2.1)}$$

where E_m is the membrane potential (V), R the universal gas constant ($\text{J K}^{-1} \text{mol}^{-1}$), z charge of the ion, F is the Faraday's constant (C mol^{-1}) and γ and m are the activity coefficient and molality of solution respectively. Subscripts c and d describe concentrate and diluate stream.

In case of a CGFB, a higher chemical potential in the concentrate compartment leads to power release due to salt transport from the concentrate to the diluate solution. As a result of salt transport, the concentration difference between the two solutions will decrease. In order to recharge the CGFB, one needs a technology that can restore the original salt concentration difference. In this study we use ED to restore the original concentration difference. The regeneration step is carried out by applying a slightly higher potential than the membrane potential. The performance of the CGFB during discharge is described by the thermodynamic efficiency which is the ratio of the generated power over the total available power by water and salt transport. In the charging step, this thermodynamic efficiency describes the rate at which energy is stored as a fraction of the input electrical power.

Interestingly, state of the art IEMs cannot reach 100 % thermodynamic efficiency, because of other processes dissipating the available free energy take place while cycling the CGFB. We identify four such processes. (i) Firstly, energy is lost due to the resistance of IEMs and water to transport ions. This resistance is caused by an ohmic component and the presence of boundary layers which limit mass transport ^{14,16–29}. (ii) Secondly, energy is being dissipated due to the fact that IEMs are not perfectly selective and thus in practice the membrane potential is lower than the calculated Nernst potential ^{21,24–30}. (iii, iv) Lastly, two other transport processes, namely, water and co-ion transport lead to energy dissipation through salt concentration changes which do not contribute to membrane potential build-up ^{17,19,26–28,30,31}.

This paper aims at studying efficiency of the CGFB under relevant operational conditions. By measuring steady state values over wide range of salt concentrations and current densities we report the performance of CGFB during the charge and discharge phase. Our experimental data identify promising ranges of salt concentration and current densities that are worth further exploration. To theoretically describe our measurements, a steady-state model describing transport processes and membrane potential is set up. This model combines a linear solution of the Nernst-Planck model with osmotic and electro-osmotic water transport. We validate this model over extensive data sets obtained during charging and discharging. Previous work by Kingsbury et al. ¹³ showed similar results for a number of round trip experiments with a fixed

current density and for a limited concentration range. Here we analyse mass transport processes and thermodynamic efficiencies in a wide range of operational conditions and are able to distinguish between individual charge- and discharge thermodynamic efficiency. Our experimental data and calculations give valuable information on the optimal applied current window of the CGFB, and outline future directions for improvements.

2.2 Theory

In this work we model a single cell pair consisting of Neosepta CMX and AMX membranes and consider a univalent completely dissociated NaCl salt. In this section we describe a theoretical approach required to define the solution characteristics, the ion and water fluxes, membrane potential, power dissipation mechanisms and their effects on the efficiency of the CGFB during charge and discharge.

2.2.1 Solution characterization

All solutions are characterized by (i) the salt content expressed as molality m (mol kg^{-1}), (ii) the chemical potential of the salt μ_s (J mol^{-1}) including activity correction γ_{\pm} (activity coefficient) and (iii) the chemical potential of the water μ_w ($\text{J kg}^{-1} \text{H}_2\text{O}$) including another activity correction ϕ (osmotic coefficient). All activity and osmotic coefficients are obtained using the Pitzer model³² (see Supplementary Information for more details).

One can write the chemical potential, μ_s (J mol^{-1}), of the salt as

$$\mu_s = \mu_s^0 + \nu RT \ln \left(\gamma_{\pm} \frac{m}{m_0} \right) \quad \text{eq. (2.2)}$$

where μ_s^0 is the standard chemical potential (J mol^{-1}), T the temperature (K), m_0 the standard molality and ν is the number of moles of ions in one mole of salt. To account for the non-ideal behaviour of the solutions, an activity coefficient, γ_{\pm} is introduced.

Based on Ref.³³, the chemical potential of water, μ_w , is given by

$$\mu_w = -\nu RT m \phi \quad \text{eq. (2.3)}$$

where the osmotic coefficient, ϕ , is included to account for non-ideal behaviour of the solution. We calculate differences in solution characteristics over a membrane as a difference between the concentrated and dilute solutions.

2.2.2 Ionic fluxes and properties of ion-exchange membranes

As explained above, a cell pair consists of two ion exchange membranes, one CEM and one AEM, and two solution compartments flushed with concentrate and dilute (see Figure 2.1). In our model we consider transport of negatively (anions) and positively (cations) charged ions, and water molecules, indicated by a , c and w subscripts, respectively. For all fluxes we use the

symbol J . The water flux J_w is expressed as $\text{kg m}^{-2} \text{s}^{-1}$ and the salt flux J_s is expressed as $\text{mol m}^{-2} \text{s}^{-1}$, where m^2 stands for membrane surface area.

The IEMs are characterized by the fixed charge density, X_f (mol kg^{-1}) and the thickness, δ_m (m). Both membranes are assumed to have the same properties, except for the sign of the membrane charge. The fixed charge density of a membrane is high compared to the salt concentration in the solution and is either positive (AEM) or negative (CEM). The counterion concentration inside an IEM is always higher than in the bulk solution.

Ionic flux through an IEM is well described using the Nernst-Planck equation¹⁵. However, the individual ion flows cannot be discriminated in a unit cell and therefore it is common to study two associated fluxes, the molar current density and the total salt flux.

The molar current density, I_{mol} ($\text{mol m}^{-2} \text{s}^{-1}$), relates to the current density I_d , expressed in A m^{-2} by multiplying by Faraday's constant. For any IEM the molar current density can be calculated as the difference between the counterion and co ion fluxes according to

$$I_{mol} = J_C^{CEM} - J_A^{CEM} = J_C^{AEM} - J_A^{AEM} \quad \text{eq. (2.4)}$$

The total salt flux from one solution to the other can be expressed as

$$J_s = \frac{1}{2} (J_C^{CEM} + J_A^{CEM} - J_C^{AEM} - J_A^{AEM}) \quad \text{eq. (2.5)}$$

As stated above, in this work we assume that AEM and CEM properties are the same, except for the sign of the fixed membrane charge. This implies that diffusion and water permeability coefficients are expressed as average values. This also implies that counterion and co-ion fluxes are equal in magnitude but have opposite directions, thus $J_C^{CEM} = -J_A^{AEM}$ and $J_A^{CEM} = -J_C^{AEM}$. Based on the above, one can express the salt flux as $J_s = J_C^{CEM} + J_A^{CEM}$, or $J_s = I_{mol} + 2J_A^{CEM}$.

Assuming local electroneutrality inside the IEM, and in case of symmetric electrolytes, the counterion concentration inside IEM is expressed as

$$m_{counter}^{membrane} = X_f + m_{co}^{membrane} \quad \text{eq. (2.6)}$$

The relative co-ion fraction, β_c , inside the IEM can be calculated as function of the fixed charge according to^{12,34}

$$\beta_c = \frac{m_{co}^{membrane}}{X_f} = \frac{1}{2} \sqrt{1 + \left(2\gamma_c \frac{m_c}{X_f} \right)^2} - \frac{1}{2} \quad \text{eq. (2.7)}$$

Next, we express the total ion transport over a CEM using the Nernst-Planck equation in steady state by using the Henderson approach, according to

$$J_s = -\frac{2D_m X_f \rho_m}{\delta_m} (\beta_d - \beta_c) + \frac{I_{mol}}{1 + \beta_c + \beta_d} \quad \text{eq. (2.8)}$$

Where D_m is the membrane diffusion coefficient for salt, and ρ_m is the solution density inside the IEM (detailed derivation of eq. 2.8 is given in Supplementary Information). The total osmotic water flux over both membranes, J_{osm} ($\text{kg m}^{-2} \text{s}^{-1}$) is expressed in Ref. ²⁷ as

$$J_{osm} = 2L_p (-\Delta\mu_w) \quad \text{eq. (2.9)}$$

where L_p is the average water permeability coefficient ($\text{kg m}^{-2} \text{s}^{-1} \text{kg J}^{-1}$) of both IEMs. The electro-osmotic flux over both membranes, J_{eosm} ($\text{kg m}^{-2} \text{s}^{-1}$) describes water that is being dragged along with transported ions. The electro-osmotic flux is calculated as

$$J_{eosm} = J_s t_w M \quad \text{eq. (2.10)}$$

where M is the molar weight of water (kg mol^{-1}) and t_w are the water molecules associated with the transport of salt ($\text{mol water mol}^{-1} \text{salt}$). The total water transport is calculated as the sum over both membranes according to

$$J_w = 2L_p (-\Delta\mu_w) + J_s t_w M \quad \text{eq. (2.11)}$$

2.2.3 Membrane potential and internal resistance

The membrane potential at open cell potential can be calculated as the difference of the two Donnan ¹⁵ potentials on each side and is expressed as

$$E_0 = \frac{RT}{zF} \ln \left(\frac{\gamma_d m_d}{\gamma_c m_c} \cdot \frac{\beta_c}{\beta_d} \right) \quad \text{eq. (2.12)}$$

Next, in case of electrical current flow some portion of electrical power will be dissipated due to electrical resistance of IEMs and solutions, and thus the cell potential ^{17,31} can be calculated as

$$E_{cell} = 2E_0 - I_{mol} F R_i \quad \text{eq. (2.13)}$$

where R_i is the internal resistance ($\text{ohm} \cdot \text{m}^2$), which is the sum of both membrane resistances, including its boundary layer, R_f , and any shadow spacer effect, and the resistance of the diluate and concentrate compartment. The latter two resistances are determined by the distance between the membranes, δ_s (m), and the conductance, κ (S m^{-1}), of the solution. When spacers are used to build a CGFB stack, a factor λ is introduced to account for the increased path length between the membranes due to tortuosity of the fibres.

The internal resistance of the CGFB stack can be expressed as

$$R_i = R_f + \lambda \left(\frac{\delta_d}{\kappa_d} + \frac{\delta_c}{\kappa_c} \right) \quad \text{eq. (2.14)}$$

2.2.4 Energy dissipation mechanisms and system efficiencies

The chemical potential difference of a salt in two solutions separated by a membrane, $\Delta\mu_s$ (J mol⁻¹), can be calculated as

$$\Delta\mu_s = \nu RT \ln \left(\frac{\gamma_c m_c}{\gamma_d m_d} \right) \quad \text{eq. (2.15)}$$

For an incompressible solvent such as water, the difference in chemical potential, $\Delta\mu_w$ (J kg⁻¹), is expressed as

$$\Delta\mu_w = -\nu RT (\phi_c m_c - \phi_d m_d) \quad \text{eq. (2.16)}$$

Based on values of the total water flux, J_w (kg m⁻² s⁻¹), and total salt flux, J_s (mol m⁻² s⁻¹), the Gibbs free energy flux (eq. 2.17) describes the change of chemical energy as a result of ion and water transport across the IEM. Negative P_G values indicate that power is being stored during charging, whereas a positive P_G value indicates power that is being released during discharging. It is important to note that opposite to the chemical potential gradient of the salt, the chemical potential of the water in the concentrate is lower than for the diluate. A flux of water from diluate to concentrate is thus associated with a release of power and can be considered a loss of power during both charge and discharge phase,

$$P_G = J_w (-\Delta\mu_w) + J_s (-\Delta\mu_s) \quad \text{eq. (2.17)}$$

In order to identify different sources of energy dissipation, the second term on the right-hand side of eq. 2.17 can be split, leading to

$$P_G = \overbrace{J_w (-\Delta\mu_w)}^{\text{water transport}} + \overbrace{J_s (-\Delta\mu_s) - I_d 2E_0}^{\text{co-ion transport}} + \overbrace{I_d 2E_0 - I_d E_{cell}}^{\text{internal resistance}} + \overbrace{I_d E_{cell}}^{\text{cell power}} \quad \text{eq. (2.18)}$$

Next, we define the dissipated power, P_D , as a difference between the Gibbs energy flux and the cell power

$$P_D = \overbrace{J_w (-\Delta\mu_w)}^{\text{water transport}} + \overbrace{J_s (-\Delta\mu_s) - I_d 2E_0}^{\text{co-ion transport}} + \overbrace{I_d 2E_0 - I_d E_{cell}}^{\text{internal resistance}} \quad \text{eq. (2.19)}$$

Eq. 2.19 includes three sources of energy dissipation which are caused by (i) water transport, (ii) co-ion transport and (iii) internal resistances.

2.2.5 Concentration gradient flow battery efficiency

Efficiency of transforming chemical power by the CGFB into electric power during discharging is described by a thermodynamic efficiency, $\eta_{\text{discharge}}$, which is expressed as

$$\eta_{\text{discharge}} = \frac{P_{\text{cell}}}{P_G} = 1 - \frac{P_D}{P_G}.$$

The thermodynamic efficiency for charging, η_{charge} , is

$$\eta_{\text{charge}} = \frac{P_G}{P_{\text{cell}}} = 1 + \frac{P_D}{P_{\text{cell}}}.$$

Please note that the cell power during charging step is negative resulting in the thermodynamic efficiency being lower than unity.

The round trip efficiency (η_{RTE}) of the CGFB battery is defined as the ratio of the amount of energy extracted during discharging to the amount of energy needed to fully charge the battery. Although RTE is an important figure of merit for any battery, we believe that its use in our system gives an incomplete picture of the different processes occurring. In this study by selecting a wide range of salt concentrations and studying operation of CGFB battery at steady-state conditions, the mass transport, internal resistance and instantaneous thermodynamic efficiencies are determined. This approach gives more insight into relative contributions of different types of mass transport processes and energy losses at several stages of charge and discharge cycle.

2.3 Materials and methods

2.3.1 Concentration gradient flow battery stack design and operation

The CGFB stack used in this study is similar to the one used by Vermaas et al. in Ref. ²². The CGFB stack consisted of four CEM and three AEM membranes which are assembled in an alternating pattern, see Figure 2.1. The IEMs used were commercial grade CMX and AMX Neosepta membranes (Astom Corporation, Japan). The total effective area inside the CGFB is 0.01 m² per IEM. The average thickness of the membranes is 155 μm . Spacers (SEFAR AG, Switzerland) with a thickness of 210 μm and open area of around 50 % were placed between the IEMs in order to create a water flow path. Silicone gaskets are used to seal the spacer channel. The electrodes used were two titanium mesh electrodes coated with Ir/Ru (Magneto Special Anodes B.V., the Netherlands). The membranes and gaskets were held together with two end blocks pressed together with bolts with a torque of 3 Nm. All solutions used, including the solution in contact with the anode and cathode (referred to as rinse solution), were kept at constant temperature of 25 ± 1 °C using a thermal bath. Constant volumetric flow rate of 200 mL min⁻¹ of the 0.5 M Na₂SO₄ rinse solution is used during all experiments. A rather large volume of 5 L of rinse solution is used to make sure that any unforeseen chemical or temperature changes will not significantly affect experimental data. We use long tubing between the cathode and

anode compartments to minimize electrolytic short-circuit currents between the compartments¹⁶. High purity NaCl salt is used to prepare all solutions (ESCO, the Netherlands). The electrical conductivity of both inlet and both outlet streams is measured and recorded with inline conductivity probes (Thermo Fisher Scientific, VERSA STAR meter, USA). Before the experiments all conductivity probes were extensively characterized in their conductivity and temperature measurement range. A galvanostat (Ivium Technologies, the Netherlands) is used to control electrical current and to measure the potential difference. The potential difference over the membranes is measured using two reference electrodes (QM711X, QIS, the Netherlands) placed in the cathode and anode compartments. During discharging and charging mode 8 reservoirs with different salt concentrations are used. In total four different diluate solutions (0.025 m, 0.05 m, 0.1 m and 0.25 m) and four different concentrate solutions (0.5 m, 1 m, 2 m, 3 m) were pumped in their respective compartments inside the cell resulting in 16 concentration combinations. In discharging mode, eight different current densities (ranging between 5 A m⁻² and 33 A m⁻²) are tested, whereas twelve different current densities (ranging between -5 A m⁻² and -49 A m⁻²) are tested during discharge. At the start of each new measurement, the electrical current is turned off in order to allow the CGFB system to reach open circuit conditions. Experimental data obtained during charging mode at overlimiting current are not presented in this work. In order to ensure that no leakages occurred during testing and no other experimental errors were made, a second CGFB stack was built and tested. We found that results of the second CGFB were comparable with results obtained in the first stack.

2.3.2 Parameter estimation

Salt and water fluxes reported in this work are estimated based on measured molality values. A similar approach to calculate water and salt fluxes is reported in Ref.³¹. The water flux, J_w^m (kg m⁻² s⁻¹), is calculated according to

$$J_w^m = \frac{1}{A_m} \frac{F_{Ld}^{in}(m_d^{out} - m_d^{in}) + F_{Lc}^{in}(m_c^{out} - m_c^{in})}{m_d^{out} - m_c^{out}} \quad \text{eq. (2.20)}$$

where m stands for the molality of the solution (mol kg⁻¹ H₂O), F_L is the flow rate, and A_m (m²) is the total projected membrane area. Please note that the superscript indicates whether the flow is directed inside or outside the CGFB, while the subscript indicates the diluate, (d), or concentrate, (c).

The salt flux, J_s^m (mol m⁻² s⁻¹), over the total membrane area is calculated as

$$J_s^m = \frac{F_{Ld}^{in}}{A_m} (m_d^{out} - m_d^{in}) - J_w^m m_d^{out} \quad \text{eq. (2.21)}$$

Based on calculated water and salt flux other parameters such as X_f , D_m , L_p , t_w , R_i and λ are estimated. The fixed membrane charge, X_f , and the membrane diffusion coefficient, D_m , are estimated based on regression using equations 2.7 and 2.8. Likewise, by using equations 2.11

and 2.16, parameters t_w and L_p are estimated by regression. The internal resistance, R_i , and tortuosity factor, λ , are estimated based on equations 2.7 and 2.12-14 and based on the value of the fixed membrane charge, X_f . In order to assist the reader, a model flow chart summary is presented in the Supplementary Information.

2.4 Results and Discussion

2.4.1 Maximum energy density of the CGFB

The energy density of a battery is of key importance since it determines the size and weight of the system. This is true for a normal battery (e.g. Li-ion) as well as for the CGFB where power generation and energy storage are decoupled using a flow-by module and electrolyte reservoirs. The electrolyte solutions are the biggest component of the CGFB and therefore it is important to know how much energy can be stored per given electrolyte volume or mass.

The Gibbs free energy of a solution, G (J kg⁻¹ solvent), is a function of molality and can be calculated as

$$G(m) = \nu RT m \left(\ln \left(\gamma_s \frac{m}{m_0} \right) - \phi \right) \quad \text{eq. (2.22)}$$

The energy storage capacity (J kg⁻¹ of solvent) is defined as the energy released upon mixing the concentrate with the dilute solution and is expressed per total mass of solvent after mixing. The energy storage capacity of two solutions can be calculated from

$$\Phi_E = G(m_m) - \alpha G(m_c) - (1 - \alpha) G(m_d) \quad \text{eq. (2.23)}$$

where α is the fraction of the concentrated solution, and m_m is the molality of the mixed solution. The maximum energy storage capacity, $\Phi_{E,\max}$, is achieved when the salt concentration difference between two solutions is the highest. For such situations, one solution is saturated ($m_c = m_{\text{sat}}$) and one solution is pure water ($m_d = 0$). The mixed solution molality will be equal to $m_m = \alpha_{\max} m_{\text{sat}}$ and thus eq. 2.23 reduces to

$$\Phi_{E,\max} = G(m_m) - \alpha_{\max} G(m_{\text{sat}}) \quad \text{eq. (2.24)}$$

where α_{\max} is the fraction of concentrated solution at which the maximum energy storage density is reached. The value of α_{\max} can be found by optimizing $\Phi_{E,\max}$ with respect to α . The maximum energy storage density for an ideal salt equals then $\nu R T e^{-1} m_{\text{sat}}$. For example in case of an ideal solution of 5 mol kg⁻¹, the energy storage density is comparable to pumped hydro storage⁴ and equals 9.1 kJ kg⁻¹ or ~2.5 kWh m⁻³ when expressed per volume. Please note that the maximum energy storage density depends on the salt type, maximum salt concentration, an activity correction and density. In Table 2.1 we present the maximum energy density and optimal mixing ratio of several non-toxic salts.

Table 2.1. Calculated maximum energy storage density of NaCl, KCl, KI, KAcetate, NaAcetate and KNO₃ salts at 298 K. Activity coefficients, osmotic coefficients and m_{sat} are adapted from Pitzer et al. ³². Total solutions volume is equal to 1 m³.

Salt	m_{sat}	$E_{\text{d,max}}$ (MJ)	α
NaCl	6	11.5	0.43
KCl	4.8	7.8	0.39
KI	4.5	7.4	0.41
CH ₃ COOHK	3.5	6.7	0.40
CH ₃ COOHNa	3.5	6.7	0.41
KNO ₃	3.8	4.3	0.34

Table 2.1 shows that the maximum energy storage density depends on salt type. This is in large part due to the maximum attainable salt concentration. Also, the activity coefficient and osmotic coefficient differ for each salt type and thus affect the energy storage density.

2.4.2 Parameter estimation

Table 2.2 shows results of the parameter fitting describing the salt and water flux, and internal resistance. In Table 2.2 we also show the covariance of two variables divided by the product of their standard deviations, which is called the Pearson correlation coefficient. This value equals the correlation coefficient R^2 in case of linear regression, but is used here to also find the value for the non-linear regression used for estimating the salt flux.

We find that the estimated value of fixed charge density is lower compared to values reported in Ref. ¹⁵. Next, using the value of the fixed charge density and known membrane thickness, the diffusion coefficient inside the membrane can be calculated as $1.6 \cdot 10^{-11} \text{ m}^2 \text{ s}^{-1}$. We also find that the diffusion coefficient, D_m , and the water permeability coefficient, L_p , are in good agreement with values reported by Veerman et al. in Ref. ³¹ with high R^2 values showing that the variance is well explained by the model.

For the number of water molecules associated with salt transport, t_w , we find good agreement with values reported by Galama et al. ³⁰. The R^2 value of the t_w and L_p parameters is lower compared to other values. This difference can be explained by the fact that the numerator of the estimate of the water flux (eq. 2.20), contains the difference of solution molality going inside and outside the CGFB stack. We note that this difference is small compared to the incoming concentration itself, which results in a high intrinsic variance of the estimate. A further indication that the high intrinsic variance plays an important role in explaining the coefficient of determination can be found in the statistical significance of the parameters, as both L_p and t_w are significantly lower than 0.001%, while the intercept was not significant. Finally, we used the electrical potential difference data to determine the membrane resistance (eq. 2.14) and the tortuosity factor. The estimated values are in line with those obtained by Galama et al. ^{15,35}.

Table 2.2. Parameter values used to model the CGFB system.

Flux	eq.	parameter	value	unit	R^2
J_s	8	X	3.45	$\text{mol kg}^{-1} \text{H}_2\text{O}$	0.95
		D_m	$1.6\text{e-}11$	$\text{m}^2 \text{s}^{-1}$	
J_w	11	L_p	$2.4\text{e-}08$	$\text{kg m}^{-2} \text{s}^{-1} \text{kg J}^{-1}$	0.67
		t_w	5.2	$\text{mol H}_2\text{O mol}^{-1} \text{salt}$	
R_i	14	R_f	7.0	$\Omega \cdot \text{cm}^2$	0.96
		λ	2.8		

In Figure 2.2 we show the parity plots of the cell power, P_{cell} , and the Gibbs free energy flux, P_G . We find that the P_{cell} is well described, ($R^2=0.99$), while the correlation coefficient of P_G shows a higher variance equal to 0.92. The larger variance for the Gibbs free energy flux is probably due to the large variance of the estimation of the water flux as the water flux is part of the calculation of Gibbs free energy flux (eq. 2.17).

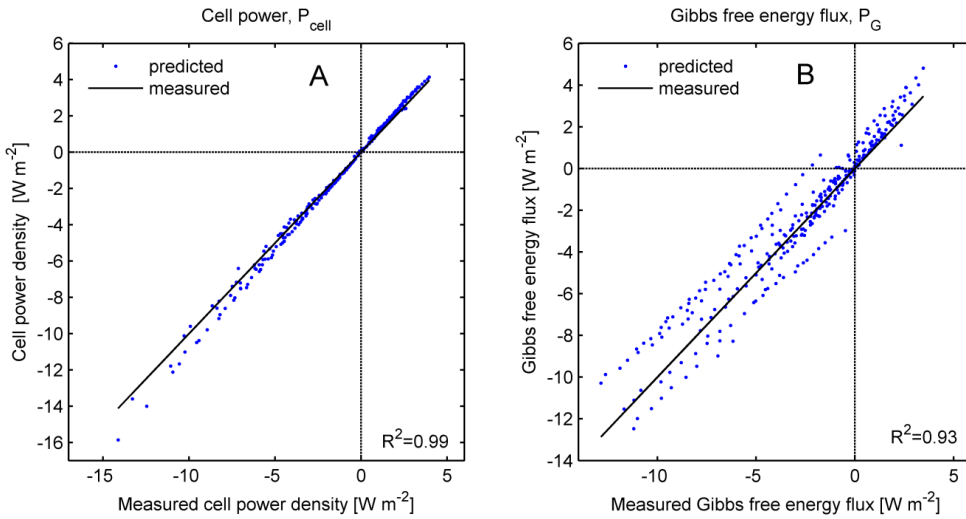


Figure 2.2. (A) Parity plot of cell power, P_{cell} . The x-axis shows the measured cell power and the y-axis shows cell power. Measured values are plotted as straight line to guide the eye. Predicted values (\bullet) show the calculated cell power. (B) Parity plot of the Gibbs free energy flux, P_G . The x-axis shows the measured Gibbs free energy flux and the y-axis shows Gibbs free energy flux. Measured values (straight line) are plotted to guide the eye. Predicted values (\bullet) show the calculated cell power.

Although a good fit is obtained for both P_{cell} and P_G , this is not sufficient to conclude that our model gives a proper mechanistic description of the underlying transport processes. Therefore, we present further reasoning to show that the linear approximation used in our description is adequate to describe operation of the CGFB system. First of all, our model has a theoretical basis, and the parameter values are in line with literature values. Second, our model describes charge

and discharge modes using a single set of parameters over a wide range of salt concentration gradients and correctly predicts the intercept of water transport to be equal to zero.

2.4.3 Evaluation of the thermodynamic efficiency

In this section we discuss the thermodynamic efficiency of the CGFB system which is expressed as the Gibbs free energy, G (J kg^{-1}). Experimental results are presented for sixteen different combinations of concentrate (0.5, 1, 2 and 3 mol kg^{-1}) and diluate (0.025, 0.05, 0.1 and 0.25 mol kg^{-1}) concentrations and at different current densities. Figure 2.3A shows experimental results at fixed dilute concentration of 0.25 mol kg^{-1} .

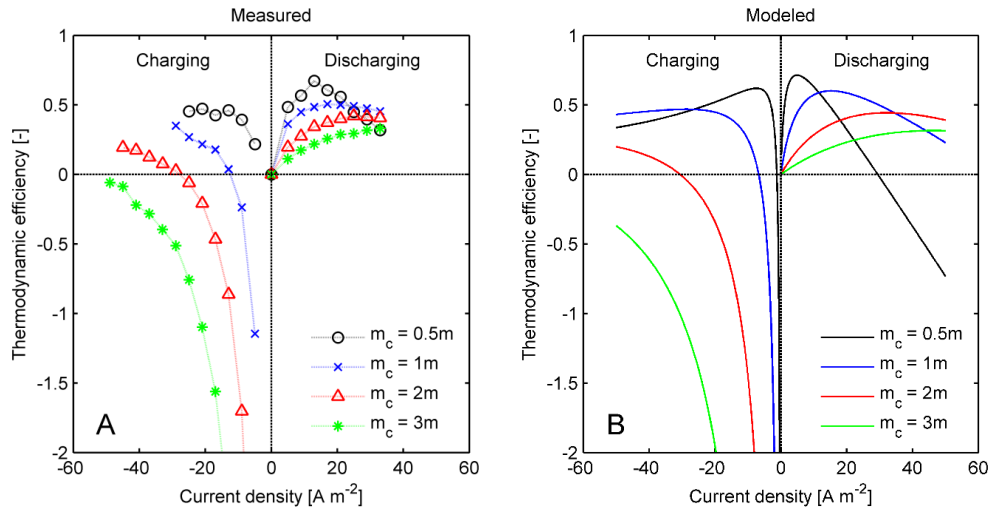


Figure 2.3. (A) measured and (B) simulated thermodynamic efficiencies during charge and discharge modes as function of current density for different values of concentrate concentrations. In panel A and B, the salt concentration of the diluate is fixed and equals 0.25 mol kg^{-1} . In panel (A) lines serve to guide the eye.

Figure 2.3A shows that during the discharging step, the thermodynamic efficiency increases with increasing current density. The maximum value of 0.75 is reached when the concentrate concentration equals 0.5 mol kg^{-1} . We also observed that the maximum efficiency decreases with increasing concentrate concentration. In Figure 2.3A and B we find a negative thermodynamic efficiency during charging at low current densities. This is because the Gibbs free energy stored in the system is small compared to the losses (diffusion, osmosis and internal resistance). Therefore, there will be no net energy storage at low current densities. At a certain current density, the efficiency becomes zero. This “zero efficiency current density” increases in absolute terms with increasing concentrate concentration. A zero thermodynamic efficiency means that the quantity of Gibbs free energy stored equals the power losses due to dissipation. With increasing current densities, the thermodynamic efficiencies increase and seem to converge, and pronounced maxima are not observed. The maximum thermodynamic efficiency is observed at concentrate concentration of 0.5 mol kg^{-1} . In all cases plotted in Figure 2.3 we note that the

maximum discharging efficiency at a given concentrate concentration is higher than the associated charging efficiency. Similar experiments which were performed at other diluate concentrations show similar trends.

In Figure 2.3B we show theoretical calculations of the predicted thermodynamic efficiency at the same conditions as in Figure 2.3A. We find good agreement between experimental and modelling data. For example, in Figure 2.3B we find that thermodynamic efficiency is equal to zero when current density is also zero, and a pronounced maximum and further drop below zero is observed at the lowest concentrate concentration of 0.5 mol kg^{-1} . During the charging step negative efficiencies are predicted at low current density. In Figure 2.3B we also see that the theoretical lines at concentrate concentrations of 0.5 and 1 mol kg^{-1} converge at current density of around 27 A m^{-2} .

To obtain a storage system one would like to use high concentrate concentrations as this gives the highest energy storage capacity. However especially the efficiencies for charging are very low at higher concentrations. The maximum thermodynamic efficiency of 0.5 is reached at concentrate concentrations 0.5 and 1 mol kg^{-1} . For the same salt concentrations, the thermodynamic efficiency of the discharge step is always higher than that of the charging step. Nevertheless, for a competitive storage system both thermodynamic efficiencies are too low, especially at higher salt concentrations. In all cases, low thermodynamic efficiencies indicate high energy dissipation. As the thermodynamic efficiency is a clear function of the concentrate concentration and current density (see Figure 2.3A and 3B), energy dissipation mechanisms need to be studied and a connection should be established in relation to these variables. The contribution of different fluxes to the energy dissipation will be identified and quantified in the next section. To the best of our knowledge, the presented method of analysis is novel, and may serve as a starting point for further improvements of the CGFB system.

2.4.4 Flux analysis of the CGFB

As discussed in section 4.2, the Gibbs free energy of a solution, $G \text{ (J kg}^{-1}\text{)}$, is a function of molality. Based on eq. 2.19, the total power dissipation consists of three components; (i) dissipation due to water transport, (ii) non-ideal transport of salt through the membranes, and (iii) internal resistance. In this section we analyse these contributions based on calculated values of water and salt fluxes and the corresponding values of chemical potentials, and membrane potential.

In Figure 2.4 the negative current density corresponds to the charging step while the positive current describes the discharging phase. The black line shows the dissipated power due to an internal resistance. The blue line is the sum of power dissipation due to internal resistance and non-ideal salt transport. The difference between the blue and black line is thus the power loss due to non-ideal salt transport. The red line is the total power dissipation including internal resistance, non-ideal salt transport and water transport. The difference between the red and the blue line represents the power dissipation caused by water transport. Finally, the green line shows

the total Gibbs free energy flux for discharging, whereas for charging the green line describes the cell power. The difference between the green and the red line corresponds to the extracted power during discharging and to the power storage during charging.

In Figure 2.4 we show results of such an analysis. In Figure 2.4A we see that the blue and red lines nearly coincide with the black line, indicating that the dominant dissipation mechanism is internal resistance, while non-ideal salt transport and water transport contributions are low. This can be explained by the mostly small concentration gradient in the system. The dissipation by internal resistance rises with increasing current density. We see that the black line has a parabolic shape and is symmetric with respect to the y-axis because of a similar internal resistance for both charge and discharge steps. We see that the internal resistance is nearly equal in all cases. This is because its value is hardly influenced by the concentrate concentration, as the concentrate compartment has a high conductance compared to the diluate compartment. During the charging step, we see that the power storage is positive, while during discharge the power extraction becomes negative at higher current densities. From this point on the power extracted is less than the power dissipated. The point of zero thermodynamic efficiency is achieved at current density of 27 A m^{-2} .

Figure 2.4 shows that higher concentrate concentrations contribute to higher total power dissipation at all current densities. In Figure 2.4 we see that higher concentration differences between the two solutions lead to higher water and co-ions transport. This is explained by increased osmosis and diffusion. The power dissipation due to internal resistance seems not affected much by the increase in concentrate concentration. This result is expected since the conductivity increase in the concentrate compartment with increasing salt concentrations is very small. At zero current density, the Gibbs free energy flux equals the energy dissipation as at this condition power is not extracted. Figure 2.4 also shows that no power is extracted due to zero current density. Because of this positive dissipation, the thermodynamic efficiency of the discharge step will always be zero at zero current density and at lower current densities the thermodynamic efficiency remains positive. As the internal resistance dissipation line is parabolic and the total Gibbs free energy flux [G] nearly linear with current density, there will always be an intersection point between the Gibbs free energy flux and the total power dissipation line [W] indicating point at which the thermodynamic efficiency equals zero. Please note that this intersection point shifts to higher current densities as concentration difference increases. Based on results presented in Figure 2.4, it becomes clear that the power dissipation strongly depends on the concentrate concentration. Experimental data which were obtained at other diluate concentrations shows similar trends as Figure 2.4.

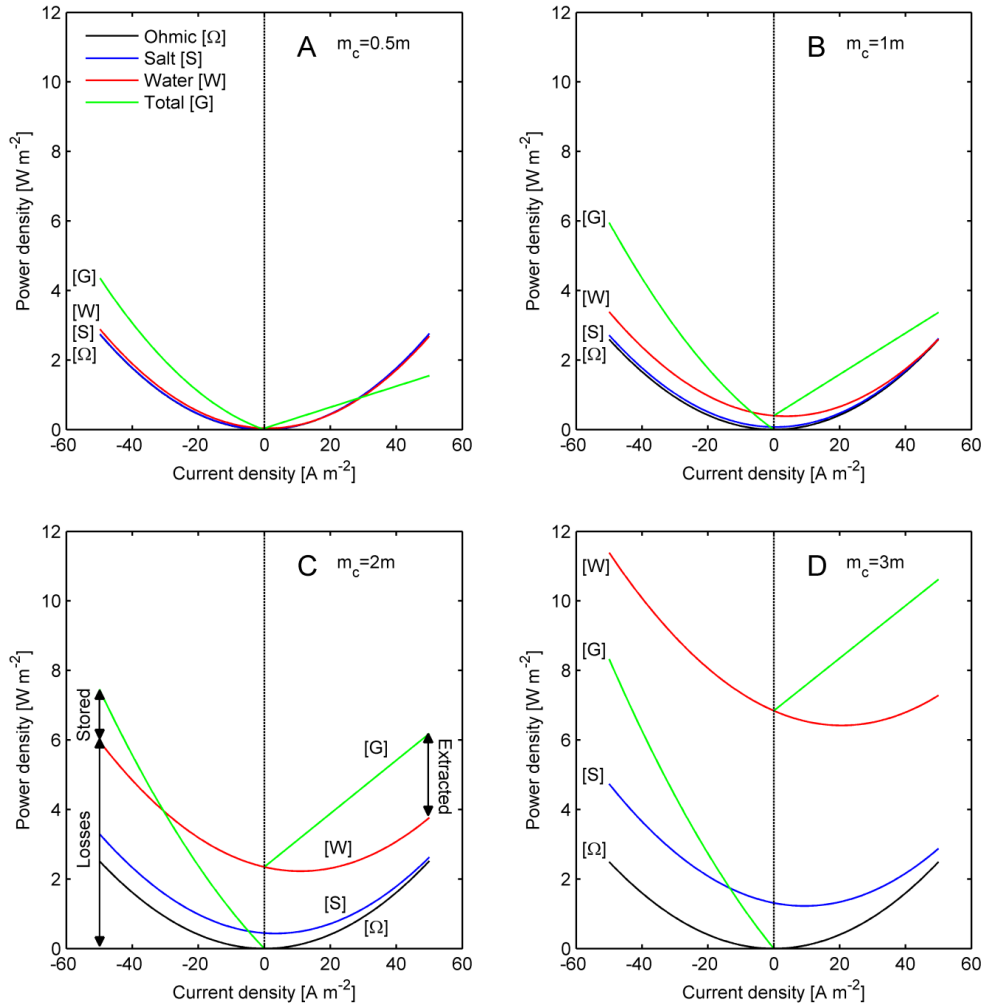


Figure 2.4. Power dissipation as function of current density during operation of CGFB shown as internal resistance $[\Omega]$, internal resistance + non-ideal salt transport $[S]$ and internal resistance + non-ideal salt transport + water transport $[W]$. Total cell power or total Gibbs free energy flux is shown for the charging and discharging step, respectively. In all panels salt concentration of the diluate is fixed and equals 0.25 mol kg^{-1} , whereas the concentrate concentration is different in each panel. Negative current density corresponds to the charging step while positive current density describes discharging.

During charging we note that when the applied power is zero, then current density is also zero, while the power dissipation stays always positive, leading to negative efficiencies at low current densities. The intersection of the total power dissipation and the applied power indicates a point where the thermodynamic efficiency equals zero. As power dissipation increases with increasing concentrate concentration, the point of zero thermodynamic efficiency shifts to higher current densities.

Both the power dissipation due to water transport and non-ideal salt transport seem to decrease with increasing current density for the discharging step. This can be partly explained by water molecules which are being transported via electro-osmosis, restoring the concentration difference. Thus, during the discharging step, the effect of osmosis is diminished by electro-osmosis and this increases the thermodynamic efficiency. During the charging step the opposite process occurs, namely, electro-osmosis is diminishing the concentration gradient and thus contributes to power dissipation. We also note that lower power dissipation due to non-ideal salt transport is a result of the potential gradient which develops in the membrane due to the increased transport of counterions (see Figure 2.1 where at the right-hand side $I > 0$).

In a non-ideal IEM at zero current density there is no charge being transported and salt transport occurs mostly by diffusion, the rate of which is limited by membrane diffusion of co-ions. With increasing current density, the transport mechanism changes and the transport of counterions gives rise to a potential drop inside the IEM. This potential drop will increase the transport rate of counterions, while decreasing the transport of co-ions and thus decrease the power dissipation due to non-ideal salt transport. However, during charging, the developed potential gradient is reversed ($I < 0$) which leads to enhanced co-ion transport and at the same time higher power dissipation. This asymmetry related to different water and co-ion transport explains different efficiencies of the charging and discharging step.

In summary, in this section we showed that the steady state experimental approach in combination with flux analysis can serve as a powerful tool in explaining different thermodynamic efficiencies.

We showed that CGFB efficiency is lower when salt concentration is higher, that negative and zero thermodynamic efficiencies are possible and finally that our analysis allows us to quantify the importance of the different sources of power dissipation as function of current density. Our analysis implies that the charging and discharging steps should be performed at optimum current densities which are a function of concentration difference. At first glance charging at higher and discharging at lower power seems acceptable for a large-scale energy storage system, since the duration of the optimum solar power output is a small portion of the whole day.

2.4.5 Influence of different sources of power dissipation at maximum CGFB efficiency

The previous section we showed that for a given concentrate concentration the value of the maximum efficiency depends on the current density.

In Figure 2.5A we show the optimal current density as function of the concentrate concentration. Current for the charging step is represented as positive values for easy comparison with the discharging step. Figure 2.5A shows that the optimal current density for the charging and discharging step increases with increasing salt concentration. The optimal current density increase during charging is faster than during discharging. This is due to the fact that the charging

step starts with a negative efficiency and needs increasingly higher current densities just to counteract the power dissipation due to growing water and co-ion transport with increasing concentration.

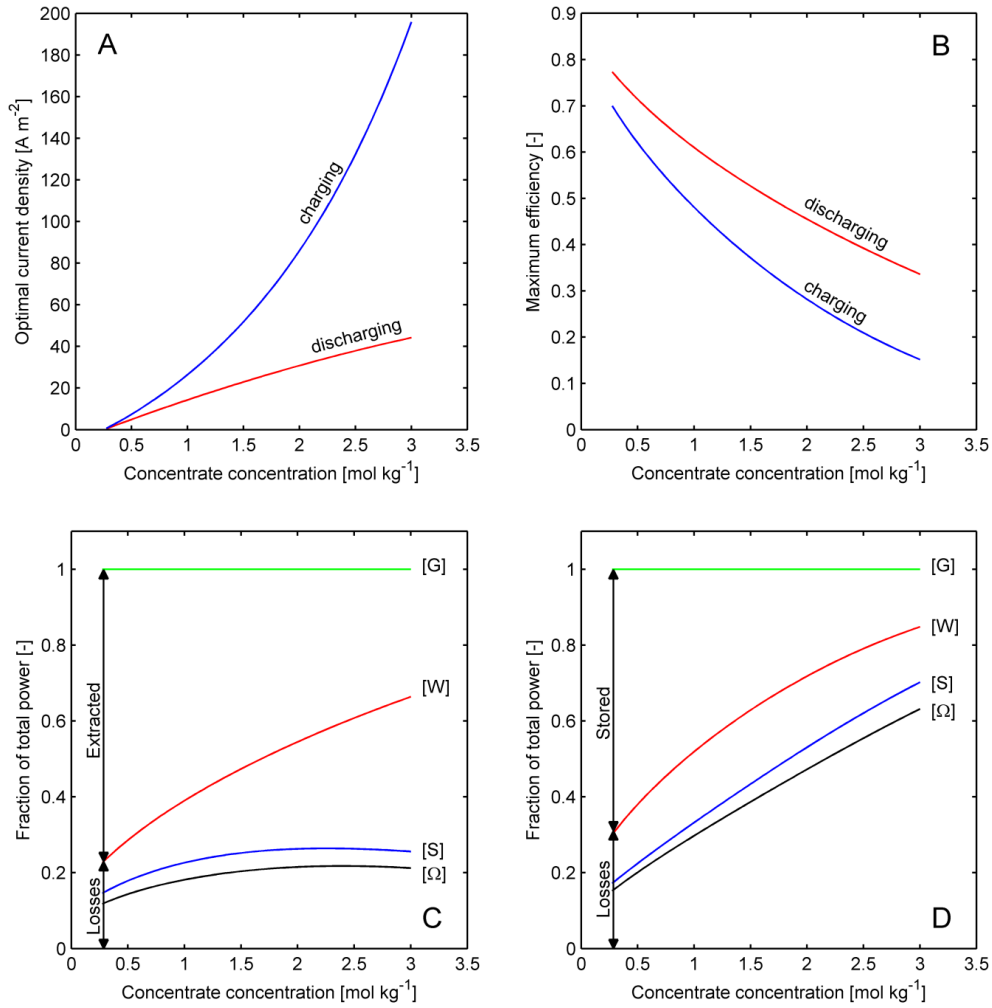


Figure 2.5. (A) Optimal current density and (B) maximum efficiency for charging and discharging step as function of concentrate concentration, m_c . (C) Power dissipation in discharging step and (D) charging step including losses due to internal resistance [Ω], internal resistance + salt transport [S] and internal resistance + salt transport + water transport [W] and total Gibbs energy flux [G] as function of concentrate concentration, m_c . Salt concentration of the diluate is fixed and equals 0.25 mol kg⁻¹.

In Figure 2.5B we show the maximum efficiency at a given concentrate concentration. The maximum efficiency drops with increasing concentration, both for the charging and discharging

step. The charging efficiency is lower than discharging due to the higher power dissipation by osmosis and salt flux.

Figure 2.5C shows the importance of the different sources of power dissipation. In the discharging phase we see that with increasing concentrate concentration, power dissipation mostly occurs via osmotic water flow. Contributions of the salt flux and internal resistance to the power dissipation remain stable when the concentrate concentration is higher than 1.5 mol kg^{-1} . The large contribution of osmosis to the power dissipation and modest contribution of the unwanted salt transport was also reported by Kingsbury et al.¹³ Figure 2.5D shows that losses via the internal resistance increase strongly with increasing concentrate concentration, while other losses remain nearly the same. We explain this result by the fact that during the charging step much higher current densities are needed to reach optimal performance and thus the charge transport losses are more important during charging.

2.5 Conclusions

In this work we have shown that to achieve high energy density with CGFB, high salt concentration gradients are necessary. We demonstrate that the state of the art ion-exchange membranes are not capable of delivering sufficiently high thermodynamic efficiency. The main reason for sub-optimal efficiencies during the discharge step is water transport. In order to improve the performance of the discharge step it is necessary to use ion-exchange membranes with lower water permeability. We also note that to reach modest efficiencies during the charging step high current density should be applied to the CGFB system to minimize water transport. On the other hand, a high current density in the charging step leads to higher power dissipation due to charge transport. Thus, for an efficient operation of the CGFB system, charge and discharge should be performed at different current densities.

Our study also shows that lowering the internal resistance would improve mostly the performance of charging step, and to some extent also the performance of the discharge step. Lower internal resistance can be achieved by reducing the volume of the two solution compartments. However, when the distance becomes smaller than a certain value, energy consumption due to pumping would strongly increase. The use of thin spacers inside a CGFB system would be beneficial to reduce the water flow because the optimum efficiency would be reached at lower current densities resulting in lower power dissipation via the charge transport.

With current state of the art ion-exchange membranes the CGFB is not expected to reach competitive performance. The thermodynamic efficiencies reported in this work are too low to achieve an economically feasible energy storage system. Development of an ion-exchange membrane with low water transport and low resistance would be a first step in realizing the potential of the CGFB and therefore we believe that further progress in this direction is needed.

Acknowledgements

This work was performed in the cooperation framework of Wetsus, European Centre of Excellence for Sustainable Water Technology (www.wetsus.nl). Wetsus is co-funded by the Dutch Ministry of Economic Affairs and Ministry of Infrastructure and Environment, the Province of Fryslân and the Northern Netherlands Provinces. The authors like to thank the participants of the research theme “Blue Energy” for the fruitful discussions and their financial support. In addition, the authors like to thank Maarten Biesheuvel and Michele Tedesco for the valuable discussions.

2.6 References

- (1) Sternberg, A.; Bardow, A. *Energy Environ. Sci.* **2015**, 8 (2), 389–400.
- (2) Carbajales-Dale, M.; Barnhart, C. J.; Benson, S. M. *Energy Environ. Sci.* **2014**, 7 (5), 1538–1544.
- (3) Dunn, B.; Kamath, H.; Tarascon, J.-M. *Science (80-.)*. **2011**, 334 (6058), 928–935.
- (4) Chatzivassileiadi, A.; Ampatzi, E.; Knight, I. *Renew. Sustain. Energy Rev.* **2013**, 25, 814–830.
- (5) Beaudin, M.; Zareipour, H.; Schellenberglobe, A.; Rosehart, W. *Energy Sustain. Dev.* **2010**, 14 (4), 302–314.
- (6) Ibrahim, H.; Ilinca, A.; Perron, J. *Renew. Sustain. Energy Rev.* **2008**, 12 (5), 1221–1250.
- (7) Whittingham, M. S. *MRS Bull.* **2008**, 33 (4), 411–419.
- (8) Hadjipaschalis, I.; Poullikkas, A.; Efthimiou, V. *Renew. Sustain. Energy Rev.* **2009**, 13 (6–7), 1513–1522.
- (9) Rahman, F.; Rehman, S.; Abdul-Majeed, M. A. *Renew. Sustain. Energy Rev.* **2012**, 16 (1), 274–283.
- (10) Chen, H.; Cong, T. N.; Yang, W.; Tan, C.; Li, Y.; Ding, Y. *Prog. Nat. Sci.* **2009**, 19 (3), 291–312.
- (11) Corcuera, S.; Estornés, J.; Menictas, C. In *Advances in Batteries for Medium and Large-Scale Energy Storage*; Lim, C. M. S.-K. M., Ed.; Woodhead Publishing, 2015; pp 29–53.
- (12) Tedesco, M.; Hamelers, H. V. M.; Biesheuvel, P. M. *J. Memb. Sci.* **2016**, 510, 370–381.
- (13) Kingsbury, R. S.; Chu, K.; Coronell, O. *J. Memb. Sci.* **2015**.
- (14) Post, J. W.; Veerman, J.; Hamelers, H. V. M.; Euverink, G. J. W.; Metz, S. J.; Nymeijer, K.; Buisman, C. J. N. *J. Memb. Sci.* **2007**, 288 (1–2), 218–230.
- (15) Galama, A. H.; Post, J. W.; Hamelers, H. V. M.; Nikonenko, V. V.; Biesheuvel, P. M. *J. Membr. Sci. Res.* **2015**.
- (16) Veerman, J.; Post, J. W.; Saakes, M.; Metz, S. J.; Harmsen, G. J. *J. Memb. Sci.* **2008**,

310 (1–2), 418–430.

- (17) Galama, A. H.; Vermaas, D. A.; Veerman, J.; Saakes, M.; Rijnaarts, H. H. M.; Post, J. W.; Nijmeijer, K. *J. Memb. Sci.* **2014**, 467 (0), 279–291.
- (18) Długołęcki, P.; Gambier, A.; Nijmeijer, K.; Wessling, M. *Environ. Sci. Technol.* **2009**, 43 (17), 6888–6894.
- (19) Strathmann, H. *Ion-exchange membrane separation processes*; Elsevier: Amsterdam, 2004; Vol. 9.
- (20) Strathmann, H. *Desalination* **2010**, 264 (3), 268–288.
- (21) Vermaas, D. A.; Saakes, M.; Nijmeijer, K. *Electrochim. Acta* **2014**, 117, 9–17.
- (22) Vermaas, D. A.; Saakes, M.; Nijmeijer, K. *Environ. Sci. Technol.* **2011**, 45 (16), 7089–7095.
- (23) Vermaas, D. A.; Saakes, M.; Nijmeijer, K. *J. Memb. Sci.* **2014**, 453 (0), 312–319.
- (24) Długołęcki, P.; Nijmeijer, K.; Metz, S.; Wessling, M. *J. Memb. Sci.* **2008**, 319 (1–2), 214–222.
- (25) Daniilidis, A.; Vermaas, D. A.; Herber, R.; Nijmeijer, K. *Renew. Energy* **2014**, 64 (0), 123–131.
- (26) Veerman, J.; Saakes, M.; Metz, S. J.; Harmsen, G. J. *Chem. Eng. J.* **2011**, 166 (1), 256–268.
- (27) Tedesco, M.; Cipollina, A.; Tamburini, A.; Bogle, I. D. L.; Micale, G. *Chem. Eng. Res. Des.* **2015**, 93 (0), 441–456.
- (28) Tedesco, M.; Cipollina, A.; Tamburini, A.; van Baak, W.; Micale, G. *Desalin. Water Treat.* **2012**, 49 (1–3), 404–424.
- (29) Güler, E.; Elizen, R.; Vermaas, D. A.; Saakes, M.; Nijmeijer, K. *J. Memb. Sci.* **2013**, 446 (0), 266–276.
- (30) Galama, A. H.; Saakes, M.; Bruning, H.; Rijnaarts, H. H. M.; Post, J. W. *Desalination* **2014**, 342, 61–69.
- (31) Veerman, J.; De Jong, R. M.; Saakes, M.; Metz, S. J.; Harmsen, G. J. *J. Memb. Sci.* **2009**, 343 (1), 7–15.
- (32) Pitzer, K. S.; Mayorga, G. *J. Phys. Chem.* **1973**, 77 (19), 2300–2308.
- (33) Blandamer, M. J.; Engberts, J. B.; Gleeson, P. T.; Reis, J. C. *Chem Soc Rev* **2005**, 34 (5), 440–458.
- (34) Biesheuvel, P. M. *J. Colloid Interface Sci.* **2011**, 355 (2), 389–395.
- (35) Galama, A. H.; Post, J. W.; Stuart, M. A. C.; Biesheuvel, P. M. *J. Memb. Sci.* **2013**, 442, 131–139.

Supplementary information chapter 2

S2.1 Pitzer model

For easy reference, here the original Pitzer equations and parameters are presented ³²:

$$\phi - 1 = |z_M z_X| f^\phi + m \left(\frac{2\nu_M \nu_X}{\nu} \right) B_{MX}^\phi + m^2 \frac{2(\nu_M \nu_X)^{\frac{3}{2}}}{\nu} C_{MX}^\phi \quad \text{eq. (S 1)}$$

$$\ln \gamma = |z_M z_X| f^\gamma + m \left(\frac{2\nu_M \nu_X}{\nu} \right) B_{MX}^\gamma + m^2 \frac{2(\nu_M \nu_X)^{\frac{3}{2}}}{\nu} C_{MX}^\gamma \quad \text{eq. (S 2)}$$

The number of ions in the formula of salt is represented by ν_M and ν_X and their respective charges by z_M and z_X . In addition, $\nu = \nu_M + \nu_X$.

$$f^\gamma = -A^\phi \left[\frac{I^{\frac{1}{2}}}{1 + bI^{\frac{1}{2}}} + \frac{2}{b} \ln \left(1 + bI^{\frac{1}{2}} \right) \right] \quad \text{eq. (S 3)}$$

$$f^\phi = -A^\phi \frac{I^{\frac{1}{2}}}{1 + bI^{\frac{1}{2}}} \quad \text{eq. (S 4)}$$

$$B_{MX}^\gamma = 2\beta_{MX}^0 + \frac{2\beta_{MX}^1}{\alpha^2 I} \left[1 - e^{-\alpha I^{\frac{1}{2}}} \left(1 + \alpha I^{\frac{1}{2}} - \frac{1}{2} \alpha^2 I \right) \right] \quad \text{eq. (S 5)}$$

$$B_{MX}^\phi = \beta_{MX}^0 + \beta_{MX}^1 e^{-\alpha I^{\frac{1}{2}}} \quad \text{eq. (S 6)}$$

$$C_{MX}^\gamma = \frac{3}{2} C_{MX}^\phi \quad \text{eq. (S 7)}$$

$$I = \frac{1}{2} \sum m_i z_i^2 \quad \text{eq. (S 8)}$$

$A^\phi = 0.392$ for water at 25°C, $b=1.2$, $\alpha=2$

Table S1. Pitzer parameters adapted from Pitzer and Mayorga ³².

Salt	β_{MX}^0	β_{MX}^1	C_{MX}^ϕ	m_{salt}
NaCl	0.0765	0.2664	0.00127	6
KCl	0.04835	0.2122	-0.00084	4.8

KNO ₃	-0.0816	0.0494	0.00660	3.8
KI	0.0746	0.2517	-0.00414	4.5
NaCH ₃ COOH	0.1426	0.3237	-0.00629	3.5
KCH ₃ COOH	0.1587	0.3251	-0.00660	3.5

S2.2 Salt transport

Derivation of eq. 2.8 starts with the Nernst-Planck equation ¹⁵

$$J_i = -D_i \left[\frac{dc_i(x)}{dx} + c_i(x) \frac{z_i F}{RT} \frac{dE}{dx} \right] \quad \text{eq. (S 9)}$$

with

$$\varepsilon = E \frac{F}{RT}$$

subscripts C and A denoting counterions and co-ions, capitals C and A denoting concentrations of counter and co-ions and assuming $D_C=D_A=D_m$ charge transport for monovalent ions can be described by

$$I_{mol} = J_C - J_A = -D_m \left(\frac{d}{dx} C + zC \frac{d}{dx} \varepsilon \right) + D_m \left(\frac{d}{dx} A - zA \frac{d}{dx} \varepsilon \right) = -D_m \left(\frac{d}{dx} (C - A) + z(C + A) \frac{d}{dx} \varepsilon \right) \quad \text{eq. (S 10)}$$

with $C = X_f + A$ the charge transport becomes

$$I_{mol} = -D_m \left(\frac{d}{dx} X_f + z(X_f + 2A) \frac{d}{dx} \varepsilon \right) \quad \text{eq. (S 11)}$$

Assuming that the fixed charge density, X_f , is fixed results in

$$I_{mol} = -D_m z (X_f + 2A) \frac{d}{dx} \varepsilon \quad \text{eq. (S 12)}$$

or

$$\frac{d}{dx} \varepsilon = - \frac{I_{mol}}{D_m z (X + 2A)} \quad \text{eq. (S 13)}$$

The salt transport is described by

$$J_s = J_C + J_A = -D_m \left(\frac{d}{dx} (C + A) + z(C - A) \frac{d}{dx} \varepsilon \right) \quad \text{eq. (S 14)}$$

with $C = X_f + A$, eq. (S 14) becomes

$$J_s = -D_m \left(\frac{d}{dx} (X_f + 2A) + zX_f \frac{d}{dx} \varepsilon \right) \quad \text{eq. (S 15)}$$

Assuming the fixed charge density, X_f , is fixed and substitution of eq. (S 13) gives

$$J_s = -D_m \left(\frac{d}{dx} (2A) + zX_f \frac{-I_{mol}}{D_m z (X + 2A)} \right) \quad \text{eq. (S 16)}$$

which can be rewritten to

$$J_s = -D_m \frac{d}{dx} (2A) + X_f \frac{I_{mol}}{(X + 2A)} \quad \text{eq. (S 17)}$$

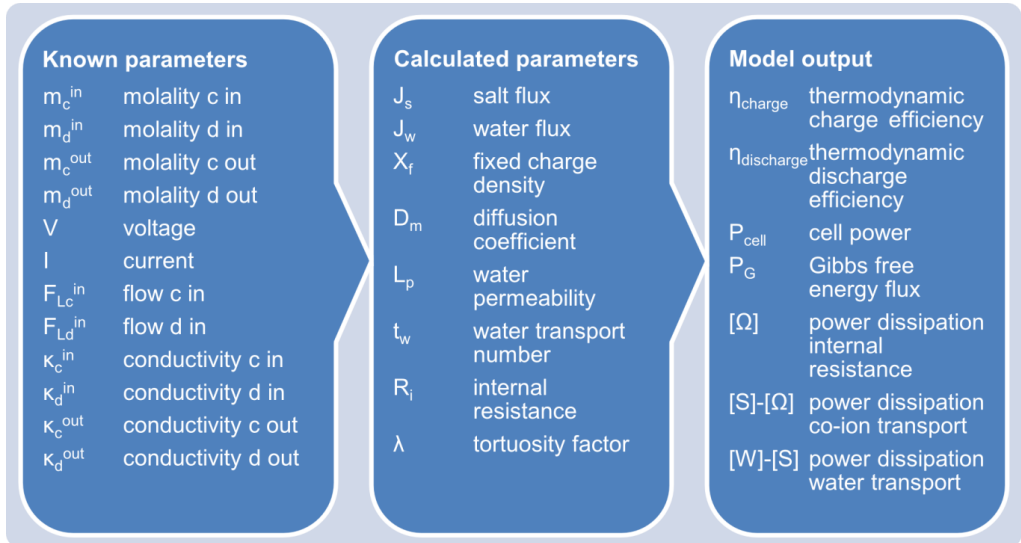
Finally, with

$$\beta = \frac{A}{X_f}$$

and integration over the membrane while assuming a linear concentration gradient, the salt transport is described by

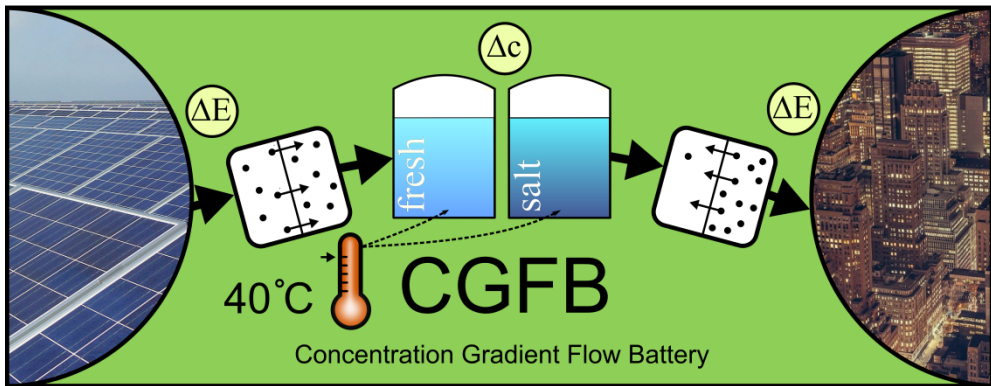
$$J_s = -\frac{2D_m X_f \rho_m}{\delta_m} (\beta_d - \beta_c) + \frac{I_{mol}}{1 + \beta_c + \beta_d} \quad \text{eq. (S 18)}$$

S2.3 Model flow chart summary



Chapter 3

Energy efficiency of a Concentration Gradient Flow Battery at elevated temperatures



This chapter is published as

van Egmond, W.J.; Starke, U.K.; Saakes, M.; Buisman, C.J.N.; Hamelers, H.V.M. “Energy efficiency of a concentration gradient flow battery at elevated temperatures”. *J. Power Sources* **2017**, 340, 71–79.

Abstract

Fast growth of intermittent renewable energy generation introduces a need for large scale electricity storage. The Concentration Gradient Flow Battery (CGFB) is an emerging technology which combines Electrodialysis with Reverse Electrodialysis into a flow battery which is able to safely store very large amounts of energy in environmental friendly NaCl solutions. In this work, (dis)charge efficiency, energy density and power density are both theoretically and experimentally investigated. Fifteen constant current experiments (-47.5 to $+37.5 \text{ A m}^{-2}$) are performed at 40°C and two experiments (-32.5 and 15 A m^{-2}) at 10 and 25°C . The magnitudes of the three main energy dissipation sources (internal resistance, water transport and co-ion transport) are measured and mitigation strategies are proposed. The effect of current density, state of charge and temperature on the dissipation sources is analysed. Water transport is shown to cause hysteresis, lower (dis)charge efficiencies and lower energy capacity. At constant current and with increasing temperature, internal resistance is reduced but unwanted water transport is increased. This study reports charge efficiencies up to 58% and discharge efficiencies up to 72%. Full charge or discharge of the battery is shown inefficient. The optimal operating range is therefore introduced and identified ($\Delta m > 0.5$ and $\eta > 0.4$).

3.1 Introduction

Production of renewable energy and the necessity to balance electricity production and consumption are driving development of various types of energy storage systems¹⁻⁵. One of the main challenges in this area is the required capacities of large scale electrical energy storage (EES) systems in the electricity grid. Recently, a concentration gradient flow battery (CGFB) was proposed as an environmental friendly EES system^{6,7}. A CGFB stores energy in two reservoirs filled with aqueous solutions of different salinity. This system stores power in two solutions with different concentrations using the Electro Dialysis (ED) process⁸⁻¹¹. The reverse process, Reverse Electro Dialysis (RED), must be carried out in order to discharge the CGFB¹²⁻¹⁴. The resulting battery is scalable, can be placed anywhere in the world and uses abundant materials only.

Figure 3.1 shows the concept of the CGFB during charging mode (ED mode). A completely discharged CGFB constitutes two aqueous reservoirs containing solutions with equal salt concentration, a so called 'stack' of alternately placed cation and anion exchange membranes and pumps. Both solutions are pumped through the stack and returned to their respective reservoir. The membranes contain fixed charges (represented schematically in figure 3.1 by + and - signs) which makes the membranes ion-selective. Cation exchange membranes allow cations to pass and block anions and anion exchange membranes allow anions to pass while blocking cations. An electric potential is applied over the outer electrodes (black bars) during charging. As a result, ions will move across the membranes in one stream becoming more concentrated (c,out) and one stream more diluted (d,out). In this way electric power is spent for creating one concentrated reservoir (salt) and one diluted reservoir (fresh). To discharge the CGFB, the current direction is reversed. Ions move in opposite direction and the solutions mix

under the influence of a concentration difference over the membranes. Power is harvested over the outer electrodes while the salinity difference decreases. Ionic current over the membranes needs to be converted to electric current at the electrodes. For this, redox reactions at the electrodes in a secondary solution take place. The secondary solution is circulated in a separated closed loop. In a true sized CGFB, any energy loss as result of the redox reaction is negligible. Therefore, these losses are excluded from this study.

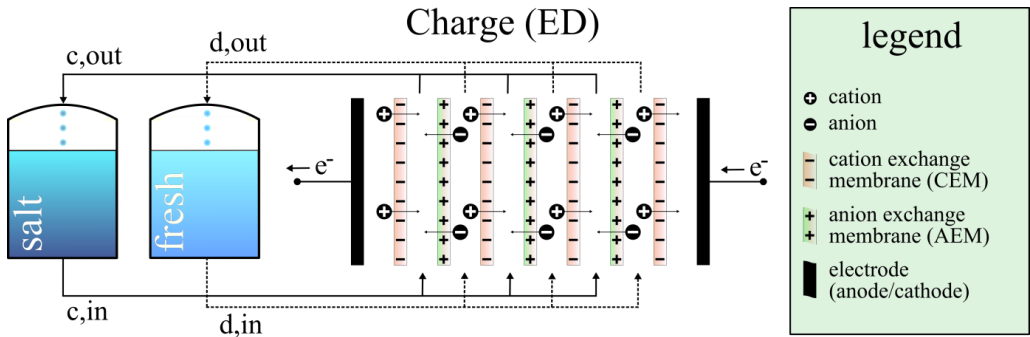


Figure 3.1. Conceptual drawing of a CGFB during a charging step. Two reservoirs on the left contain two solutions of different salinity (salt and fresh). The solutions coming out the concentrated (salt) reservoir (c_{in}) and the diluted (fresh) reservoir (d_{in}) are pumped into the ED/RED stack. An electric potential is applied over the electrodes and ions will move across the membranes resulting in a more concentrated solution (c_{out}) and more diluted concentration (d_{out}) leading to an increase in salinity difference between the reservoirs.

In the charge/discharge process, all mass transport takes place through the membranes. Three dissipation factors decrease the (dis)charge efficiency: internal resistance, water transport and co-ion transport⁷. Internal resistance is the result of the electric resistance over the membranes and solution compartments. Water transport consists of osmosis and electro-osmosis. Osmosis occurs over the membrane as a result of a concentration difference and always constitutes a potential energy loss since it decreases the salinity difference without harvesting power. Electro-osmosis is water transport as a result of water associated with ions in their mantle. Depending on the direction of ion transport, associated water can be transported against or along the concentration gradient. Co-ion transport refers to unwanted ion transport as result of diffusion over membranes because membranes are not perfectly charge selective.

Initial studies on CGFB performance^{6,7} show that the (dis)charge efficiency and power density of such systems are rather limited due to internal resistance and osmosis (< 40% round trip efficiency). Reduction of internal resistance is therefore a straightforward solution for increasing both (dis)charge efficiency and power density of a CGFB. Earlier work on RED and ED shows that the internal resistance can be significantly reduced by increasing operating temperatures^{15–21}. This study investigates experimentally how operating a CGFB at different current densities and at an elevated temperature of 40 °C affects instantaneous system internal resistance, mass transport, (dis)charge efficiency and energy density over complete charge/discharge cycles. It

also points out “hysteresis” of a CGFB, which is a result of water transport through the membranes from the fresh solution to concentrate solution preventing the battery from returning to its original state. In this work, the working range of salt concentration is limited to 1M NaCl, because operating the CGFB above that value leads to excessive energy losses due to osmotic water transport ⁷. Finally, an accurate mass transport measurement method is presented as well.

3.2 Theory of a CGFB

In this section, theory of a CGFB is presented. Important equations for energy density, mass transport and (dis)charge efficiency calculation are given and explained.

3.2.1 Energy density

Gibbs free energy of mixing becomes available when two solutions of different salinity mix inside a CGFB. The theoretical amount of energy ΔG_{mix} (J) that can be released during this process can be calculated according to

$$\Delta G_{mix} = G_{c,out} + G_{d,out} - G_{c,in} - G_{d,in} \quad \text{eq. (3.1)}$$

$$G_i = n_w \nu m R T (\ln(\gamma_{\pm} m) - \phi) \quad \text{eq. (3.2)}$$

where G_i is the total Gibbs energy of a solution i , n_w the number of kilograms of solvent, ν the number of types of ions in a solution, m the molality of a solution, R the universal gas constant, T temperature, ϕ the osmotic coefficient and γ_{\pm} the mean molal activity coefficient. The subscripts on the right-hand side of eq. 3.1 refer to the concentrate and dilute solutions flowing either in or out a CGFB. The osmotic and molal activity coefficients are a function of salt concentration and temperature. In this work the approach of Pitzer et al. ²² and Silvester et al. ²³ is used for calculating the coefficients at different temperatures.

3.2.2 Mass transport

In RED/ED there are 4 mass transport processes considered taking place across ion-exchange membranes ^{7,10,24,25}; (i) counter ion transport J_c , (ii) co-ion transport J_a , (iii) water osmosis J_{osm} and (iv) water electro-osmosis J_{e-osm} . Co-ion transport (or unwanted salt transport) is caused by a concentration and potential gradient across a membrane. This type of salt transport typically constitutes a loss in (dis)charge efficiency, since it decreases the concentration gradient. Osmotic water transport also contributes to lower (dis)charge efficiency, since it reduces the concentration gradient. Electro-osmotic water transport contributes to lower charge efficiency (ED mode), because it reduces the concentration gradient (as water is transported with ions from the dilute to concentrate solution). With RED mode, electro-osmotic water transport increases discharge efficiency, because it increases the concentration gradient. This is a result of ion transport taking place in reversed direction.

There are two types of membranes in a CGFB. This study assumes both membrane types have the same properties, except for the sign of fixed chemical charge. Based on this assumption, any

mass transport process which occurs across a cation exchange membrane (CEM) is therefore mirrored in an adjacent anion exchange membrane (AEM). Together both membranes constitute a cell pair.

Charge transport across an ion-exchange membrane and salt transport across a cell pair can be described respectively by⁷

$$I_{mol} = J_c - J_a \quad \text{eq. (3.3)}$$

$$J_s = J_c + J_a \quad \text{eq. (3.4)}$$

The molar current density I_{mol} (mol ionic charge $\text{m}^{-2} \text{s}^{-1}$ membrane) is the difference between counter ion and co-ion flux across a membrane and is calculated by dividing current density I_d (A m^{-2}) by Faradays constant F . The net salt transport J_s (mols of salt $\text{m}^{-2} \text{s}^{-1}$) represents the total amount of moles of salt transported across a cell pair.

Total water transport J_w ($\text{kg of H}_2\text{O m}^{-2} \text{s}^{-1}$) across a cell pair can be calculated according to

$$J_w = \overbrace{2L_p(-\Delta\mu_w)}^{\text{osmosis}} + \overbrace{J_s t_w M}^{\text{electro-osmosis}} \quad \text{eq. (3.5)}$$

where L_p is the average water permeability coefficient ($\text{kg m}^{-2} \text{s}^{-1} \text{kg J}^{-1}$) of both membrane types and $\Delta\mu_w$ the difference in chemical potential of the water (J kg^{-1})⁷ over the two sides of a membrane. The amount of water associated with transported ions across a membrane is expressed as t_w (mol of H_2O per mol of salt) and is referred to as electro-osmosis coefficient.

3.2.3 Power dissipation and (dis)charge efficiency

The amount of Gibbs free energy stored or released per second in or from the solutions, P_G (Gibbs power, $\text{J s}^{-1} \text{m}^{-2}$ cell pair), is calculated by

$$P_G = J_w(-\Delta\mu_w) + J_s(-\Delta\mu_s) \quad \text{eq. (3.6)}$$

where $\Delta\mu_s$ (J mol^{-1}) is the chemical potential difference of the salt of two solutions⁷ separated by an ion-exchange membrane. A more detailed explanation on how to calculate water and salt chemical potential differences, $\Delta\mu_w$ and $\Delta\mu_s$, is provided in Ref.⁷. Next to co-ion and water transport (section 2.2), internal resistance is also a major source of power dissipation. To discriminate the contributions of each dissipation factor in Gibbs power, equation 3.6 can be split up into

$$P_G = \overbrace{J_w(-\Delta\mu_w)}^{\text{water transport}} + \overbrace{J_a(-\Delta\mu_s)}^{\text{co-ion transport}} + \overbrace{J_c(-\Delta\mu_s) - I_d E_{cell}}^{\text{internal resistance}} + \overbrace{I_d E_{cell}}^{\text{cell power}} \quad \text{eq. (3.7)}$$

where P_G is the amount of Gibbs free energy stored (ED mode) in solution or Gibbs free energy released (RED mode) from solution per second. Cell power P_{cell} is the amount of electric power spent (ED mode) or electric power extracted (RED mode). Counter ion and co-ion transport, J_c and J_a can be calculated from combining eq. 3.3 and 3.4.

The discharge efficiency is defined as the ratio of electric power harvested over released Gibbs power, see eq. 3.8. The charge efficiency is given by the ratio of Gibbs power stored over electric power spent during charging, see eq. 3.9.

$$\eta_{RED} = \frac{P_{cell}}{P_G} \quad \text{eq. (3.8)}$$

$$\eta_{ED} = \frac{P_G}{P_{cell}} \quad \text{eq. (3.9)}$$

3.3 Materials and methods

3.1 Experimental setup

The experimental setup used in this study consists of a RED/ED stack, three peristaltic pumps, three reservoirs, three thermostatic baths, four conductivity meters, four pressure meters, two mass balances and a galvanostat. The stack is comparable to the one used in Ref. ²⁶. Inside the RED/ED stack four cation exchange membranes and three anion exchange membranes (CMX and AMX, Astom Corporation, Japan) are alternately placed between two endplates. Metal bolts were used to make the stack watertight. Between each membrane a silicone gasket with a thickness of 200 μm and spacer (Sefar AG, Switzerland) with a thickness of 180 μm and an open area of $\sim 50\%$ is placed. The endplates contain two titanium mesh electrodes coated with Ir/Ru (Magnet Special Anodes B.V., the Netherlands). The two salt water reservoirs are 500 ml glass bottles encapsulated by insulating foil. Both water reservoirs are placed on a mass balance connected to a computer which logs the mass. The rinse solution reservoir is a 1000 ml glass bottle, also encapsulated with insulating foil. All three reservoirs are separately connected to three dedicated thermostatic baths with spiral coils inside to control the temperature of all solutions. Two peristaltic pumps pump the salt water solutions sequentially through the spiral coils inside the thermostatic baths, separate pressure meters (Cerabar M, Endress+Hauser, Germany), conductivity meters (VERSA STAR, Thermo Fisher Scientific, USA), the RED/ED stack and another set of identical type of conductivity meters back to the bottles. Conductivity data is logged by a computer. The rinse solution is pumped by a separate peristaltic pump with two pump heads (one for the anode and another for the cathode compartment) sequentially through two pressure meters, through the RED/ED stack electrode compartments back to the bottle. To avoid any parasitic short-circuit currents, additional tubing is used before and after the RED/ED stack. In addition, tubing is insulated with foil to keep the temperature as constant as possible. Any change in temperature of each solution due to travelling from the thermostatic bath

to the stack, is taken into account by careful adjustment of the temperature inside the thermostatic bath. This ensures that the temperature of each solution inside the stack is correct during experiments. The galvanostat (Ivium Technologies, the Netherlands) is used to control current and measure potential across the RED/ED stack. Two reference electrodes (QM711X, QIS, the Netherlands) are placed in the electrode compartments in the middle of the endplates. The salt water solutions are prepared using NaCl of 99.5% purity (ESCO, the Netherlands) and the rinse solutions are prepared with laboratory grade Na₂SO₄ (VWR, the Netherlands). All water used in this work is demineralized.

3.2 Experimental procedure

In total, fifteen constant current ED and RED experiments are performed with solutions being recycled continuously. Six ED experiments at 40 °C are performed at current densities ranging from -10 A m⁻² to -47.5 A m⁻² with steps of -7.5 A m⁻² first. Salt water bottles are filled with 250 g of 0.5 molal NaCl solutions at the beginning of each experiment. The stack and tubing are also filled with 0.5 molal NaCl solution and the amount of solution inside is carefully measured. Salt solutions are pumped with a rate of 35 ml min⁻¹ and rinse solution is pumped at a rate of 255 ml min⁻¹. Once electrical current is applied across the RED/ED stack, mass and conductivities of the solutions are logged. During the charging experiment, one solution gets diluted and the other concentrated. Once the diluate reaches below 0.01 molal, the experiment is considered finished. Data analysis of the ED experiments found that a current density of -32.5 A m⁻² gives a high charge efficiency. At the end of this experiment the masses and concentrations of both solutions in the bottles and inside the tubing and stack are measured. These masses and concentrations serve as a starting point to perform RED experiments. In total, five RED experiments are performed at 40 °C with current densities ranging from 7.5 A m⁻² to 37.5 A m⁻² with steps of 7.5 A m⁻². The starting concentrations are 0.02 and 0.85 molal for the diluate and concentrate respectively. The RED experiments are considered finished when the measured voltage reaches zero. Data analysis of the RED experiments identifies 15 A m⁻² to be the current density close to the optimal discharge efficiency. For both selected current densities (-32.5 and 15 A m⁻²) the same experiments are repeated at 25 °C and 10 °C. The results are highly reproducible. For detailed information see the Supplementary Information for an example duplo experiment with a newly built stack. The standard average standard deviations for the individual datasets are: voltage, 0.01, mass, 0.23 and solution conductivity, 0.003.

3.3 Data analysis

Since the mass and concentrations of the solutions are known during operation of the CGFB, information about water mass change and salt content can be extracted at each time step. By dividing these mass transfers by the active ion-exchange membrane area of the stack, the water flux J_w and salt flux J_s is calculated. The flux of salt and water originates from the processes occurring inside the stack. Since the solutions take some time to travel from the bottle to the stack and back, these delays are carefully measured and taken into account by shifting the datasets appropriately to make sure that all readings (voltage, mass and conductivity) are well

aligned. By doing so it is made sure that any measured mass change of the bottles caused by mass transports inside the RED/ED stack is properly linked.

3.4 Results and Discussion

3.4.1 Energy capacity of and ideal CGFB

The energy content of an ideal CGFB during a full charge step is shown in figure 3.2. Since a concentration gradient flow battery is evaluated, the difference in concentration Δm (difference in molality) is a straightforward way for assessing the state of charge of the battery. When a battery is charged, a concentration gradient develops. Ideally, there would be only salt transport and no water transport. The stored Gibbs free energy of mixing ΔG_{mix} is shown at the y-axis of figure 3.2 and the concentration difference Δm is shown on the x-axis.

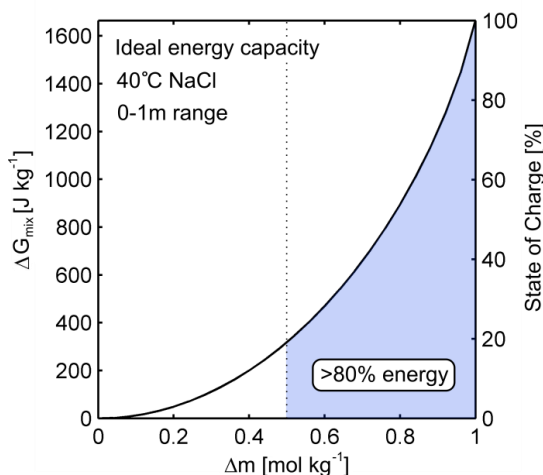


Figure 3.2. Energy density of an ideal CGFB battery. Starting solutions are two solutions of 0.5 kg water and a concentration of 0.5m NaCl. The left y-axis shows the total amount of Gibbs free energy of mixing (G_{mix}) stored in both solutions ($J\ kg^{-1}\ solvent$) as function of Δm . The right y-axis shows the state of charge (SoC) that is expressed as a percentage of the maximum amount of energy stored in the battery.

Interestingly, figure 3.2 shows that the majority of energy is stored at the end of the charging step. Halfway charging, at $\Delta m=0.5$, only about 20% of the theoretical capacity is filled. In section 4.2 the effect of the distribution of energy capacity with Δm on process performance is discussed in more detail.

3.4.2 Power dissipation as function of Δm during charge and discharge

With accurate measurements of mass transport, electrical current, cell voltage and theory given in section 2 and Ref. ⁷, it is possible to calculate the instantaneous contribution of each major dissipation source and instantaneous (dis)charge efficiency of the process over full charge and discharge cycles.

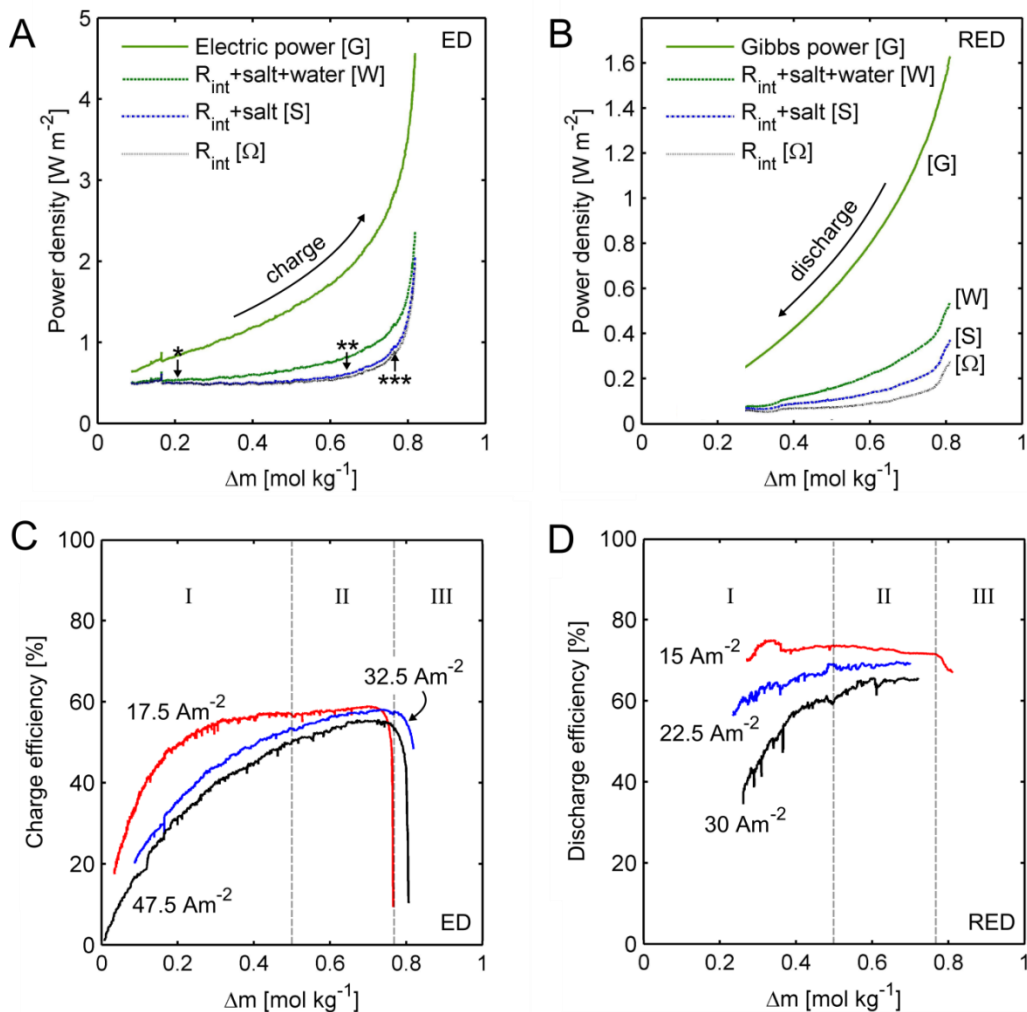


Figure 3.3. (A and B). Experimental results of a full charge (A) step at 32.5 A m⁻² and discharge (B) step at 15 A m⁻². The x-axis shows the molality difference Δm and the y-axis the power lost or gained expressed in power per membrane area (W m⁻²). R_{int} [Ω] shows the power lost as a result of internal resistance. The power lost by co-ion diffusion is given by the difference between the blue [S] and black [Ω] curve. Power loss caused by water transport is given by the difference between [W] and [S]. The difference between total spent electric power [G] and total dissipation losses [W] is the chemical power stored. For figure B the losses are described in the same manner as in A, except that [G] represents the total chemical power lost and the difference between [G] and [W] represents total electric power harvested. (C and D). Figure C and D show the (dis)charge efficiency of charging and discharging at three current densities respectively. Also, three zones are indicated by I-III.

Figures 3.3A and 3.3B show experimental results of a full charge (A) and discharge (B) step at current densities of -32.5 A m⁻² and 15 A m⁻² at 40°C. The y-axis shows the power lost or gained expressed in power per square meter of membrane area. For easy comparison the power values at charge mode are expressed as positive values.

Power lost as a result of internal resistance R_{int} is represented by the black curve $[\Omega]$. At the end of a charge step, Δm is high and the fresh water becomes strongly diluted. As a result, internal resistance of the diluate compartment increases rapidly and explains the steep increase of $[\Omega]$ at high Δm (see annotation (***)).

The curve showing power lost by co-ion transport and internal resistance together $[S]$ is plotted on top of the internal resistance curve $[\Omega]$. The difference between $[S]$ and $[\Omega]$ is the power lost by co-ion transport only. With increasing Δm , co-ion transport increases because of diffusion and this causes additional power loss. At annotation (**) the increasing power loss due to co-ion transport becomes visible.

Power loss caused by water transport is given by the difference between curve $[W]$ and $[S]$. In charging (ED) mode, both osmosis and electro-osmosis cause water transport power losses whereas in discharging (RED) mode the electro-osmosis counteracts part of the power loss caused by osmosis (also refer to section 2.2). Therefore, power loss by water transport is always higher during charging then during discharging. The effect of increasing power loss due to increasing osmosis with increasing Δm is clearly visible in figures 3.3 A and B. Annotation (*) indicates where power loss by water transport becomes visible for the charging step. Osmosis is also responsible for the fact that a CGFB does not reach a Δm of 1. This is because the concentrate solution is being diluted.

During charging, the total electric power which is fed into the battery is given by curve $[G]$. The difference between curve $[G]$ and the curve combining all losses $[W]$ is the power actually stored as chemical energy. During discharge, the total chemical power released by mixing is given by curve $[G]$. Here, the difference between curve $[G]$ and the curve combining all losses $[W]$ is the power actually harvested as electric power.

3.4.3 Charge efficiency and discharge efficiency as function of Δm

The ratios of chemical power stored over electric power spent (ED mode) or electric power harvested over chemical power spent (RED mode) determine the (dis)charge efficiency of the CGFB (also refer to eq. 3.8 and 3.9). Figures 3.3C and D show (dis)charge efficiencies for three selected current densities for both charge (3C) and discharge (3D).

All curves in figure 3.3C have the same shape. First efficiency increases steeply (zone I) followed by a region where efficiency levels off and reaches its maximum (zone II). At the end efficiencies drop rapidly (zone III).

The increase of efficiency in zone I is explained by the fact that the chemical energy stored per ion transported increases with increasing Δm (figure 3.2) while total power losses $[W]$ stay relatively constant in zone I (figure 3.3A). In zone II, losses by osmosis and internal resistance start to increase and therefore efficiency levels off. Finally, in zone III, losses caused by the internal resistance of the diluted solution cause a rapid decline in efficiency.

At the moment it is not smart to operate a CGFB in zone III. However, since power density and energy capacity in zone III are highest, it might be promising to decrease the resistance in this zone. Increasing the conductivity of the diluate compartment by introducing conductive spacers as described in Ref. ^{27,28}, could be an example for making this zone accessible to the CGFB, leading improved efficiency and higher power densities.

Because internal resistance is the largest contributor to power losses in all zones, it has a strong effect on charge efficiency. As a consequence, efficiencies should increase if power loss by internal resistance is reduced. This is exactly what happens in figure 3.3C where lower current densities show higher efficiencies.

Power dissipation (figure 3.3B) during the discharge step and discharge efficiency (figure 3.3D) show identical behaviour to the charge step. The charge and discharge step share the same zones.

From figures 3.3C and D it becomes clear that it is not smart to completely discharge a CGFB, since the charge efficiency is very low at low Δm . Also, the power density of discharging is low in this region and so is the energy capacity. From figure 3.2, 3.3C and 3.3D it becomes clear that discharging beyond Δm of 0.5 m (zone I) is not efficient. Also note that operating the battery in zone III is not efficient either. Therefore, in practice a CGFB should be operated in zone II (working domain) to ensure the best performance. The working domain defined in this paper starts above Δm of 0.5 m and ends when the charge efficiency drops below 40%. It is important to note that pumping losses are not included in figure 3.3.

3.4.4 Effect of current density on power dissipation and (dis)charge efficiency

Next to a change of Δm , also current density has an effect on power dissipation and (dis)charge efficiency.

Figure 3.4 shows experimental results of the working domain (see section 4.3) of constant current experiments performed at 40 °C. The bottom dark-blue bars show the amount of chemical power stored (ED) and electric power extracted (RED). During charge mode, increasing current densities lead to more counter ions being transported, which in turn lead to a higher chemical power stored. During discharge mode, increasing discharge current densities also lead to increased counter ions transport, yielding higher electric power output.

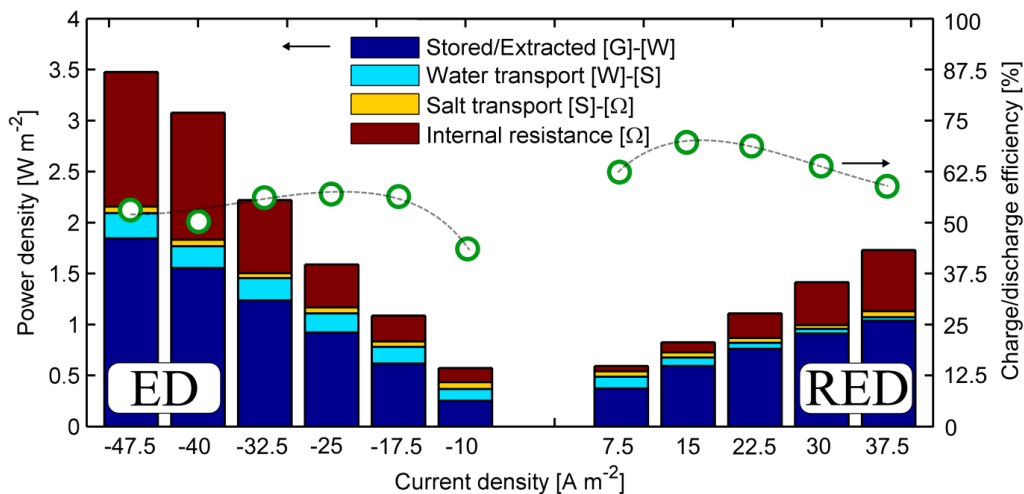


Figure 3.4. Experimental results of power density and (dis)charge efficiency as function of current density measured at 40 °C. The x-axis shows the current density where negative current density is charge (ED) and positive current density is discharge (RED). The left y-axis shows the measured power dissipation contribution for each dissipation source plus the power stored (ED) or extracted (RED). The right y-axis shows the (dis)charge efficiency of the charge/discharge process. All values are averages from all values measured inside the working domain of each experiment (see section 4.3, $\Delta m > 0.5$ and $\eta > 40\%$). Dotted lines are for guiding the eye. The size of the dots is chosen for clarity.

Power dissipation due to water transport shows an interesting behaviour. At low current densities, the battery is slowly charged or discharged. This means that at lower current densities, the solutions have to be recycled through the stack more often. As a result, the average time the solution spent inside the stack increases over a full charge/discharge cycle. An increase in (dis)charge time leads to increased water transport due to osmosis. Therefore, decreasing current densities cause a relative increase in power loss due to water transport.

Different from osmosis, electro-osmosis is coupled to the direction and size of the salt transport. For ED, electro-osmosis causes additional power losses. An increasing current density during charging therefore yields higher power losses by electro-osmosis. For RED, the opposite occurs and electro-osmosis decreases power losses. With increasing current, net water transport is reduced to almost zero at 37.5 A m⁻². The effect of electro-osmosis on power dissipation by water transport as function of current density is very similar to the previous study⁷ and is also predicted by data from Veerman et al.²⁹.

Power lost by unwanted salt transport seems limited over the whole range of current densities and can be considered as the dissipation factor of least importance in a CGFB. The same result was previously reported in Ref. ^{6,7}. The low co-ion transport can be explained by the high charge selectivity of the membranes in the concentration range used. With increasing current densities, the total power dissipation by internal resistance increases rapidly (Ohm's law).

In figure 3.4 also the average (dis)charge efficiency of the whole charge (ED) and discharge (RED) step inside the working domain is shown on the right y-axis. Two observations can be made: (i) Although two optima can be observed, the efficiency remains rather constant over the whole range of current densities tested. (ii) Discharge efficiencies are generally higher than charge efficiencies.

The first observation can be explained by the fact that power loss due to internal resistance is traded off by the power loss due to water transport. At low current densities, osmosis is high because of the longer (dis)charge time and internal resistance losses are low. At higher current densities, osmosis is decreased because of a reduced (dis)charge time but internal resistance losses are high. This trade-off effect is only valid at low current densities reported in this study. Since power losses by osmosis are linearly related to (dis)charge time (and thus current density) but power losses by internal resistance are related to the current density squared, at higher currents power dissipation by internal resistance will increase rapidly and (dis)charge efficiencies will decrease rapidly.

The second observation is explained by the fact that electro-osmosis is energetically favourable for the discharge step but energetically unfavourable during the charge step. It is also observed that the internal resistance losses for charging are somewhat higher compared to discharging, which can be explained by concentration polarization at the membrane interface. In addition, co-ion transport (and thus the associated power loss) is typically lower with discharging than with charging because of the difference in the direction of the electric field ⁷.

3.4.5 Effect of temperature on dissipation and (dis)charge efficiency

Earlier studies showed the effect of temperature on either RED or ED considering the internal resistance and mass transport ¹⁵⁻²¹. To study the effect of temperature on power dissipation and (dis)charge efficiency under CGFB operating conditions several experiments at different temperatures have been performed.

Figure 3.5 shows that for identical current densities and for increasing temperature, power losses decrease due to internal resistance (for charging from 1.41 to 0.72 W m⁻² and for discharging from 0.22 to 0.10 W m⁻²). For RED this is also reported by ¹⁵ and for ED by for example ^{16,20}. The decreased internal resistance makes it possible to operate at higher currents and therefore at higher power densities. However, water transport also increases with increasing temperature (for charging from 0.12 to 0.22 W m⁻² and for discharging from 0.01 to 0.08 W m⁻²). Figure 3.5 shows how a decrease in power losses by internal resistance is partly counteracted by increased osmosis. In fact, water transport turns out to be of such importance that it has been given special attention and is discussed in separate section 4.6.

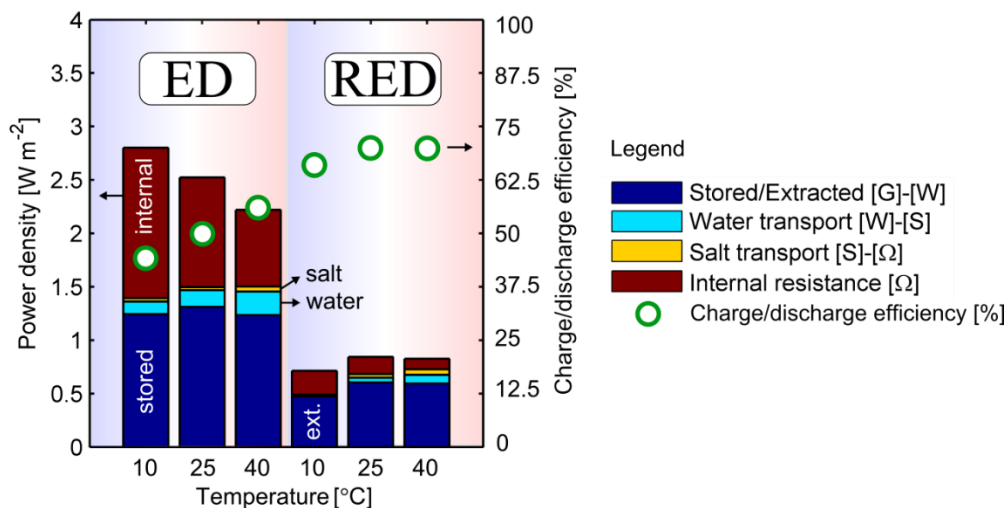


Figure 3.5. Experimental results of power dissipation and (dis)charge efficiency of a CGFB at different temperatures. Charge experiments are done at a current density of -32.5 A m^{-2} (ED) and discharge at 15 A m^{-2} (RED). The x-axis shows the temperatures. The left y-axis shows the measured power dissipation contribution for each dissipation source plus the power stored (ED) or extracted (RED). The right y-axis shows the (dis)charge efficiency of the charge/discharge process. All values are averages from all values measured inside the working domain of each experiment (see section 4.3). The size of the dots is chosen for clarity.

Power losses due to unwanted salt transport ('salt' in figure 3.5) are very small relative to other losses. However, co-ion transport does increase with increasing temperature as can be seen in figure 3.5. This increase in co-ion transport is in line with results from Ref. ^{15,17}. Since the power losses due to co-ion transport are so small compared to other types of losses, it is considered not to be a factor prohibiting the use of higher operating temperatures.

3.4.6 Water transport

Performance of a CGFB is seriously hampered by water transport. Therefore, the effect of water transport over full charge/discharge cycles and the effect of temperature on water transport are discussed in this section in more detail.

Figure 3.6 shows how the concentrations in both reservoirs develop during a full charge (red markers) and discharge (green markers) cycle. In addition, the ideal battery presented in section 4.1 is depicted in figure 3.6 to clearly indicate mismatch between ideal and real situation. Theoretically the battery could be charged until $\sim 1650 \text{ J kg}^{-1}$ (top purple marker figure 3.6), whereas experimentally only $\sim 1050 \text{ J kg}^{-1}$ is achieved. The reason for this is that water is transported from the diluate to the concentrate reservoir during the entire charge step. As a result, the concentrate gets diluted (right top panel) and the maximum Δm that can be reached in practice is lower than the ideal value. Next to the limited Δm , energy density is also limited because of an unfavourable mixing ratio between fresh and salt water. In the previous work, see Ref. ⁷, it is

shown that at high energy density, it is favourable to have a bit more fresh water than salt water. Water transport causes the opposite to happen and therefore energy density becomes limited.

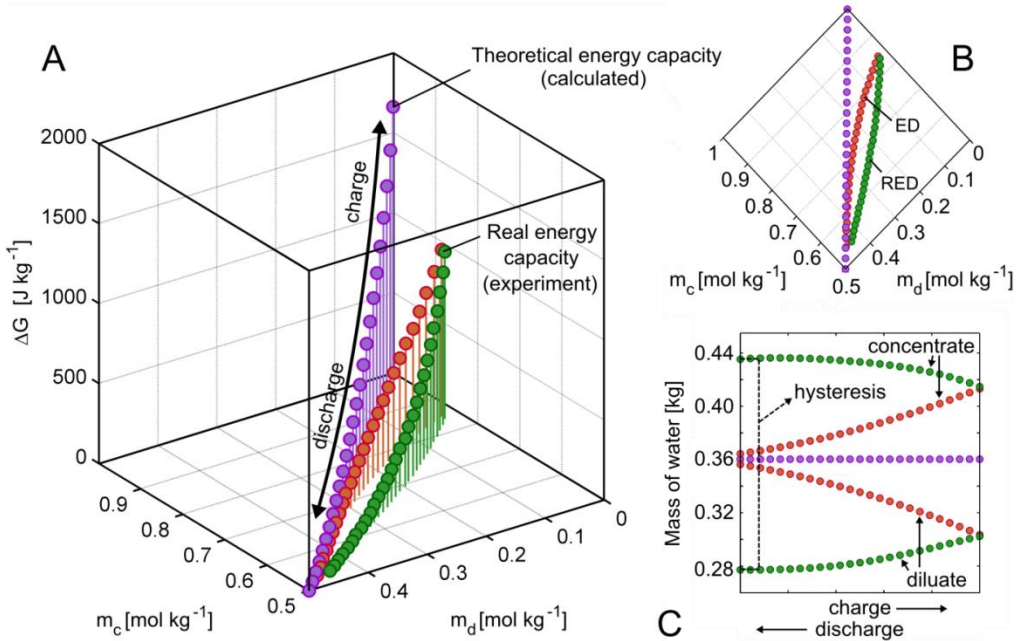


Figure 3.6. Stem plot of the energy density of an ideal battery (purple markers) and the energy density of a real battery during charge (red markers) and discharge (green markers) at 40 °C. (A) On the x and y-axis, the solution molalities of both reservoirs are shown. The z-axis represents the Gibbs energy stored at that instant in J kg^{-1} of water in the system. (B) Top view of panel A is given in panel B, to clearly show the deviation from the ideal battery (purple markers). (C) Panel C shows the mass of water in each reservoir during an ideal charge and discharge cycle (purple markers) and of the measured charge (red markers) and discharge (green markers) cycle. The difference of water mass at the end of each cycle is "hysteresis" of the battery which is responsible for decrease of energy density of the CGFB.

Panel C shows water transport in detail. When charging, the mass of water in the concentrate reservoir (y-axis) increases and the mass of the diluate decreases. The increased water transport towards the end of the charge step is caused by the increased concentration difference. When discharging, water again is transported from diluate to concentrate but since electro-osmosis takes place opposite to osmosis, total water transport is lower. The situation is slightly different during discharge, where Δm decreases and osmosis decreases gradually, but since electro-osmosis stays constant, overall water transport becomes near zero or negative at the end of the discharge step. After a full charge/discharge cycle the water transported has caused hysteresis and the battery needs to be restored. The most straightforward way would be to replace the lost volume of fresh water with water from the concentrate. If the CGFB is completely discharged and both solutions have the same concentration, this would not lead to extra energy dissipation. However, completely discharging a CGFB was shown inefficient. If therefore discharge is

stopped before the battery enters zone I, there still is a difference in concentration. Transferring part of the concentrate to the diluate would lead to undesired mixing yielding some additional energy dissipation (in the particular case of figure 3.6, equalizing the water masses would yield a Gibbs free energy loss of $\sim 131 \text{ J kg}^{-1}$). The hysteresis issue of a CGFB remains to be solved to make the battery more energy efficient.

Figure 3.5 also shows that water transport is affected by temperature. To see how osmosis and electro-osmosis are separately affected by temperature, equation 3.5 and the regression procedure used in Ref. ⁷ are used to quantify this effect on the hydraulic permeability constant L_p and the water transport number t_w , see Table 3.1.

Table 3.1: Estimated parameters L_p and t_w by regression analysis of experimental data. The data includes both ED and RED operating modes at several temperatures.

T (°C)	parameter	unit	value	R ²
10	L_p	$\text{kg m}^{-2} \text{s}^{-1} \text{ kg J}^{-1}$	5.5e-09	0.998
	t_w	$\text{mol H}_2\text{O mol}^{-1} \text{ salt}$	8.6	
25	L_p		8.9e-09	1
	t_w		8.2	
40	L_p		1.4e-08	1
	t_w		8.0	

Table 3.1 shows that the experimental data can be fitted very well ($R^2 \geq 0.998$) with eq. 3.5. This indicates that eq. 3.5 is very well able to quantitatively describe water transport over complete charge/discharge cycles at several temperatures. In addition, the hydraulic permeability constant increases with temperature. This was expected since figure 3.5 already showed that power losses caused by water transport increased with increasing temperature. Surprisingly, the water transport number stays nearly constant over the whole temperature range indicating that electro-osmosis is hardly affected by temperature. To improve battery performance regarding water transport, membranes with lower hydraulic permeability are needed to decrease hysteresis, increase energy capacity and (dis)charge efficiency.

3.5 Conclusions

Full charge and discharge cycles of a CGFB have been performed experimentally at 40 °C with current densities ranging from -47.5 A m^{-2} (ED) to 37.5 A m^{-2} (RED). In addition, full charge (-32.5 A m^{-2}) and discharge (15 A m^{-2}) cycles have been performed at 10 °C and 25 °C. Dissipation of energy and (dis)charge efficiency for both changing concentrations ($0\text{-}1 \text{ mol NaCl kg}^{-1} \text{ H}_2\text{O}$) and temperatures is investigated and discussed.

The majority of the energy is stored at the end of the charge step where the difference in molality is greatest and the diluate very fresh. With increasing molality difference, power losses by osmosis and co-ion transport increase. In contrary power losses due to internal resistance are

shown to be relatively constant over the whole range of molality differences, except for the highest molality difference due to high resistance of the diluate solution. Considering the (dis)charge efficiency, three zones can be distinguished over a typical charge and discharge cycle. The first zone (0-0.5 Δm) is characterized by low (dis)charge efficiency because of a small amount of energy being stored or extracted in this range, while power losses due to internal resistance are significant. The second zone, (~0.5-0.75 Δm), has the highest (dis)charge efficiency and is considered the most optimal working domain of a real CGFB. In this zone, osmosis and co-ion transport are modest, while chemical power stored or electric power extracted is high. The last zone, (~>0.75 Δm), is characterized by the highest amount of chemical power stored or electric power extracted, but because of significant osmosis, co-ion transport and high internal resistance it is not the most optimal operational zone for the CGFB.

Power loss by co-ion transport is typically limited to a few percent in comparison to other losses. This can be explained by the high selectivity of the membranes in the chosen concentration range. Co-ion transport is shown to increase with increasing temperature but remains very small. Power loss by co-ion transport is therefore considered the least important dissipation factor of a CGFB.

The averaged (dis)charge efficiency of the CGFB in the working domain is shown to be quite stable over all current densities applied. This is explained by the trade-off of power dissipation occurring between water transport and internal resistance. For high current densities power dissipation by internal resistance is high, but since total charge and discharge times are shorter, osmosis losses are lower. For low current densities the opposite is true, with low power losses due to internal resistance but higher power losses due to osmosis. Two optima can be distinguished, for ED the maximum charge efficiency measured is 58% at a current density of 25 A m⁻² and for RED 72% at 15 A m⁻² yielding a round trip efficiency of about 42%. The highest temperature recorded the highest (dis)charge efficiencies. This is explained by the low internal resistance at higher temperatures. However, the increase in (dis)charge efficiency is limited since also water transport is shown to increase with temperature.

Water transport does triple damage to the CGFB; it leads to a lower energy capacity, a lower (dis)charge efficiency and causes hysteresis. Regression analysis on measured water transport of multiple charge/discharge cycles shows that with higher temperatures the hydraulic permeability of the membranes increases and electro-osmosis stays unaffected. Just as in the previous study⁷, even with higher temperatures, power losses due to internal resistance remain the most important dissipation factor in a CGFB and in this regard significant improvement of membranes is needed.

Acknowledgements

This work was performed in the cooperation framework of Wetsus, European Centre of Excellence for Sustainable Water Technology (www.wetsus.nl). Wetsus is co-funded by the Dutch Ministry of Economic Affairs and Ministry of Infrastructure and Environment, the Province of Fryslân and the Northern Netherlands Provinces. The authors like to thank the

participants of the research theme “Blue Energy” for the fruitful discussions and their financial support. In addition, the authors would like to thank Slawomir Porada for the valuable discussions.

3.6 References

- (1) Sternberg, A.; Bardow, A. *Energy Environ. Sci.* **2015**, 8 (2), 389–400.
- (2) Carbajales-Dale, M.; Barnhart, C. J.; Benson, S. M. *Energy Environ. Sci.* **2014**, 7 (5), 1538–1544.
- (3) Dunn, B.; Kamath, H.; Tarascon, J.-M. *Science (80-.)*. **2011**, 334 (6058), 928–935.
- (4) Corcuera, S.; Estornés, J.; Menictas, C. In *Advances in Batteries for Medium and Large-Scale Energy Storage*; Lim, C. M. S.-K. M., Ed.; Woodhead Publishing, 2015; pp 29–53.
- (5) Beaudin, M.; Zareipour, H.; Schellenberglobe, A.; Rosehart, W. *Energy Sustain. Dev.* **2010**, 14 (4), 302–314.
- (6) Kingsbury, R. S.; Chu, K.; Coronell, O. *J. Memb. Sci.* **2015**.
- (7) van Egmond, W. J.; Saakes, M.; Porada, S.; Meuwissen, T.; Buisman, C. J. N.; Hamelers, H. V. M. *J. Power Sources* **2016**, 325, 129–139.
- (8) Strathmann, H. *Desalination* **2010**, 264 (3), 268–288.
- (9) Xu, T.; Huang, C. *AIChE J.* **2008**, 54 (12), 3147–3159.
- (10) Galama, A. H.; Saakes, M.; Bruning, H.; Rijnaarts, H. H. M.; Post, J. W. *Desalination* **2014**, 342, 61–69.
- (11) Galama, A. H.; Daubaras, G.; Burheim, O. S.; Rijnaarts, H. H. M.; Post, J. W. *Electrochim. Acta* **2014**, 136, 257–265.
- (12) Vermaas, D. A.; Saakes, M.; Nijmeijer, K. *Environ. Sci. Technol.* **2011**, 45 (16), 7089–7095.
- (13) Yip, N. Y.; Vermaas, D. A.; Nijmeijer, K.; Elimelech, M. *Environ. Sci. Technol.* **2014**, 48 (9), 4925–4936.
- (14) Veerman, J.; Saakes, M.; Metz, S. J.; Harmsen, G. J. *J. Appl. Electrochem.* **2010**, 40 (8), 1461–1474.
- (15) Daniilidis, A.; Vermaas, D. A.; Herber, R.; Nijmeijer, K. *Renew. Energy* **2014**, 64 (0), 123–131.
- (16) Bejerano, T.; Forgacs, C.; Rabinowitz, J. *Desalination* **1967**, 3 (2), 129–134.
- (17) Mir, F. Q.; Shukla, A. *Desalination* **2015**, 372, 1–6.
- (18) Smagin, V. N.; Zhurov, N. N.; Yaroshevsky, D. A.; Yevdokimov, O. Y. *Desalination* **1983**, 46 (1–3), 253–262.

- (19) McRae, W. A.; Glass, W.; Leitz, F. B.; Clarke, J. T.; Alexander, S. S. *Desalination* **1968**, 4 (2), 236–247.
- (20) Forgacs, C.; Koslowsky, L.; Rabinowitz, J. *Desalination* **1968**, 5 (3), 349–358.
- (21) Leitz, F. B.; Accomazzo, M. A.; McRae, W. A. *Desalination* **1974**, 14 (1), 33–41.
- (22) Pitzer, K. S.; Mayorga, G. *J. Phys. Chem.* **1973**, 77 (19), 2300–2308.
- (23) Silvester, L. F.; Pitzer, K. S. *J Phys Chem* **1977**, 81, 1822–1828.
- (24) Tedesco, M.; Cipollina, A.; Tamburini, A.; Bogle, I. D. L.; Micale, G. *Chem. Eng. Res. Des.* **2015**, 93 (0), 441–456.
- (25) Veerman, J.; Saakes, M.; Metz, S. J.; Harmsen, G. J. *Chem. Eng. J.* **2011**, 166 (1), 256–268.
- (26) Veerman, J.; Saakes, M.; Metz, S. J.; Harmsen, G. J. *J. Memb. Sci.* **2009**, 327 (1), 136–144.
- (27) Shahi, V. K.; Thamby, S. K.; Rangarajan, R. *Desalination* **2001**, 133 (3), 245–258.
- (28) Długołęcki, P.; Dąbrowska, J.; Nijmeijer, K.; Wessling, M. *J. Memb. Sci.* **2010**, 347 (1), 101–107.
- (29) Veerman, J.; De Jong, R. M.; Saakes, M.; Metz, S. J.; Harmsen, G. J. *J. Memb. Sci.* **2009**, 343 (1), 7–15.

Supplementary information chapter 3

The experiments are highly reproducible. To show accurateness, results of a duplo of one ED experiment at -32.5 A m^{-2} at 40°C is shown together with the original experiment under the same conditions. For the duplo a completely new stack is built.

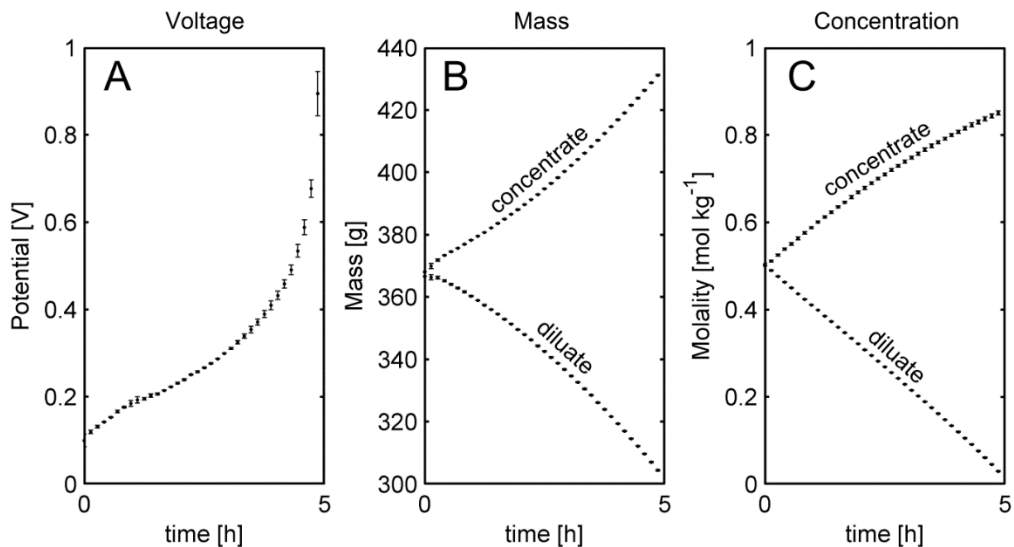


Figure SI-3.1. Min-max error bar plot of raw data of two ED experiments at -32.5 A m^{-2} at 40°C . All data points are average measurement values and the error bars show the minimum and maximum difference from the average. (A) Voltage measurements. (B) Mass measurements of the concentrate (top) and diluate (bottom). (C) Concentration measurements of the concentrate (top) and diluate (bottom).

Figure SI-3.1 shows that for all results (A-C) it is clear that the reproducibility is very high and that the deviation of the duplo from the original experiment is very small. For large part of the curves it is difficult to distinguish the error bars from the mean data points. Therefore, with regular interval data points are removed to make individual data points and error bars better visible.

Chapter 4

Tailoring ion exchange membranes to enable low osmotic water transport and energy efficient electrodialysis

This chapter is published as

Porada, S.; van Egmond, W.J.; Post, J.W.; Saakes, M.; Hamelers H.V.M. “Tailoring ion exchange membranes to enable low osmotic water transport and energy efficient electrodialysis”. *J. Membrane Science* **2018**, 552, 22-30.

Abstract

Ion exchange membranes have been applied for water desalination since the 1950s in a process called electrodialysis, ED. Parallel to the transport of ions across ion exchange membranes, water molecules are transported from diluate to concentrate compartments reducing ED efficiency. In this study tailor made meshed membranes were prepared by embedding polymeric meshes with significantly reduced open area into an ion conductive polymer. These membranes were characterized to assess their transport properties. It is shown that by changing mesh open area, material and surface properties it is possible to significantly reduce osmotic water transport. Polyamide mesh embedded in a cation exchange polymer showed an eightfold decrease of the water mass transport coefficient. Unexpectedly, osmotic water transport was not affected when the same mesh material was embedded in an anion exchange polymer. A decrease of the osmotic water transport for meshed anion exchange membranes was achieved by using a polyethylene terephthalate mesh. Despite the associated electrical resistance increase, application of meshed membranes increased diluate yield and allowed for energy efficient operation in case ED is confined to a low current density regime.

4.1 Introduction

Electrodialysis, ED, is a well-established membrane desalination technology, primarily applied for the treatment of brackish water¹⁻⁷. Many system designs and material modifications have been introduced in order to apply this process in various industries including the chemical, food, pharmaceutical, semiconductor and wastewater industry^{1,8-11}. Moreover, the concept of ion transport across selective barriers can also be used for energy generation in processes like reverse electrodialysis¹²⁻¹⁴ and capmix¹⁵⁻¹⁷ and for energy storage applications¹⁸⁻²⁰. The key components of these processes are ion exchange membranes, IEMs. A typical IEM consists of a polymeric matrix to which charged groups are fixed^{21,22}. There are two types of ion exchange polymers. One with negatively charged groups, such as $-\text{SO}_3^-$, $-\text{COO}^-$ and $-\text{PO}_3^{2-}$, to exclude anions from the matrix and one with positively charged groups, such as $-\text{NH}_3^+$, $-\text{NRH}_2^+$ and NR_3^+ , to exclude cations from the matrix²³. The first type is called cation exchange membrane (since it blocks anions) and the second type is called anion exchange membrane (since it blocks cations).

Figure 4.1 A provides an overview of a basic ED process. Cation- and anion exchange membranes are alternately stacked. The spaces between the membranes are called compartments and are filled with either porous inert spacers or with ion conductive material to allow solutions to flow along the membranes²⁴. On both ends of the membrane assembly two electrodes are submerged in a separate electrolyte ('rinse') solution. In figure 4.1 A, salt water enters at the bottom and flows towards the exit at the top. An electric potential is applied at the electrodes. As a result of the electric field, ions will start to move along the field. Due to the charge selectivity of the membranes, part of the ions is blocked. Consequently, half of the compartments lose ions and becomes fresh ('diluate') and half of the compartment gains ions and becomes concentrated ('concentrate'). In parallel to ion transport across IEM caused by external electric field, there is

also water being transported from diluate (high water activity close to 1) to concentrate compartments (low water activity), see figure 4.1 B. Besides transport of water molecules present in hydration shells of migrated ions (electro-osmosis), water transport can be attributed to osmosis resulting from the chemical potential gradient, and water permeation resulting from a hydrostatic pressure gradient²⁵. Especially osmosis may contribute to a lower diluate yield and higher energy loss due to decreased electrical current utilization for the actual desalination process^{6,19,26,27}. Implications of the osmotic water transport are that ED is ideally operated with a limited concentration gradient over the IEMs (i.e. limiting its application), as well as at high current density and hence low energy efficiency. Osmotic transport may be decreased by developing IEMs with low water permeability. Such membranes can be used, for example, for treating the reverse osmosis retentate to produce highly concentrated brines. Another possible application is a separation process requiring a pure permeate.

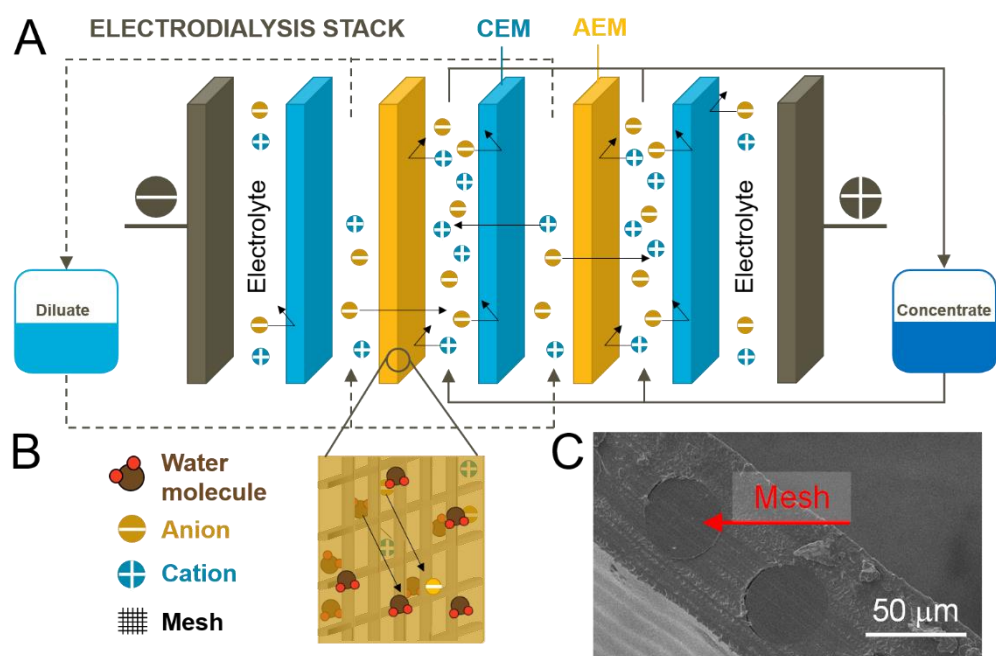


Figure 4.1. (A) Schematic overview of the electrodialysis process. (B) A schematic drawing showing polymeric mesh embedded with (AEM) and depicted water transport from diluate to concentrate side. (C) Scanning electron microscope image of an AEM used in this study.

This study aims to reduce water transport in ED by incorporating a polymeric mesh into an IEM. Figure 4.1 C shows a scanning electron microscope picture of an AEM used in this study. The mesh is completely embedded within the ion exchange polymer, and a continuous dense film of approximately 10 μm thick is covering the polymeric mesh on both sides. We showed that it is possible to increase diluate production yield in a batch mode ED process. This is achieved by a reduction of water osmotic transport due to the presence of a low open area mesh within the IEM structure. We also showed that the application of meshed membranes increases energy efficiency

of ED systems in a low current density regime and at high concentration gradient across IEMs (i.e. at a high gradient of water activity). Normally, the low current density at high concentration gradient across IEMs operational range is not available in ED processes due to low energy efficiency in this region and high costs (for more details of energy efficiency analysis see sections 2.4 and 3.4) ^{6,19}. Finally, we demonstrated that different polymer mesh materials, surface properties and open areas of the mesh affect water transport across charged membranes.

4.2 Experimental

4.2.1 Meshed ion exchange membrane synthesis

The ion exchange membranes were prepared using either anionic (FAS solution, 24 wt. % of polymer dissolved in N-Methyl-2-Pyrrolidone (NMP); Fumatech, Bietigheim-Bissingen, Germany) or cationic ionomer solution (FKS solution, 16 wt. % of polymer dissolved in NMP; Fumatech, Bietigheim-Bissingen, Germany). The membranes without polymeric mesh were prepared by casting 700 μm layer of ionomer solution on top of a glass plate and pre-drying at room temperature under atmospheric conditions to enable slow solvent evaporation process. The pre-dried membranes were carefully removed from the glass plate and were dried at 110 $^{\circ}\text{C}$ in a vacuum oven for two days to remove residual NMP solvent. Meshed membranes were prepared as described above, except ionomer solution was casted directly on top of polymeric meshes using a doctor blade. The casting blade was set to 300 μm to keep the thickness of the dried meshed membranes similar to the homogeneous membranes. Polymeric meshes made of polyamide (Nitex 03-PA 6.6, Sefar, Switzerland) and polyester (Nitex 07-PET, Sefar, Switzerland) were used as non-conductive meshes.

Table 4.1. Overview of polymeric mesh parameters. Specific gravity of the Nitex 03-PA 6.6 is 1.14 g cm^{-3} and Nitex 07-PET is 1.38 g cm^{-3} .

Membranes	Open area mesh (%)	Mesh thickness (μm)	Yarn diameter warp (μm)/ Yarn diameter weft (μm)	Mesh count warp (n/cm)/ Mesh count weft (n/cm)	Mesh opening (μm)/ Weight (g m^{-2})	Mesh area to volume ratio (1/cm)
Nitex 03-PA 6.6	2%	60	45/31	419/689	7/50	1050
Nitex 03-PA 6.6	10%	60	35/35	513/513	15/40	1140
Nitex 03-PA 6.6	18%	60	40/40	361/361	30/35	1000
Nitex 07-PET	2%	55	47/47	406/457	10/60	850

We used three, 60 μm thick, polymeric meshes having different open areas of 18, 10 and 2%, see table 4.1. Surface hydrolysis of polyester mesh was carried out using 2 M aqueous solutions of sodium hydroxide at room temperature for 2 hours. After the treatment, the polyester mesh was washed with pure water and dried in vacuum oven at 25 $^{\circ}\text{C}$ overnight. All prepared membranes had a thickness ranging from 90 to 120 μm when wetted; see table 4.1 for more details.

4.2.2 Measurement of electrical resistance

Current-voltage measurements were performed in a six compartment cell to determine the areal ohmic membrane resistance²⁸. The measuring setup consisted of five ion exchange membranes; three anion exchange membranes (AMX, Tokuyama Soda Inc., Japan), one cation exchange membrane (CMX, Tokuyama Soda Inc., Japan) and the central membrane which was the membrane under investigation. Before measurements, each membrane was equilibrated in the measuring solution of 0.5 M NaCl for at least 24 hours. The effective area of each membrane was 7.07 cm^2 . All compartments, except for the two electrode compartments were filled with 0.5 M NaCl solution. The electrode compartments were filled with a 0.5 M Na_2SO_4 solution and contained platinum coated titanium electrodes. All solutions were continuously pumped through all compartments and the flow rate was 150 mL min^{-1} . A potentiostat (Iviumstat, Ivium Technologies, The Netherlands) was used in a four-electrode configuration. The sense and reference electrode were connected to Ag/AgCl electrodes and the working and counter electrodes were connected to platinized Ti electrodes. The Ag/AgCl reference electrodes (QM711X, QIS, The Netherlands) were used to measure voltage drop across a membrane under investigation. These electrodes were placed inside a small reservoir containing 3 M KCl solution and via Haber-Luggin capillaries placed close to the membrane surface. The combined resistance of the membrane and solutions was measured by chronopotentiometry^{29–31}. In order to get only the membrane ohmic resistance, the combined resistance was corrected for the solution resistance. This resistance was measured in a separate experiment (blank correction).

4.2.3 Experimental setup

The electrode membrane assembly or ‘stack’ used in this work is similar to the one used by Veerman et al.³². All membranes were separated by a combination of silicone gaskets and spacers (thickness of 210 μm and an open area of approximately 50 %, SEFAR, Switzerland). The electrodes (MAGNETO Special Anodes B.V. the Netherlands) are made of titanium mesh with Ru/Ir coating and effective areas of 100 cm^2 . All solutions (rinse, fresh, salt solution) were kept in separate containers. Temperature of all solutions was kept constant by three thermostatic baths at 25 degrees Celsius. The rinse solution comprised of 0.5 M Na_2SO_4 (VWR, the Netherlands) and was recycled through the anode and cathode compartment. Two reference electrodes (QM711X, QIS, The Netherlands) were placed near the centre of the membrane surface and were connected to a potentiostat (Iviumstat, Ivium Technologies, The Netherlands) to measure the voltage across the membrane. The potentiostat was also used to control the current in all experiments. NaCl salt (99.5% pure, ESCO, The Netherlands) was used to prepare all

solutions. For the preparation of all solutions, demi-water was used. All solutions had their own calibrated peristaltic pump (Masterflex L/S, USA). Conductivity sensors were used to measure salt concentrations (VERSA STAR, Thermo Fisher Scientific, USA). Both the salt solution reservoir and fresh solution reservoir were placed on a balance which logged the weight of the bottles over time.

All electrodialysis experiments started with 370 g of 0.5 M NaCl in the salt and fresh water reservoir and were performed in a batch operational mode at a constant current. During ED experiments, both salt and water (by osmosis and electro-osmosis) is transported from the fresh solution reservoir to the salt solution reservoir. Conductivity of the salt and fresh solutions and the weight of both reservoirs were measured over time during each experiment. Based on these measurements the salt and water flux are calculated. For a more detailed explanation of this experimental procedure please refer to Ref. ³³. The diffusion experiments were performed in an identical way as described above, except in this case electrical current was not applied. The initial solution weight was 250 g of 0.8 M and 5 mM NaCl, and only one membrane separated the compartments.

4.2.4 Energy efficiency calculations

Energy efficiency of the electrodialysis process is an important figure of merit to compare the performance of meshed membranes with homogeneous membranes.

Consider two solutions with equal concentrations being pumped into an ED stack. If salt is transferred from one solution to the other, the concentrations of both solutions change. The solutions will start to develop a concentration difference. Two solutions with different concentrations contain chemical energy referred to as Gibbs free energy of mixing. We refer to the rate at which the Gibbs free energy of mixing is added to the two solutions as Gibbs power, P_G (W m^{-2}) expressed as power per m^2 of membrane area. In order to drive this process, electric power, $P_{electric}$ (W m^{-2}), is spent to drive salt against the concentration gradient. Electric power is also expressed as power per m^2 of membrane area. The ratio between Gibbs power and electric power spent is the energy efficiency of the electrodialysis process at that time ³³

$$\eta_{ED} = \frac{P_G}{P_{electric}} \quad (\text{eq. 4.1})$$

To calculate the Gibbs power, we need to consider the chemical species inside each solution. Each solution contains salt and water and therefore has a chemical potential for both salt (μ_s) and water (μ_w). Since there is a concentration difference between both solutions, the chemical potentials for both water and salt are different in each solution. The difference between each chemical potential is referred to as the chemical potential difference of the salt ($\Delta\mu_s$, J mol^{-1}) and the chemical potential difference of the water ($\Delta\mu_w$, J kg^{-1}). To transport a chemical species against its chemical potential, difference energy needs to be spent. Salt transport is expressed as

J_s (mol salt $s^{-1} m^{-2}$). Water transport is expressed as J_w (kg water $s^{-1} m^{-2}$). Eq. 4.2 shows how Gibbs power is calculated ³³

$$P_G = J_w(-\Delta\mu_w) + J_s(-\Delta\mu_s) \quad (\text{eq. 4.2})$$

Equation 4.2 relates P_G in the electrodialysis process with individual contributions of water transport and salt transport ³³. Substitution of eq. 4.2 in eq. 4.1 gives

$$\eta_{ED} = \frac{J_w(-\Delta\mu_w) + J_s(-\Delta\mu_s)}{P_{electric}} \quad (\text{eq. 4.3})$$

Note that by definition, for two solutions with different concentration, $\Delta\mu_s$ and $\Delta\mu_w$ have an opposite sign. Water transport decreases the numerator and therefore energy efficiency. Increasing the electric power spent, $P_{electric}$, also increases the amount of salt transported J_s , since current and salt transport are related in the electrodialysis process.

4.2.5 Diluate yield and water transfer coefficient

For most electrodialysis processes the amount of diluate which can be produced from a certain amount of starting solution contained in the fresh water container is important. In this work we defined the diluate yield as

$$\eta_{dil} = \frac{M_{dil}}{M_0} \quad (\text{eq. 4.4})$$

where M_0 is the mass of solution at the start of the batch process contained in the fresh water container and M_{dil} the mass of diluate produced at the end of the batch process. In desalination applications, high diluate efficiency implies that from a certain amount of prefiltered seawater more drinking water is produced.

Finally, a water transfer coefficient is defined as

$$\beta_w = \frac{J_{w,mol}}{\Delta c_{salt}} \quad (\text{eq. 4.5})$$

where J_w is the water flux in mol $H_2O m^{-2} s^{-1}$ and Δc_{salt} (M) is the molar concentration difference between concentrate and diluate compartments.

4.3 Results and discussion

4.3.1 Osmosis through meshed ion exchange membranes at zero current condition

The results in figure 4.2 A demonstrate an important property of meshed membranes related to the osmotic water transport at zero electrical current conditions. In all cases at the beginning of each measurement, at one side of the membrane 0.8 M NaCl and on the other side 5 mM NaCl solutions are circulated. As a result of osmotic pressure difference, water diffuses

from the diluate (highest water activity) towards the concentrate compartment (lowest water activity) through the ion exchange membranes. As indicated in figure 4.2 A, cation and anion exchange membranes without any polymeric mesh (open area 100%) have similar osmotic water transfer coefficients, with corresponding values of 6.9 for CEM and 5.3 ($\mu\text{m s}^{-1}$). As highlighted in figure 4.2 A, the osmotic water transfer coefficient of meshed cation exchange membranes strongly decreases as a function of mesh open area. For example, cation exchange polymer combined with polyamide (PA) mesh (2 % open area) shows an eight times lower osmotic water transfer coefficient. This is because the area available for water to diffuse decreases, leading to a lower water flux. Interestingly, with a decrease of the mesh open area, the osmotic water transfer coefficient remained almost constant when anion exchange polymer was used. Clearly, decreasing the open area of the mesh does not affect the water transport through meshed AEM membranes. The PA mesh used in this study is made of two monomers, each containing six carbon atoms and repeating amide linkages. These amid functionalities commonly display an amphoteric character ³⁴⁻³⁷. Bismarck et al. ³⁵ reported improved adhesion between the PA polymer and the acid treated carbon fibres. An analogy in terms of interactions of charged materials with the same polymeric material can be seen between the study by Bismarck et al. and this work. Cation exchange polymer which exhibits negative surface charge, similar to the acid treated carbon fibres, is expected to show better adhesion to the PA surface and thus lower water transport compared to the anion exchange polymer.

To further investigate why water transport across meshed AEMs is different from meshed CEMs, the PA mesh (2% open area) in the AEM was replaced with polyethylene terephthalate mesh, PET, with a similar open area fraction. As shown in figure 4.2 A, the osmotic water transfer coefficient significantly decreased when PET mesh was combined with anion exchange polymer, reaching a value of 2.7 $\mu\text{m s}^{-1}$. This indicates that the material of the mesh influences the water transport behaviour of the meshed membranes. Next, an additional diffusion test was performed using chemically modified PET mesh combined with anion exchange polymer. It is known that fibres based on PET have a limited amount of functional groups ³⁸. In order to improve anion exchange polymer adhesion to the PET surface, ester hydrolysis reaction using 2 M NaOH solution was performed ³⁹. This reaction introduces negative chemical groups such as hydroxyl and carboxyl at the surface of the mesh, and thus can lead to improved polymer adhesion caused by the attractive electrostatic interaction ⁴⁰. With the pre-treated PET mesh, the water transport coefficient reached an even lower value of 1.7 $\mu\text{m s}^{-1}$. These results show that the chemical nature of the polymeric mesh surface have an effect on the osmotic water transfer coefficient of the final membrane. We believe that the anomalous high water flux observed at low values of mesh open area for the AEM combined with PA mesh can be explained by poor mesh polymer-ion exchange resin polymer adhesion or stress encountered during membrane preparation process between the polymeric mesh surface and ion exchange polymer. It is known that the transport properties of e.g. mixed matrix membranes for gas separation processes are strongly dependent on the nanoscale morphology between two different materials ⁴¹. Weak interactions and stresses generated during solvent evaporation can lead to void formation ^{41,42}. These voids are considered

as a new phase, which separates, in our case, polymeric mesh from the ion exchange polymer. It is reasonable to assume that the transport properties in this interface region are different from the bulk ion exchange polymer. For example, this new interface can facilitate water transport from the diluate to the concentrate compartment due to higher water diffusivity in this region compared to the bulk polymer. We believe that the ester hydrolysis reaction of PET mesh using 2 M NaOH has improved mesh polymer-ion exchange polymer adhesion due to the presence of additional active surface groups. This active surface interaction can, for example, lead to formation of a rigidified polymer layer around treated PET mesh or can decrease repulsive interaction between two materials. This rigidified polymer layer has lower polymer chain mobility than the bulk polymer and thus water permeation in this region is expected to be decreased^{42,43}. Figure 4.2 B schematically shows the increased water permeability region at the mesh surface.

Interestingly, salt diffusion across meshed membranes shows different behaviour than water diffusion, see figure 4.2 C. The highest salt flux was observed for membranes with the highest open area. It is also possible to see that the salt flux decreases slowly over time. This is explained by reduced driving force as the concentration difference between the solutions changes over time. With smaller open areas, total salt flux clearly becomes smaller. At 2% open area total salt flux is about a factor of twenty smaller for the cation exchange membranes ($\sim 22 \mu\text{mmol m}^{-2} \text{s}^{-1}$ for CEM, PA, 100% and $\sim 1 \mu\text{mmol m}^{-2} \text{s}^{-1}$ for CEM, PA, 2%) and about a factor ten smaller for the anion exchange membranes ($\sim 10 \mu\text{mmol m}^{-2} \text{s}^{-1}$ for AEM, PA, 100% and $\sim 1 \mu\text{mmol m}^{-2} \text{s}^{-1}$ for AEM, PA, 2%). In contrast to the water osmotic transport across AEM, salt diffusion decreases with decreasing the open area. This result can indicate that the salt diffusion occurs primarily through the ion-conductive material. We have also studied a relation between the water transfer coefficient and the ratio of specific surface area to volume of all studied meshes (values are given in table 4.1). If indeed such relation exists, this would further confirm that water transport increases through increased water permeability regions. Based on values reported in table 4.1 and table 4.2 we did not find a clear relation. This can be caused by the presence of areas within each mesh where individual fibres overlap, thus it is difficult to estimate area to volume ratio for each mesh and their contribution to transport processes.

In summary, results presented in this section indicate that applying a mesh within the membrane can reduce the osmotic water transport due to the reduction of surface area and possibly reduced swelling of the membrane. However, mesh polymer-charged polymer interactions and the membrane preparation process are important factors to consider for the design of an optimized meshed ion exchange membrane with reduced osmotic water transport.

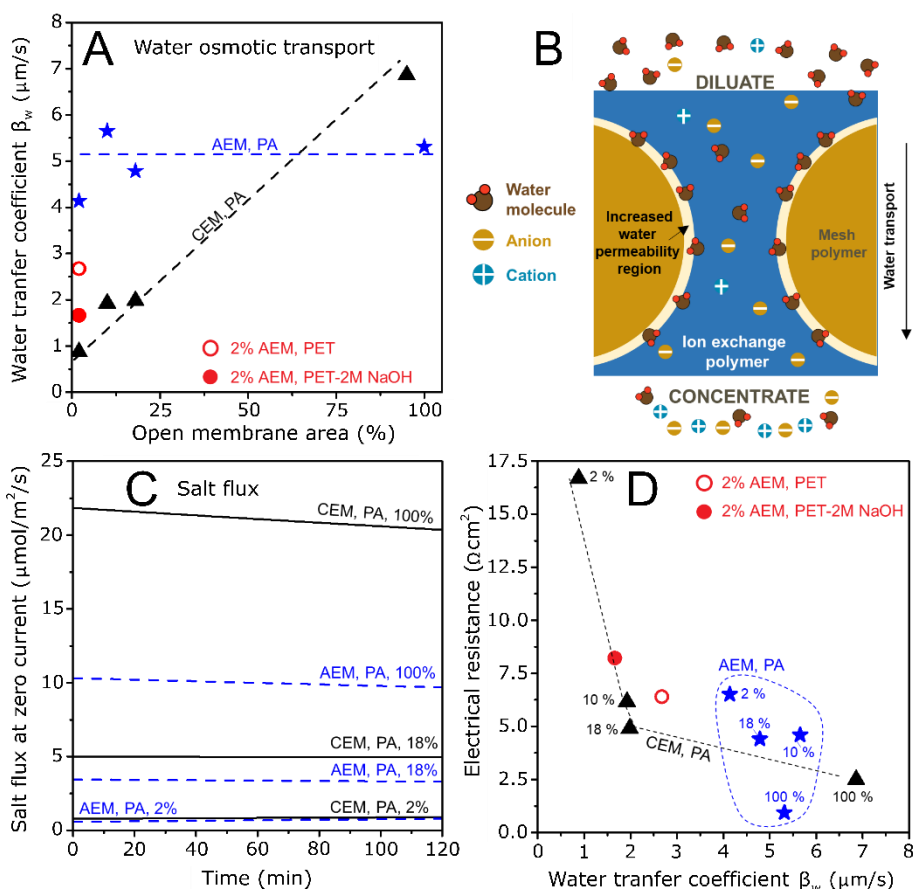


Figure 4.2. (A) Water transfer coefficient for all tested meshed ion exchange membranes at zero electrical current conditions as function of open membrane area, AEM-PA (stars), CEM-PA (triangles), AEM-PET (circles). At the start of each experiment, at one side of the membrane an 0.8 M and on the other side 5 mM NaCl solutions are present. We also provide guidelines for the AEM-PA and CEM-PA data points. (B) Schematic representation of the increased water permeability region, which can be responsible for the almost constant water transfer coefficient observed for anion exchange polymer combined with polyamide mesh. (C) The salt flux measured at zero electrical current conditions as function of open membrane area. (D) Electrical resistance plotted versus water transfer for all tested membranes.

4.3.2 Electrical resistance of meshed membranes

The charge density and structure of the ion exchange membrane determine the ion permselectivity and electrical resistance. Often membranes with lower fixed charge density show lower permselectivity and higher electrical resistance. The latter, among other factors, influences the final energy consumption of the ED process.

As shown in figure 4.5, the electrical resistance of meshed membranes increases with decreasing open area of the mesh. All polymeric meshes used in this study are non-ion conductive and have negligible surface charge density compared to the fixed charge density of ion exchange

polymers. This means that the meshes reduce the area available for ion transport and thus increase electrical resistance. Figure 4.2 D shows that the meshed CEM with 2 % open fraction has the highest electrical resistance of $16.7 \Omega \text{ cm}^2$. This value is approximately six times higher than the electrical resistance of CEM without any mesh. Interestingly, the electrical resistance of the AEM combined with either PET or PA mesh has also increased approximately seven times compared to AEM without any mesh. This indicates that the presence of embedded polymeric mesh has a similar effect on electrical resistance for both anion and cation exchange membranes. Additionally, as shown in figure 4.2 D, a change of the mesh material from PA to PET for anion exchange meshed membrane leads to a decrease of water transfer coefficient, while electrical resistance is not significantly changed. This result can indicate that sodium and chloride ions in both membranes are transported mostly via ion exchange polymer, while water transport occurs through both the ion exchange polymer and so called increased water permeability region.

4.3.3 Water and NaCl salt transport through meshed ion exchange membranes at non-zero current condition

In order to study water and salt mass transport processes across the meshed membranes, multiple electro dialysis experiments at different current densities have been performed. The results of these experiments are shown in figure 4.3 and 4.4. Each electro dialysis experiment starts with two 0.5 M NaCl solutions present in the diluate and concentrate compartment. As current is being applied across the electro dialysis stack and salt is being transported, a concentration difference Δc_{salt} develops between the two solutions. Figure 4.3 A-D shows the actual water flux ($\text{mmol m}^{-2} \text{ s}^{-1}$) as function of the difference in concentration, Δc_{salt} , of both solutions for different current densities (panel A-D, 15-47 A m^{-2}).

Importantly, the osmotic water transport through a membrane is often assumed to be linearly dependent on the salt concentration difference^{6,44-46}. Indeed, figure 4.3 A-D shows that water flux increases linearly with increasing concentration difference. The slope of water flux and concentration difference calculated based on experimental data presented in figure 4.3 A-D, is called water transfer coefficient, β_w , and it is a measure of IEM water permeability. For all current densities plotted in figure 4.3 A-D we observe that the slope increases with mesh open area. This is in agreement with our hypothesis of lower water transport with less open area meshed membranes.

Electro-osmosis is dependent on current density^{6,45-48}. Since at the start of each experiment all concentrations are equal, the water flux measured at these conditions is mainly caused by electro-osmosis. As indicated in figure 4.3 A-D it is clear that with increasing current density, electro-osmotic water transport increases. Since we know the current density and the water flux, it is possible to calculate the water transport number T_w ($\text{mol H}_2\text{O mol salt}^{-1}$)²¹. The water transport number is equal to the amount of moles water molecules transported along with the salt and is based on the measured salt flux. The calculated water transport numbers and other parameters are given in table 4.2.

Table 4.2. Overview of several membrane parameters including thickness of wet membranes, the water transport number, the electrical resistance, the water transfer coefficient and the water content. The standard deviation values are reported in brackets.

Membrane	Open area mesh (%)	Mesh mat.	Thickness of wet membrane, CMX/ AMX or FKS/FAS (μm)	Water transport number T_w (mol H_2O mol $^{-1}$ salt)	Electrical resistance FKS/FAS ($\Omega \text{ cm}^2$)	Water transfer coef. FKS/ FAS ($\mu\text{m/s}$)	Water content FKS/ FAS (%)
Neosepta CMX/ AMX	n.k.	n.k.	170/140	8.0 (± 0.33)	n.k.	n.k.	n.k.
Fumatech FKS/FAS	2%	PA	97/105	11.6 (± 0.58)	16.7/6.5	0.9/4.1	17.8/ 18.1
Fumatech FKS/FAS	2%	PA- PET	97/94	9.0 (± 0.62)	16.7/8.2	0.9/1.6	17.8/ 15.0
Fumatech FKS/FAS	10%	PA	90/95	9.4 (± 0.52)	6.2/4.6	1.9/5.6	18.6/ 21.4
Fumatech FKS/FAS	18%	PA	85/90	10.0 (± 1.0)	4.9/4.4	2.0/4.8	18.2/ 22.3
Fumatech FKS/FAS	100%	n/a	120/115	10.8 (± 0.35)	2.5/0.9	6.9/5.3	35.8/ 30.2

For Neosepta, T_w is 8.0, which value is comparable to the values reported in an earlier study with identical membranes (T_w of 8.2³³). All other measured T_w values range between 9.0 and 11.6 and are also in line with values reported for other homogenous membranes (T_w of 8.0 to 23.4^{45,49}).

As indicated in Ref. ⁶, water molecules are continuously being transported from the diluate to concentrate, causing the concentrate reservoir to dilute during each electrodialysis experiment. As expected, in all panels of figure 4.3 A-D the highest concentration difference has been reached using meshed membranes with the lowest water permeability (2% open area). For electrodialysis processes where high purity of treated water is important, switching to meshed membranes might therefore be a valuable solution. For easy comparison of the performance of the membranes under study to state-of-the art electrodialysis membranes, extra tests have been performed with Neosepta membranes (Tokuyama Soda Inc., Japan). For the highest concentration differences, the 2% open area membranes outperform the Neosepta membranes in terms of water permeability. As shown in figure 4.3 A-D, a combination of CEM-PA and AEM-PET after treatment lowers water transport coefficient by a factor of two compared to commercial Neosepta membranes.

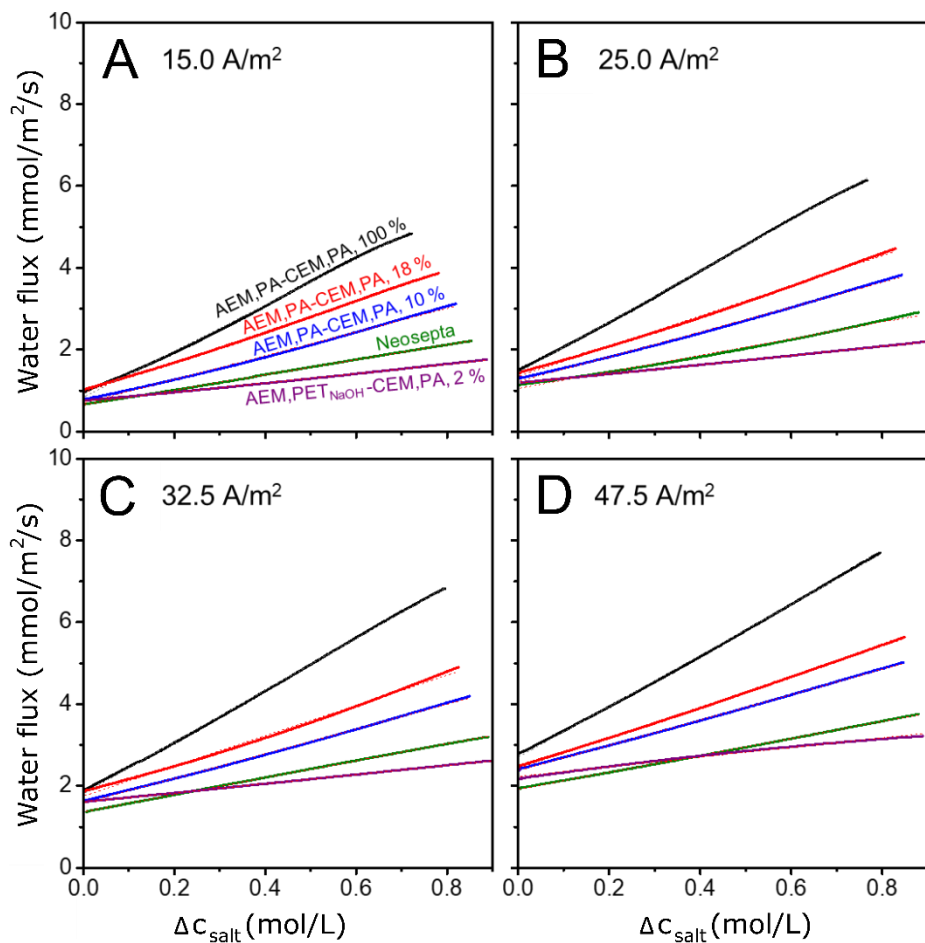


Figure 4.3. Water flux over membranes as function of the concentration difference, Δc_{salt} , for different type of membranes at current densities of (A) 15 A m⁻² (B) 25 A m⁻² (C) 32.5 A m⁻² (D) 47.5 A m⁻².

Figure 4.4 A shows water transport coefficients for different electrodialysis experiments ($I \neq 0$). Since osmosis is not related to the applied current density, one would expect that the average water transport coefficient measured in all experiments coincides with the average water transport coefficients measured for the membrane pairs under zero current conditions ($I=0$). Results presented in figure 4.4 A are in line with our hypothesis. For example, for the 18% open area membranes the water transport coefficient at $I=0$ is 4.8 and 2.0 $\mu\text{m s}^{-1}$ for AEM and CEM membranes respectively (see figure 4.2). The average of these two values equals 3.4 $\mu\text{m s}^{-1}$ and is close to the value plotted in figure 4.4 A, that is 3.7 $\mu\text{m s}^{-1}$.

In addition to the water transport, we have also measured salt transport, see figure 4.4 B. The results shown in figure 4.4 B indicate that higher applied current densities lead to higher salt transport. As the concentration difference increases, the measured salt flux tends to decline

slightly. This can be explained by the increase of unwanted salt transport by diffusion at higher concentration differences. The change in salt flux seems linear with concentration difference 44,45

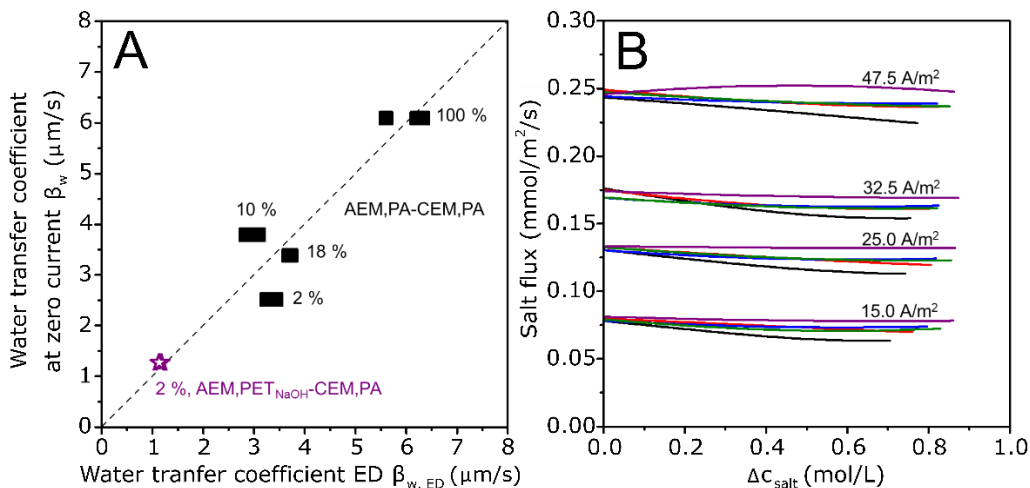


Figure 4.4. (A) Comparison between the water transport coefficient measured during electrodialysis experiments and the water transport coefficient measured at zero current condition for all tested membranes. (B) Measured salt flux of different electrodialysis experiments as function of difference of salt concentration in the solution reservoirs.

4.3.4 Energy efficiency

As mentioned in the introduction section, the purpose of decreasing water transport during electrodialysis process is to improve energy efficiency and to create a system in which a product with higher purity can be produced. In figure 4.2 A and 4.4 A we have shown that by decreasing the mesh open area, lower osmotic water transport can be achieved, but at the same time electrical resistance increases. To evaluate whether the meshed membranes can improve energy efficiency, we analyse experimental data obtained at several current densities and concentration differences. In addition, to allow easy comparison between the self-made membranes and state-of-the-art commercial membranes, results obtained using Neosepta membranes are presented in figure 4.5.

Figure 4.5 A-D shows for different levels of salt concentration difference ($\Delta c_{\text{salt}} = 0.1\text{-}0.7\text{ M}$) and for several current densities the energy efficiency is affected by changing the mesh. The response of the efficiency to the current density differs for the two self-made membranes. In figure 4.5 A-D we see that the meshed membrane efficiency decreases steadily with increasing current density in almost all cases. This indicates that the ohmic energy loss is dominant for the meshed membrane caused by their higher electrical resistance. The response of the homogeneous membrane is different. The homogeneous membrane shows distinct maxima at optimal current density levels. At current densities lower than this optimum, the efficiency drops due to water

transport while at higher current densities the ohmic losses become dominant also for the homogeneous membranes.

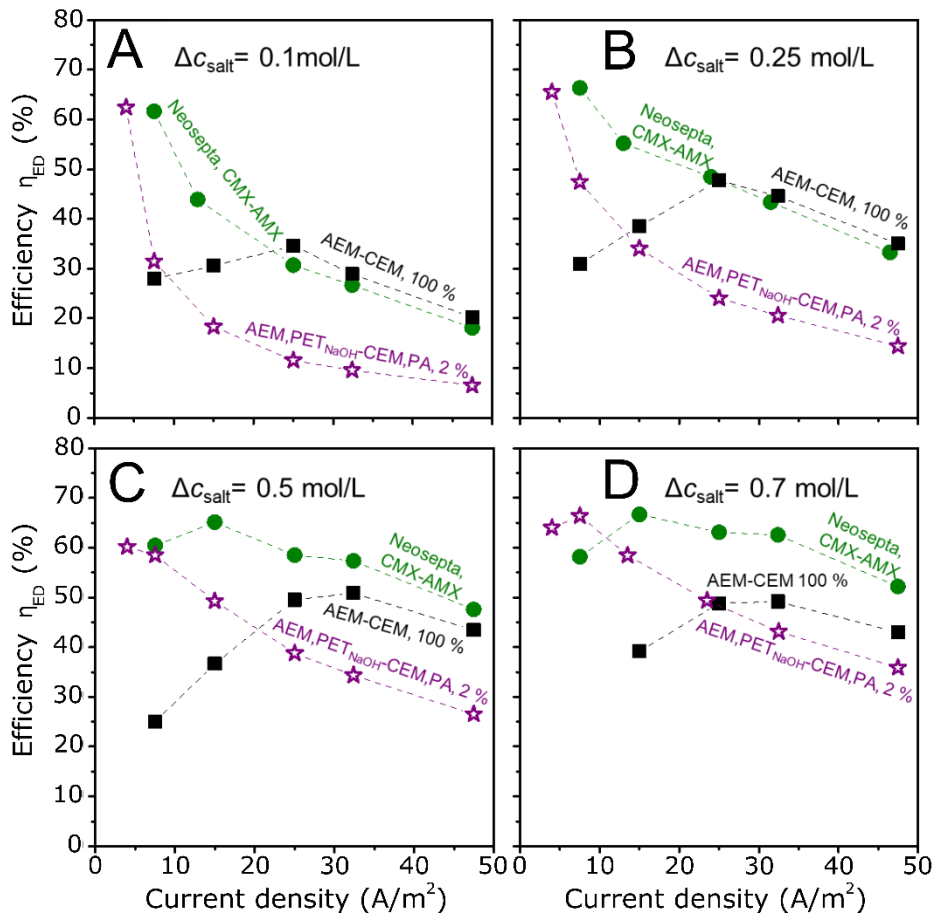


Figure 4.5. (A-D) Energy efficiency of meshed membranes with 2% open area (open purple stars, AEM, PET_{NaOH}-CEM, PA), IEMs without embedded mesh (filled black squares, AEM-CEM, 100% open area) and commercial Neosepta membranes (filled green circles CMX-AMX) as function of applied current density and concentration difference in diluate and concentrate compartments.

At higher current densities, higher than the optimum value, the homogenous membranes outperform the meshed membranes due to its lower electrical resistance (see figure 4.2 D). However, for all different levels of desalination (represented by different concentration differences) and at low current densities, the overall highest efficiency is measured when meshed membranes were used. This also results in the lower overall energy consumption of meshed membranes at current density of 7.5 A m^{-2} , see table 4.3. This is made possible by the strongly decreased water transport property of the meshed membrane. The state of the art commercial Neosepta membranes show high efficiency at multiple current densities and concentration differences.

Table 4.3. Energy consumption in kWh per m³ of diluate produced for meshed membranes with 2% open area (AEM, PET_{NaOH}-CEM, PA), and IEMs without embedded mesh (AEM-CEM, 100% open area) at two current densities.

Membranes	Open area mesh (%)	Mesh material	Current density (A m ⁻²)	Energy consumption (kWh m ⁻³ of diluate produced)
Fumatech FKS/FAS	2%	PA-PET	7.5	1.28
Fumatech FKS/FAS	2%	PA-PET	47.5	2.69
Fumatech FKS/FAS	100%	n/a	7.5	2.06
Fumatech FKS/FAS	100%	n/a	47.5	1.72

4.3.5 Diluate yield

Next to energy efficiency, also diluate yield is a useful parameter for analysing ED performance. Figure 4.6 shows a comparison between the diluate yields of two experiments with different membranes as function of current density. The black squares are experiments with homogenous membranes whereas purple stars are experiments with meshed membranes with 2 % open area. Two important observations can be made; diluate yield increases with current density and diluate yield is higher for meshed membranes. The first observation is explained by the fact that with increasing current densities, total batch desalination process time gets shorter. This means that osmosis has less time to occur and therefore the diluate reservoir loses less water. The second observation is explained by the lower water transfer coefficient of the meshed membrane (also see figure 4.2 A). The lower water transfer coefficient of the meshed membrane leads to decreased diluate loss by osmosis. From figure 4.6 it is apparent that incorporating a mesh inside an ion exchange membrane improves diluate yield for a wide current density range, while providing diluate of almost the same concentration (diluate concentration at current density of 7.5 A m⁻² equals 3.3 mM for the 2 % open AEM, PET_{NaOH}-CEM, PA and 2.0 mM for the 100 % open AEM-CEM).

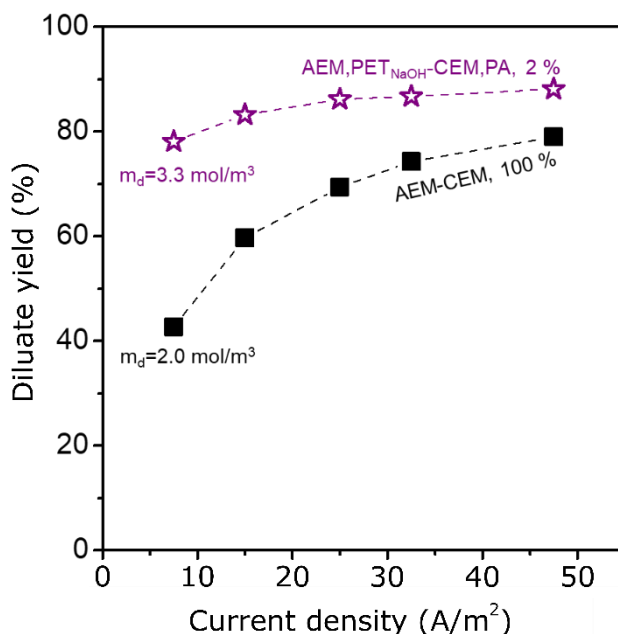


Figure 4.6. Diluate yield (%) of meshed membranes with 2 % open area (open purple stars AEM, PET_{NaOH}-CEM, PA) and IEMs without embedded mesh (filled black squares AEM-CEM, 100%) as function of applied current density (A m⁻²).

4.4 Conclusions

In this study, meshed membranes were prepared by embedding a polymeric mesh with open area percentages varied between 2, 10, 18 and 100 %. These membranes were characterized to assess their water and ion transport properties in an electrodialysis desalination system. We have demonstrated that a significant reduction of the water transfer coefficient can be achieved by embedding polymeric mesh inside a charged polymer. We showed that mesh material type, open area and surface properties are important factors influencing membranes performance in electrodialysis. Although water permeability of the meshed membranes generally decreases with decreasing open area of the mesh, we observed a substantial increase of electric resistance.

In terms of energy efficiency, we showed that meshed membranes with 2 % open area are advantageous over homogeneous membranes at low applied current densities for a wide range of concentration difference across membranes (0.1-0.7 M). We also showed that meshed membranes are advantageous over homogeneous membranes in terms of diluate yield. In addition, the concentrate stream remains purer, considering the fact that transport of electrically neutral molecules in case of meshed membranes will be smaller. Of course, operating an ED system at a lower current density would increase the size of an ED stack leading to higher capital costs. Although this effect is partly diminished by the higher water yield and efficiency, it remains a point of attention.

Operating the ED in a staged fashion could further diminish this disadvantage. This can be achieved by first operating with conventional membranes at higher current density at low concentration difference followed up by a second stage operated at lower current density and higher concentration difference using the meshed membranes.

Acknowledgments

The research is supported by the Dutch Technology Foundation STW, which is part of The Netherlands Organization for Scientific Research (NWO), and which is partly funded by the Ministry of Economic Affairs (VENI grant no 15071).

This work was performed in the cooperation framework of Wetsus, European Centre of Excellence for Sustainable Water Technology (www.wetsus.eu). Wetsus is co-funded by the Dutch Ministry of Economic Affairs and Climate Policy and Ministry of Infrastructure and Water Management, the Province of Fryslân, and the Northern Netherlands Provinces.

4.5 References

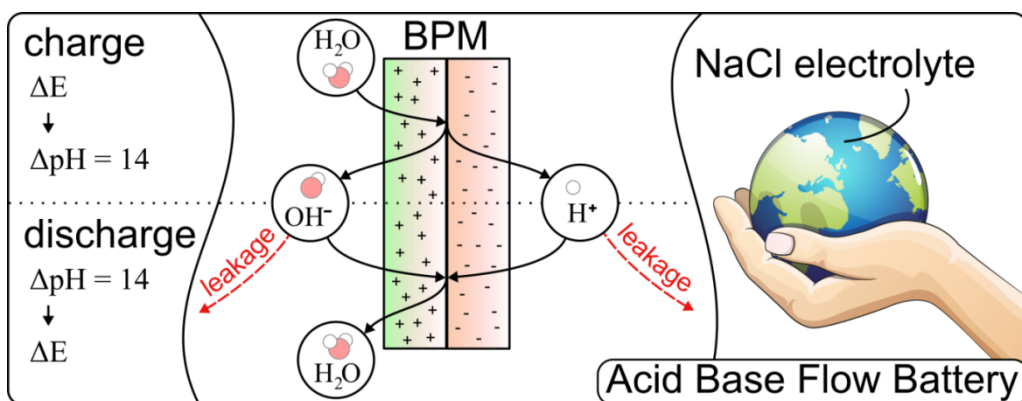
- (1) Strathmann, H. *Desalination* **2010**, 264 (3), 268–288.
- (2) McGovern, R. K.; Zubair, S. M.; Lienhard V, J. H. *Desalination* **2014**, 348, 57–65.
- (3) Kressman, T. R. E. *Nature* **1950**, 165, 568.
- (4) Juda, W.; McRae, W. A. *J. Am. Chem. Soc.* **1950**, 72 (2), 1044.
- (5) Wilson, J. R. *Demineralization by electrodialysis*; Wilson, J. R., Ed.; Butterworths Scientific Publications: Pretoria, 1960.
- (6) Galama, A. H.; Saakes, M.; Bruning, H.; Rijnaarts, H. H. M.; Post, J. W. *Desalination* **2014**, 342, 61–69.
- (7) Galama, A. H.; Daubaras, G.; Burheim, O. S.; Rijnaarts, H.; Post, J. W. *J. Memb. Sci.* **2014**, 452, 219–228.
- (8) Xu, T.; Huang, C. *AIChE J.* **2008**, 54 (12), 3147–3159.
- (9) Garcia-Vasquez, W.; Ghalloussi, R.; Dammak, L.; Larchet, C.; Nikonenko, V.; Grande, D. *J. Memb. Sci.* **2014**, 452, 104–116.
- (10) Basile, A.; Cassano, A.; Rastogi, N. K. *Advances in Membrane Technologies for Water Treatment: Materials, Processes and Applications*; 2015.
- (11) Huang, C.; Xu, T.; Zhang, Y.; Xue, Y.; Chen, G. *J. Memb. Sci.* **2007**, 288 (1–2), 1–12.
- (12) Weinstein, J. N.; Leitz, F. B. *Science (80-.)*. **1976**, 191 (4227), 557–559.
- (13) Vermaas, D. A.; Bajracharya, S.; Sales, B. B.; Saakes, M.; Hamelers, B.; Nijmeijer, K. *Energy Environ. Sci.* **2013**, 6 (2), 643–651.
- (14) Post, J. W.; Hamelers, H. V. M.; Buisman, C. J. N. *Environ. Sci. Technol.* **2008**, 42 (15), 5785–5790.

- (15) Brogioli, D. *Phys. Rev. Lett.* **2009**, *103* (5).
- (16) Brogioli, D.; Zhao, R.; Biesheuvel, P. M. *Energy Environ. Sci.* **2011**, *4* (3), 772–777.
- (17) Sales, B. B.; Burheim, O. S.; Porada, S.; Presser, V.; Buisman, C. J. N.; Hamelers, H. V. M. *Environ. Sci. Technol. Lett.* **2014**, *1* (9), 356–360.
- (18) Kingsbury, R. S.; Chu, K.; Coronell, O. *J. Memb. Sci.* **2015**.
- (19) van Egmond, W. J.; Saakes, M.; Porada, S.; Meuwissen, T.; Buisman, C. J. N.; Hamelers, H. V. M. *J. Power Sources* **2016**, *325*, 129–139.
- (20) Kingsbury, R. S.; Coronell, O. *Environ. Sci. Technol.* **2016**.
- (21) Strathmann, H. *Ion-exchange membrane separation processes*; Elsevier: Amsterdam, 2004; Vol. 9.
- (22) Kariduraganavar, M. Y.; Kittur, A. A.; Kulkarni, S. S. In *Ion Exchange Technology I: Theory and Materials*; 2012; pp 233–276.
- (23) Xu, T. *J. Memb. Sci.* **2005**, *263* (1–2), 1–29.
- (24) Alvarado, L.; Chen, A. *Electrochim. Acta* **2014**, *132*, 583–597.
- (25) Tedesco, M.; Hamelers, H. V. M.; Biesheuvel, P. M. *J. Memb. Sci.* **2016**, *510*, 370–381.
- (26) Indusekhar, V. K.; Krishnaswamy, N. *Desalination* **1985**, *52* (3), 309–316.
- (27) Brydges, T. G.; Lorimer, J. W. *J. Memb. Sci.* **1983**, *13* (3), 291–305.
- (28) Długołęcki, P.; Anet, B.; Metz, S. J.; Nijmeijer, K.; Wessling, M. *J. Memb. Sci.* **2010**, *346* (1), 163–171.
- (29) Vermaas, D. A.; Saakes, M.; Nijmeijer, K. *Electrochim. Acta* **2014**, *117*, 9–17.
- (30) Sistat, P.; Pourcelly, G. *J. Memb. Sci.* **1997**, *123* (1), 121–131.
- (31) Vermaas, D. A.; Saakes, M.; Nijmeijer, K. *Environ. Sci. Technol.* **2011**, *45* (16), 7089–7095.
- (32) Veerman, J.; Saakes, M.; Metz, S. J.; Harmsen, G. J. *J. Memb. Sci.* **2009**, *327* (1), 136–144.
- (33) van Egmond, W. J.; Starke, U. K.; Saakes, M.; Buisman, C. J. N.; Hamelers, H. V. M. *J. Power Sources* **2017**, *340*, 71–79.
- (34) Grancaric, A. M.; Tarbuk, A.; Pusic, T. *Color. Technol.* **2005**, *121* (4), 221–227.
- (35) Bismarck, A.; Richter, D.; Wuertz, C.; Springer, J. *Colloids Surfaces A Physicochem. Eng. Asp.* **1999**, *159* (2–3), 341–350.
- (36) Wang, Y.; Li, X.; Cheng, C.; He, Y.; Pan, J.; Xu, T. *J. Memb. Sci.* **2016**, *498* (Supplement C), 30–38.
- (37) Kirby, B. J.; Hasselbrink, E. F. *Electrophoresis* **2004**, *25* (2), 203–213.

- (38) Prorokova, N.; Chorev, A.; Kuzmin, S.; Vavilova, S.; Prorokov, V. *Chem. Chem. Technol.* **2014**, 8 (3), 293–302.
- (39) Henry, A. C.; Waddell, E. A.; Shreiner, R.; Locascio, L. E. *Electrophoresis* **2002**, 23 (5), 791–798.
- (40) Zhang, J.; Uchida, E.; Suzuki, K.; Uyama, Y.; Ikada, Y. *J. Colloid Interface Sci.* **1996**, 178 (1), 371–373.
- (41) Mahajan, R.; Burns, R.; Schaeffer, M.; Koros, W. J. *J. Appl. Polym. Sci.* **2002**, 86 (4), 881–890.
- (42) Moore, T. T.; Koros, W. J. *J. Mol. Struct.* **2005**, 739 (1–3), 87–98.
- (43) Aroon, M. A.; Ismail, A. F.; Matsuura, T.; Montazer-Rahmati, M. M. *Sep. Purif. Technol.* **2010**, 75 (3), 229–242.
- (44) Tedesco, M.; Cipollina, A.; Tamburini, A.; Bogle, I. D. L.; Micale, G. *Chem. Eng. Res. Des.* **2015**, 93 (0), 441–456.
- (45) Veerman, J.; De Jong, R. M.; Saakes, M.; Metz, S. J.; Harmsen, G. J. *J. Memb. Sci.* **2009**, 343 (1), 7–15.
- (46) Galama, A. H.; Vermaas, D. A.; Veerman, J.; Saakes, M.; Rijnaarts, H. H. M.; Post, J. W.; Nijmeijer, K. *J. Memb. Sci.* **2014**, 467 (0), 279–291.
- (47) Lakshminarayanaiah, N. *Chem. Rev.* **1965**, 65 (5), 491–565.
- (48) Jiang, C.; Wang, Q.; Li, Y.; Wang, Y.; Xu, T. *Desalination* **2015**, 365, 204–212.
- (49) Zlotorowicz, A.; Strand, R. V.; Burheim, O. S.; Wilhelmsen, Ø.; Kjelstrup, S. *J. Memb. Sci.* **2017**, 523 (Supplement C), 402–408.

Chapter 5

Performance of an environmentally benign Acid Base Flow Battery at high energy density



This chapter is published as

van Egmond, W.J.; Saakes, M.; Noor, I.; Porada, S.; Buisman, C.J.N.; Hamelers, H.V.M. "Performance of an environmentally benign acid base flow battery at high energy density". *Int. J. Energy Res.* **2018**, 42, 1524-1535.

Abstract

An increasing fraction of energy is generated by intermittent sources such as wind and sun. A straightforward solution to keep the electricity grid reliable is the connection of large scale electricity storage to this grid. Current battery storage technologies, while providing promising energy and power densities suffer from a large environmental footprint, safety issues and technological challenges. In this paper, the Acid Base Flow Battery (AB-FB) is re-established as an environmental friendly means of storing electricity using electrolyte consisting of NaCl salt. To achieve a high specific energy, we have performed charge and discharge cycles over the entire pH range (0-14) at several current densities. We demonstrate stable performance at high energy density (2.9 Wh L^{-1}). Main energy dissipation occurs by unwanted proton and hydroxyl ion transport and leads to low coulombic efficiencies (13-27%).

5.1 Background

Reliable and sustainable power supply requires large scale electricity storage, as most renewable energy sources are intermittent in their nature ¹⁻⁴. At the same time, large scale electricity storage based on current battery technology raises environmental concerns as their production needs scarce resources that have a high energy demand both for extraction and recycling ⁵⁻⁸. On account of these disadvantages, development of a more sustainable battery is required. Such a battery is based on abundant, easily extractable and recyclable chemicals. A few examples of recently published work on sustainable batteries include an iron redox flow battery ⁹, an iron-air battery ¹⁰, a metal free flow battery based on 9,10-anthraquinone-2,7-disulphonic acid and Br_2/Br^- ¹¹ and a NaCl concentration gradient flow battery (CGFB) ^{12,13}. Although the CGFB has low environmental impact, energy density and power density are too low to be attractive for practical application. In this work, we show that the energy density and power density of the CGFB can be improved by implementing a bipolar membrane. The studied system is an energy storage system based on a reversible acid-base reaction. In this system called Acid Base Flow Battery (AB-FB), energy is being stored in acid and base solutions created by the bipolar membrane. The charge step of the AB-FB is similar to the well-known bipolar membrane electro dialysis (BPM-ED). BPM-ED converts NaCl solutions into NaOH and HCl solutions by spending electric power to separate protons and hydroxyl ions from water dissociation from the bipolar junction inside a bipolar membrane. Energy is recovered by performing the opposite process, neutralizing the acid and base at the bipolar junction inside the bipolar membrane to form water. The process is therefore also distinctly different from the Acid Base Electrochemical Flow Battery (e.g. ¹⁴ and ¹⁵) which is dependent on electrode reactions involving hydrogen gas and platinum as catalyst. Potentially, the AB-FB has several environmental and safety advantages compared to typical battery or redox flow battery systems. First of all, the AB-FB system does not use any precious, toxic or scarce materials which are, in addition to being expensive, sometimes also difficult or energy intensive to recycle ¹⁶⁻¹⁸. Secondly, the solution used in an AB-FB is NaCl solution which can be derived from and recycled back to seawater which is cheap and abundantly available. In a real sized AB-FB, up to hundreds of membrane cells in series are sandwiched between two electrodes (fig. 1). Unlike redox flow batteries, the number of electrodes necessary

in an AB-FB is brought back to a total of two. These electrodes do not necessarily require metals, they can be made of an environmental friendly source of carbon ¹⁹. Additionally, an environmental friendly battery consumes little energy to be produced. A useful metric is the energy stored on invested (ESOI), which relates the amount of energy a battery system stores over its entire lifetime to the energy it costs to produce the system ²⁰. Energy storage systems which use mostly natural materials (for example PHS - water or CAES - air) have the highest scores and are considered to be very environmental friendly in terms of energy consumption during production ^{8,20}. Since an AB-FB also uses mostly natural materials the AB-FB has the potential to reach similar high ESOI values. Next to the environmental advantages, the AB-FB largest advantage is safety. Fire or explosion hazard is negligible. Also, it is impossible that air, soil or natural waters are damaged by leaching toxic chemicals.

An AB-FB has a theoretical energy density of 11.1 Wh L⁻¹ when a maximum of 1M of acid and base is used (as is done in this study). This study reports a measured energy density of 2.9 Wh L⁻¹. The difference between theoretical and measured capacity is mainly caused by co-ion transport as will be shown later. Yet, if co-ion transport could be minimized, the theoretical energy density of an AB-FB could be much higher because more concentrated solutions could be used (e.g. ~44 Wh L⁻¹ ²¹ for 4M of acid and base solutions). Please note that the energy density is expressed for the volume of acid and base solutions as these are the energy carrying solutions. The salt solution does also consume space as well as the redox solution, the membrane system, housing, pumps etc., the sizes of which can fluctuate and can be freely chosen to some extent. Practical energy densities will therefore be somewhat lower as these volumes should be included. Typical redox flow batteries such as Vanadium or ZnBr redox flow batteries show energy densities in the range of 16-35 Wh L⁻¹ and 20-65 Wh L⁻¹ ²²⁻²⁴ respectively. Although the measured energy density of an AB-FB so far is a factor smaller compared to RFBs, it is already comparable to pumped hydro systems (PHS, 0.5-2 Wh L⁻¹) and compressed air systems (CAES, 2-6 Wh L⁻¹) ²⁵. This would already make the AB-FB an option to store surplus sun and wind energy on the daily to weekly scale just as PHS and CAES are used. An AB-FB can be placed anywhere and has no geographical constraints like PHS or CAES ²⁶ and is scalable.

Early work on the AB-FB concept was done in the 1970s by Ramp ²⁷ where the author-discussed different cell designs including the design used in this study. In this work however, the author tested another concept using Pd electrodes and phosphoric acid without bipolar membranes. The next published study about the AB-FB concept was published by Emrén et al. in the '80s ²¹. They used the same stack design as used in this study but reported an extremely low energy efficiency of 0.1%. Zholkovskij et al. published experimental work on another AB-FB concept in the '90s ²⁸. Zholkovskij et al. chose to charge the battery only up to 0.03 M acid/base and to leave the acid/base solution stationary inside the membrane assembly. They reported a specific energy up to 0.1 Wh kg⁻¹ (acid and base combined). In the same year, Pretz et al. ²⁹ also published a study where they use the AB-FB concept as a fuel cell. They only discharge and use pure acid and base solutions. They reported maximum discharge efficiencies with 1M acid and base of <1%. A

recent study by Kim et al.³⁰ reports an energy density up to 0.9 Wh L⁻¹ (based on unspecified volumes). Their cell design is similar to the design used in this study except for their electrodes. The cell design is based on a patent³¹ where carbon electrodes are used in combination with a Fe²⁺/Fe³⁺ redox couple to avoid gas evolving redox reactions. Their choice of Fe²⁺/Fe³⁺ redox couple in combination with cation exchange membranes next to the electrode compartments led to iron ion migration from the electrode compartments to the base compartment. Here, the iron precipitated leading to unstable performance. In addition, they reported that the anion exchange layer of their bipolar membrane was damaged by the alkaline solution. Although the principle of the AB-FB is known, no study is known which experimentally operates the AB-FB in a stable way at sufficient energy density (using the whole pH range) with reasonable efficiency.

In this study, we provide experimental validation that it is possible to have stable operation of an AB-FB at high energy density (pH range 0-14). Low round trip efficiency remains an issue for the AB-FB. Therefore, we study round trip efficiency in more detail using a new set of analytical expressions to describe and quantify the energy efficiency of the AB-FB in terms of different energy dissipation sources (ohmic losses, non-ohmic losses and co-ion losses). We show the contribution of each type of energy loss in combination with coulombic efficiency, voltage efficiency and energy efficiency as function of current density. Also, we experimentally determined what the highest allowable discharge current density is before delamination of the bipolar membrane occurs. Finally, we discuss the optimal mode of operation and future directions to improve the round-trip efficiency.

5.2 Theory

To assess performance and power dissipation of an AB-FB a theoretical framework is provided. The framework assumes ideal selective membranes and gives an upper limit for the specific energy. Figure 1 shows how an AB-FB works.

Figure 5.1 A shows the two major components of an AB-FB, the electrode membrane assembly which is the power unit on the left and the electrolyte reservoirs where energy is stored on the right. A typical power unit is very similar to the designs of BPM-ED systems^{32–36}. It consists of two electrodes where up to hundreds of membranes are placed in between. Three different types of membranes are present and stacked in alternate fashion: Cation exchange membranes (c), bipolar membranes (b) and anion exchange membranes (a). Between the membranes a spacer is placed which is permeable to the electrolyte solutions. The space between two membranes is called a compartment. Three compartments and three membranes (one of each type) together is called a cell. Many of these cells are thus placed in series between the electrodes. The electrolyte solutions are pumped through the compartments and recycled back to the reservoirs. The extra reservoir on the right side contains a solution which facilitates a redox reaction on the electrodes. This solution is pumped only to the two electrode compartments where it converts the ionic current from the membranes to an electric current at the electrodes. The redox reaction used in this study is the electrolysis reaction of water (water decomposed into O₂ and protons at the anode and into H₂ and hydroxyl ions at the cathode), but many other redox reactions are possible.

Two examples of electrolyte solutions (that are in contact with the anode and cathode) are NaCl^{37,38} and Na₂SO₄^{33,39}. Just as in BPM-ED systems, the energy consumed by the redox reaction occurring at the electrodes is considered negligible compared to the amount of energy which is stored or extracted from the processes at the membranes.

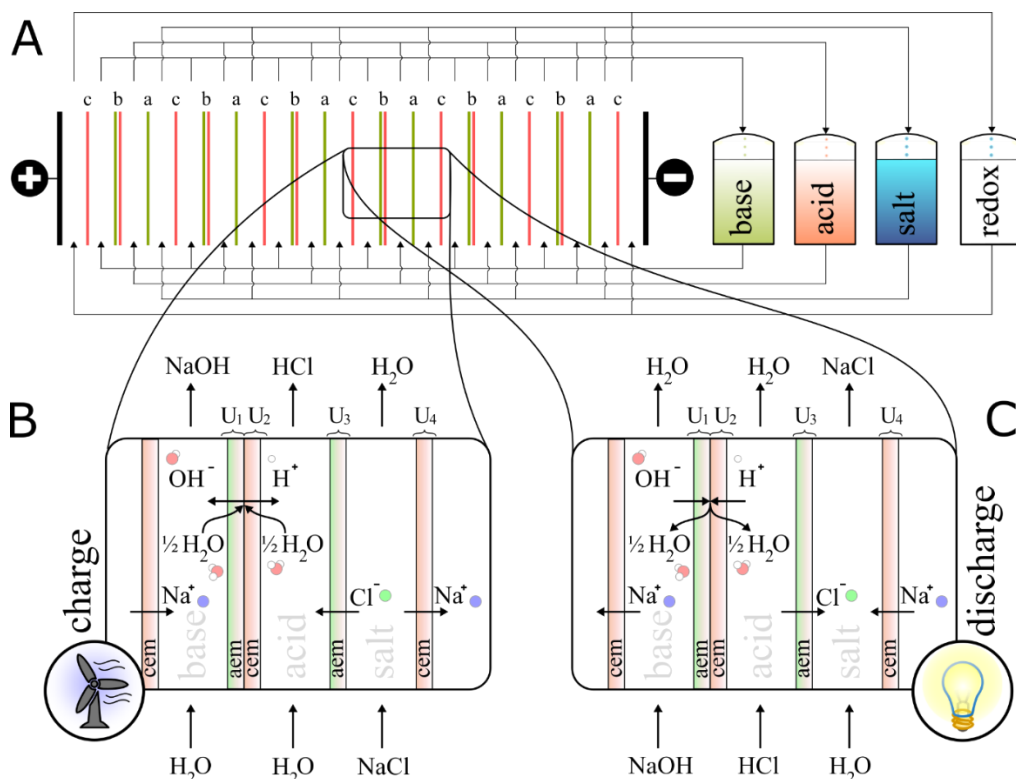
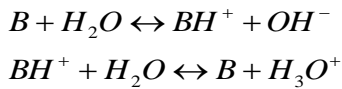


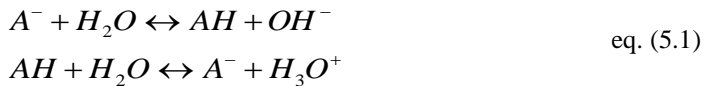
Figure 5.1. A conceptual drawing of an Acid Base Flow Battery (AB-FB). (A) On the right side, the reservoirs with solutions are shown. On the left, the membrane assembly is shown. Between two electrodes many membranes (up to hundreds) are stacked in repetitive manner. (B) Close-up of a single cell (bipolar membrane, consisting of anion exchange material and cation exchange material, anion exchange membrane and cation exchange membrane) with the water dissociation process and mass transport. (C) Close-up of a single cell during discharge with the neutralization of the acid and base and mass transport. Please note that voltage lost at the electrodes by the redox reaction is negligible compared to the voltage generated by many membranes.

To understand how energy is stored in the AB-FB system, figure 5.1 B zooms in on a single cell. The first compartment is connected to the ‘base’ reservoir. The first membrane is a bipolar membrane. A bipolar membrane is made by fusing an anion exchange membrane (aem) and a cation exchange membrane (cem) together, typically with a catalyst in the aem and/or cem^{33,40}. Anion exchange membranes are made of polymers containing fixed positive charges^{32,41}. The positive fixed charges allow anions to enter the membrane but block cations and therefore make the membrane charge selective. Cation exchange membranes are identical except for the sign of the fixed charges and thus they are selective towards cations. The second compartment is

connected to the ‘acid’ reservoir. At the start of the charge process, the flow battery is empty and in all reservoirs only ordinary NaCl solutions are present. Once potential is applied at the electrodes ions in solution and inside the membranes will start to move according to the electric field. Inside the bipolar membrane, initially sodium and chloride ions will move out of the membrane. As soon as these ions are depleted, water dissociation occurs inside the bipolar membrane at the interface of the aem and cem. Protons and hydroxyl ions are created by a dissociation reaction of water while interacting with weakly basic or acidic groups present at the membrane surface area ^{42–44}. Following Simons and Strathmann ^{42–44} the following reactions can occur (eq. 5.1)



and



where B is a neutral base, BH⁺ the catalytic active centre (typically the fixed charged group on the anion exchange membrane), A⁻ the fixed group on the cation exchange membrane and AH a neutral acid ⁴². Different catalysts are added for promoting the water dissociation reaction ⁴⁰. Examples include carboxylic acid ⁴⁴, tertiary amines ⁴⁵ and phosphoric acid ⁴⁶.

In figure 5.1 B we see that base compartment is gaining hydroxyl ions and the acid compartment is gaining protons. To account for electroneutrality in both the ‘acid’ and ‘base’ compartments, the extra ‘salt’ solution compartment is added. This compartment provides sodium ions to the base solution and chloride ions to the acid solution. The extra two membranes are present to prevent the three solutions from mixing. The result of the charging process is that electric energy is spent, the acid reservoir becomes acidic, the base reservoir becomes alkaline and the concentration of salt in the salt reservoir decreases. The final concentration of the salt reservoir in charged state, depends on the choice in size of the reservoir and starting concentration. In this study the concentration of the salt reservoir in the charged state was 0.214M (refer to section 3.2 for starting volume and concentration).

In the discharge process, current direction is reversed (figure 5.1 C). In this case all ions move in opposite direction so that protons and hydroxyl ions recombine again inside the bipolar membrane to form water, thus neutralizing the acid and base solution. The salt compartment gains both sodium and chloride ions again and the salt concentration returns to its original level. To understand how energy is harvested in this process we show the membrane potentials involved. At the interface of the bipolar membrane where both ion exchange materials touch, the concentration of protons and hydroxyl ions is very low (10⁻⁷ M). In a charged battery, the

concentration of hydroxyl ions and protons inside the base and acid solutions is much higher (1 M) and because of Donnan exclusion, a membrane potential is created over each layer of ion exchange material (eq. 5.2, U_1 and U_2). In a charged flow battery, the concentration of salt in the salt reservoir is low. In this study, it is 0.214 M of NaCl. Since the concentrations of chloride (1 M) in the acid reservoir and sodium (1 M) in the base reservoir is higher, also a membrane potential develops over the extra anion exchange membrane (U_3) and cation exchange membrane (U_4). In order to calculate an ideal membrane potential, we use the Nernst equation (eq. 5.2). Next, assuming ideal solutions, the membrane potentials of all membranes are summed to calculate the maximum cell potential (eq. 5.2)

$$\begin{aligned}
 U_1 &= \frac{RT}{zF} \ln \left(\frac{[\text{OH}^-]_{bp}}{[\text{OH}^-]_{base}} \right) \approx \frac{RT}{-F} \ln \left(\frac{10^{-7}}{1} \right) = 0.414 \\
 U_2 &= \frac{RT}{zF} \ln \left(\frac{[\text{H}^+]_{acid}}{[\text{H}^+]_{bp}} \right) \approx \frac{RT}{F} \ln \left(\frac{1}{10^{-7}} \right) = 0.414 \\
 U_3 &= \frac{RT}{zF} \ln \left(\frac{[\text{Cl}^-]_{salt}}{[\text{Cl}^-]_{acid}} \right) \approx \frac{RT}{-F} \ln \left(\frac{0.214}{1.5} \right) = 0.050 \\
 U_4 &= \frac{RT}{zF} \ln \left(\frac{[\text{Na}^+]_{base}}{[\text{Na}^+]_{salt}} \right) \approx \frac{RT}{F} \ln \left(\frac{1.5}{0.214} \right) = 0.050 \\
 \hline
 U_{cell} &= U_1 + U_2 + U_3 + U_4 = 0.928
 \end{aligned} \tag{5.2}$$

where U_1 - U_4 Nernst potentials correspond to each membrane layer depicted in figure 5.1 C and U_{cell} is the total cell potential (V). Since in a AB-FB many cells are stacked in series the voltage over the electrodes can reach up to tens of volts.

An important phenomenon which can occur inside a bipolar membrane is delamination. When the discharge current density is too high, protons and hydroxyl ions recombine that fast that the produced water cannot diffuse out of the membrane fast enough. In this case the two ion exchange layers can delaminate⁴⁰ in a process also known as ‘ballooning’ of the membrane. In a AB-FB, the discharge current densities are therefore limited by delamination. In this study we could safely operate the AB-FB up to 15 A m⁻². Another reason for bipolar membrane delamination is the presence of CO₂. The base solution can absorb CO₂ from the air. When the pH of the solution changes inside the bipolar membrane gaseous CO₂ can form leading to delamination⁴⁰.

As the flow battery is discharged and the concentrations inside the electrolyte reservoirs change, cell potential drops. With the decrease of cell potential, the remaining energy content of the solutions drops as well. For an ideal flow battery the remaining energy content can be calculated as a function of the acid concentration according to eq. 5.3⁴⁷

$$\Delta G = \int_{10^{-7}}^{[H^+]} F U_{cell} d[H^+] \quad \text{eq. (5.3)}$$

where ΔG (J L⁻¹) is the total energy content, $[H^+]$ is the concentration of protons in solution (mol L⁻¹) and F is Faraday's constant (C mol⁻¹).

Figure 5.2 shows how energy density of such ideal flow battery behaves as function of the pH of the acid reservoir. Please note that the base concentration is identical to the acid concentration.

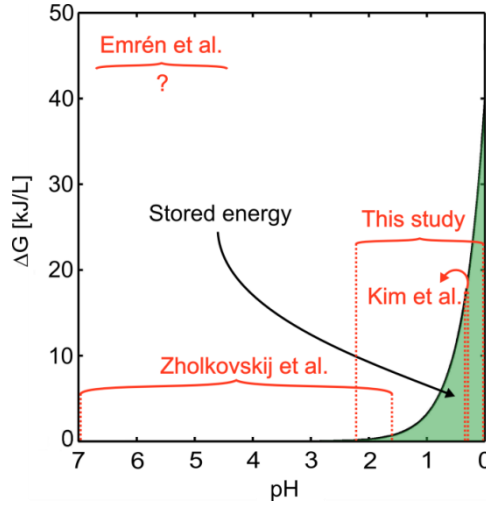


Figure 5.2. The energy content (ΔG in kJ L⁻¹) of an AB-FB as function of pH in the acid compartment. The energy content is expressed for 0.5 L acid and 0.5 L base solution and shows the maximum amount of energy which can be harvested during discharge. The operating range (in pH) for previous studies is shown as red brackets.

The total internal resistance R_i of a flow battery is given by

$$R_i = \overbrace{R_{BP} + R_{AEM} + R_{CEM} + R_{base} + R_{acid} + R_{salt} + R_{electrodes}}^{\Omega} + \overbrace{R_{non-\Omega}}^{non-\Omega} \quad \text{eq. (5.4)}$$

where R_{BP} is the resistance of the bipolar membranes, R_{AEM} and R_{CEM} the resistances of the anion and cation exchange membranes respectively, R_{base} , R_{acid} and R_{salt} the resistances of the solutions compartments and $R_{electrodes}$ the resistance of the rinse solution compartments plus the resistance of the extra cation exchange membrane (see fig. 5.2). Together these resistances constitute the ohmic resistance (denoted as Ω in eq. 5.4) of the flow battery. In practice, many cells will be put in series so that $R_{electrodes}$ becomes negligible. Because of concentration polarization at the membrane interface when current is applied, non-ohmic resistance arises. This is represented in eq. 5.4 by $R_{non-\Omega}$.

Because of losses due to internal resistance, measured cell potential U is given by

$$U = U_{cell} - IR_i \quad \text{eq. (5.5)}$$

where I is current. The round trip efficiency, η_{RTE} , is an important figure of merit for all storage technologies. It is the ratio of energy released at discharge over energy consumed during charge. For constant current experiments, it can also be calculated by multiplying the coulombic efficiency and voltage efficiency^{12,48}.

$$\eta_{RTE} = \frac{\int_0^{t_d} I_d U_d dt}{\int_0^{t_c} I_c U_c dt} = \eta_{CE} \eta_{VE} \quad \text{eq. (5.6)}$$

where subscripts d and c stand for discharge and charge respectively. Total time for charge/discharge is given by t , the applied current by I and the measured potentials during charge and discharge are given by U . The coulombic efficiency η_{CE} is the ratio of total charge transferred during discharge over the total charge transferred during charge. Voltage efficiency is given by η_{VE} and is useful for determining the magnitude of internal losses due to internal resistance.

The total amount of energy lost is calculated by

$$E_{lost} = \int_0^{t_c} I_c U_c dt - \int_0^{t_d} I_d U_d dt \quad \text{eq. (5.7)}$$

and the total amount of energy lost on internal resistance by

$$E_{Ri} = \int_0^{t_c} R_i I_c dt + \int_0^{t_d} R_i I_d dt \quad \text{eq. (5.8)}$$

The difference between the total energy loss and the ohmic loss is the energy loss due to other processes as co-ion transport and water transport. In case of the AB-FB it can be argued that this is mainly due to unwanted transport of protons and hydroxyl ions^{21,27}. This co-ion transport loss is then given by

$$E_{co-ion} = E_{lost} - E_{Ri} \quad \text{eq. (5.9)}$$

5.3 Materials and Method

5.3.1 Experimental set-up

The experimental set-up used in this work consists of a flow battery with membranes and electrodes arranged as depicted in figure 5.1 and we study a single cell. The membrane/electrode assembly is pressed and is hold together by two external acrylic plates. The membranes are separated by 500 μm spacers (SEFAR AG, Switzerland), and sealed with a silicon gasket. Four

bottles containing base, acid, salt and rinse solutions are connected with pumps and solutions are pumped through the appropriate in- and outlets. Following the procedure outlined by Veerman et al.⁴⁹, two Ag/AgCl reference electrodes (QM711X, QIS, the Netherlands) are placed in the rinse solutions close to the shielding cation exchange membrane. Two titanium mesh 1.0 electrodes coated with mixed metal oxide (iridium and ruthenium, Magneto Special Anodes B.V., the Netherlands) and reference electrodes are connected to a galvanostat (model IviumStat.XRi, Ivium Technologies, the Netherlands). Please note that although in this study Ti-mesh electrodes are used with precious metals, in a commercial AB-FB many other (abundant) non-catalytic materials such as carbon or graphite could be used. Although non-catalytic electrode materials (no precious metals involved) would increase the overpotential of the redox reaction, this extra energy loss would be negligible compared to the amount of energy stored and released in the membranes. Another option is to use noble metal free electrode material like carbon or graphite felt in combination with a low-cost reversible redox couple based upon e.g. Fe(II) and Fe(III) with an appropriate ligand. That would result in low energy losses at the electrodes in combination with the use of a low-cost reversible electrochemical redox couple. The anion exchange membrane used (FAB-PK-130, Fumatech GmbH, Germany) is specifically selected for its high proton blocking property. The bipolar membrane is a low resistance Fumasep FBM ($<3 \Omega \text{ cm}^2$). The cation exchange membranes adjacent to the electrode compartments are Nafion N117 membranes (Dupont, USA)) that are resistant against any unwanted Cl_2 that might form at the electrodes during charge or discharge. The effective area of each membrane is 0.01 m^2 . The electrolyte solutions are pumped with a flow rate of 30 ml min^{-1} . Galvanic decoupling between both electrode compartments to avoid short circuit currents⁵⁰ is assured by adding additional bottles and using the droplet method. For safety, N_2 gas is pumped inside the bottles to remove the O_2 and H_2 mixture in the head space of the bottles.

5.3.2 Experimental procedure

First a test was performed to measure the open circuit voltage (OCV) of a fully charged flow battery. Fresh acid, base, salt and rinse solutions were prepared. The acid solution consisted of 1 M HCl (Sigma Aldrich, USA) mixed with 0.5 M NaCl (ESCO, the Netherlands). The base solution consisted of 1 M NaOH (Sigma Aldrich, USA) mixed with 0.5 M NaCl. The salt solution consisted of 0.214 M NaCl and the electrode rinse solution consisted of 0.5 M Na_2SO_4 (VWR, the Netherlands). The electrode rinse solution was selected from the study of Veerman et al.⁵¹ for its stability and non-toxicity. All electrolyte solutions are pumped through the flow battery with recycling. The measured OCV (0.83 V) represents the voltage where the flow battery is considered full (corresponding to 100% State of Charge, SOC) and is used in next experiments as signal to stop charging.

Next, constant current density experiments (9 charge and 9 discharge experiments) were performed. At the start of each experimental run 50 g of 0.5 M NaCl solution (ESCO, the Netherlands) was inserted in the acid and base bottles and 175 g of 0.5 M NaCl solution inside the salt bottle. The additional solution inside the salt bottle with respect to the acid and base

bottle is there to reduce the concentration gradients of sodium chloride concentrations over the AEM and CEM once the flow battery is charged. The rinse solution bottle was filled with 5 kg of 0.5 M Na₂SO₄ solution (VWR, the Netherlands). The charge steps (3 x 50, 100 and 150 A m⁻²) are followed by discharge steps (3 x 5, 10 and 15 A m⁻²) yielding 9 datasets with full charge and discharge cycles. The discharge experiments are stopped once cell potential reaches zero volt. The x-axis in figure 5.4 shows exactly how the datasets are compiled. The discharge current density was limited to a maximum value of 15 A m⁻², as the bipolar membrane was experimentally shown to delaminate at a current density of ~20 A m⁻².

During all constant current density experiments the current is interrupted at regular intervals to measure the OCV. This OCV is a measure for SOC of the flow battery. In addition, regular interruption of current allows for measurement of the internal resistance of the flow battery. By using chronopotentiometry^{52,53}, the total internal resistance R_i is measured including its non-ohmic part ($R_{non-\Omega}$) and ohmic part (eq. 5.4).

Finally, the coulombic efficiency for the charge process is calculated. From our initial OCV test we know the theoretical capacity of a fully charged flow battery. The actual capacity during the charge steps is measured. By dividing the theoretical capacity with the measured capacity, the η_{CE} for charging is calculated.

5.4 Results and Discussion

In this section, we will first present charge and discharge behaviour of an AB-FB and next discuss main energy dissipation mechanisms.

5.4.1 Charge and discharge characteristics

This section shows and discusses typical charge and discharge characteristics of an AB-FB.

In figure 5.3 A we show three complete charge-discharge cycles. Each cycle starts with neutral 0.5 M NaCl solutions in the acid, base and salt reservoirs. The left area (“charge”) shows the mean of three separate charge experiments with 100 A m⁻². To show the high reproducibility of the experiments, error bars showing 2 standard deviations from the mean are included. Charging was stopped when the flow battery acquired an OCV of 0.83 V, a value that corresponds to a pH of the acid compartment of 0 and the base compartment of 14 (Materials and Method). Three separate discharge steps are shown in the right area (“discharge”) of figure 5.3 A, with current densities of 5 A m⁻², 10 A m⁻² and 15 A m⁻². The discharge experiments continued until discharge power reached zero. With increasing discharge current density, measured cell voltage decreased as expected from eq. 5.5 and expected resistance. At the end of the discharge curves, a steep decrease in potential occurred. This is explained by the depletion of acid and base, see section 4.2 for more details about acid/base depletion. The vast majority of the energy is stored at the right-hand side of figure 5.2 (pH 0-1). With a constant current density experiment, cell potential will decrease rapidly when the flow battery is nearly discharged (pH>2) because most of the protons and hydroxyl ions are depleted from the acid and base compartment. This steep potential

drop is a clear indication to stop the discharge step as only almost negligible energy is still available in the solutions.

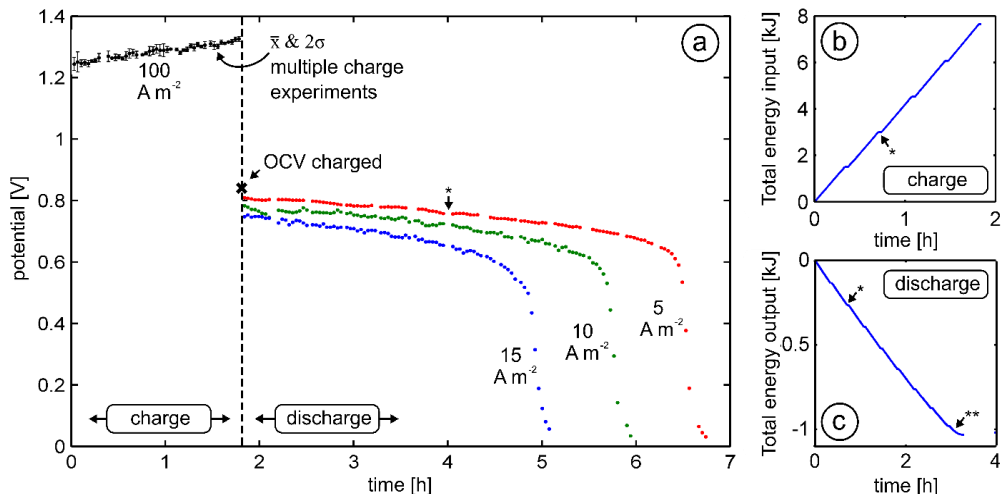


Figure 5.3. (A) Charge at constant current followed by constant current discharge voltage measurements versus time in hours. At $t=0$, the flow battery starts charging at 100 A m^{-2} until it reaches an OCV value of 0.83 V . The data points are the average values of 3 separate charge experiments repeated under identical conditions. The error bars represent 2 standard deviations (σ) from the mean. Three separate discharge current densities are shown: 5 A m^{-2} (red), 10 A m^{-2} (green) and 15 A m^{-2} (blue). (B) Total energy input (kJ) in the flow battery versus time (h) during charge (100 A m^{-2}). (C) Total energy output (kJ) from the flow battery versus time (h) during discharge (15 A m^{-2}). (A-C) At regular intervals current is briefly interrupted for measuring the OCV of the flow battery. The single asterisks show a few examples and explain the small areas with no voltage measurements.

Figure 5.3 B shows total energy spent as function of time. Figure 5.3 C shows total energy extracted as function of time. Because cell potentials remain nearly constant during charge and discharge (figure 5.3 A), the lines in figure 5.3 B and C are both nearly linear for the whole charge and discharge step except for the discharge step at the end. This implies that with exception of the very last end of the discharge step (marked with two asterisks), η_{VE} does depend little on how far the flow battery is charged and discharged.

In panels A-C in figure 5.3 at regular intervals a few data points are missing where the OCV is measured. Several single asterisks show examples of such intervals where temporarily the charge and discharge process are on hold.

5.4.2 Main dissipation sources

This section discusses efficiency and main dissipation sources of the AB-FB to better understand how to improve its performance. Figure 5.4 A shows various efficiencies of the AB-FB including coulombic, η_{CE} , voltage, η_{VE} and round trip, η_{RTE} , efficiencies of 9 charge-discharge cycles performed at different current densities. We found that the η_{CE} of all cycles is rather low and ranges between 13 and 27%.

Low η_{CE} is most likely mainly caused by unwanted mass transport ^{12,27}. Unwanted mass transport which occurs inside an AB-FB includes proton, hydroxyl, sodium and chloride ions as well as water transport. The change of pH in both salt (to ~pH 2) and rinse solutions (to ~pH 2.5) indicates that leakage of protons, and probably hydroxyl ions over AEM and CEM occurs. This is in line with the high mobility of these ions in aqueous environments due to their small size and the Grotthuss mechanism ^{54,55}. Also, the driving force for these ions is large as the concentration difference over the AEM and CEM for protons and hydroxyl ions can be as high as 1 M for a fully charged flow battery. This ion leakage leads to recombination of protons and hydroxyl ions in all compartments. Importantly, the ion recombination occurring outside the bipolar membrane does not contribute to a membrane potential and thus substantial amount of energy is being lost inside acid-base flow battery. Ramp et al. ²⁷ and Emrén et al. ²¹ also reported high proton and hydroxyl ion leakage as major energy dissipation source for the same system. The large energy loss by leakage of protons and hydroxyl ions is represented in figure 5.4 B as a green bar (39-65%). Besides proton and hydroxyl ion leakage, also unwanted water and salt transport can take place. The acid and base carry by far most energy in the flow battery (eq. 5.2). Therefore, unwanted sodium and chloride ion transport is not expected to be responsible for the high energy losses presented by the green bar in figure 5.4 B. Also, water transport cannot account for the large energy dissipation shown by the green bar. In a CGFB, water transport causes a significant decrease in the ratio of concentrations over a membrane, leading to an appreciable loss in cell potential and energy ^{12,13}. In an AB-FB however, cell potential is hardly affected by water transport, as the concentration of proton and hydroxyl ions inside the membrane remains 10^{-7} and the concentration ratio over the two sides of a bipolar membrane is several factors higher compared to a CGFB.

The low η_{CE} values are unacceptably low for an electricity storage system. To find out whether the charge or discharge step is responsible for the low η_{CE} , the coulombic efficiency of the charging step is calculated and shown in table 5.1.

Table 5.1. Measured amount of charge in during charge phase, theoretical charge capacity and charging η_{CE} as function of charging current density.

$I_{A,c}$ (A m ⁻²)	Total charge in (Ah L ⁻¹)	Theoretical charge capacity (Ah L ⁻¹)	Coulombic efficiency charging (-)
50	35.8	26.8	0.75
100	33.3	26.8	0.80
150	30.4	26.8	0.88

Table 5.1 shows increasing charge η_{CE} with increasing current density. The highest charge current density (150 A m⁻²) even reaches a high charge η_{CE} of 88%. This can be explained by the decreasing contact times of the solutions. If the flow battery is charged fast, there is less time for the concentration gradient driven diffusion process to occur and charge η_{CE} increases. Looking

at figure 5.4 A we can see this is also true for discharging. With increasing discharge current, η_{CE} increases. Comparing overall η_{CE} (13-27%) with charge η_{CE} (75-88%), we find that the discharge step contributes most to a low overall η_{CE} . This is exactly what we would expect based on the longer contact times of the solutions during the discharge step. In general, we believe that the η_{CE} can be drastically improved by increasing discharge current densities. However, delamination sets an upper limit on the current density applied. Bipolar membranes with high water permeability would be necessary to allow higher discharge current densities. Another way of increasing the discharge current density without causing delamination to occur could be to include osmotic ballast in the acid and base solution to increase the rate in which water is transported out of the bipolar membrane into solution ⁵⁶.

The voltage efficiencies of all experiments, as shown in figure 5.4 A, are measured to be between 41 and 63%. This is lower compared to other flow batteries and CGFBs. Vanadium redox-flow batteries for example show voltage efficiencies ranging from 85-95% ⁵⁷ while they operate at much higher current densities of 500-1000 A m⁻². A CGFB however has a voltage efficiency ranging between 60-80% ¹² and is most similar to the AB-FB. The measured low voltage efficiencies of an AB-FB can be explained by relatively high internal resistance. Increasing the charge current density is not favourable in terms of η_{RTE} . Comparing dataset 6 (100 A m⁻² charge) with dataset 9 (150 A m⁻²) for example shows that although η_{CE} is increased by increasing current density, the associated η_{VE} is much lower leading to an overall decline in η_{RTE} . A solution for increasing the η_{VE} and η_{RTE} might be using thinner solution compartments and membranes. In this case, higher charge current densities could be obtained with higher η_{VE} . Also, higher discharge current densities could be obtained since water could diffuse faster from thinner membrane layers in the bipolar membrane.

The effect of internal resistance is also visible in figure 5.4 B. Here, the red and purple bar show the energy losses caused by ohmic (Ω) and non-ohmic (non- Ω) resistance. The contribution of the ohmic resistance (23-45%) is larger than the non-ohmic resistance (4-5%). Figure 5.4 B shows that the non-ohmic resistance increases only very little with increasing current. This can be explained by increasing concentration polarization occurring at the membrane interfaces ⁵⁸.

Round trip efficiencies are presented in figure 5.4 A (as η_{RTE}) and 4 B (as % energy harvested). Because of the low η_{CE} during the discharge process, the overall round trip efficiencies are low. In summary, results show that with state-of-the art membranes it is possible to have stable operation of the AB-FB at high energy density (pH 0-14). Round trip efficiency is low, because of low coulombic efficiency, especially during discharge. Discharge current density is limited by delamination of the bipolar membrane. With suggested improvements, the roundtrip efficiency might be increased significantly.

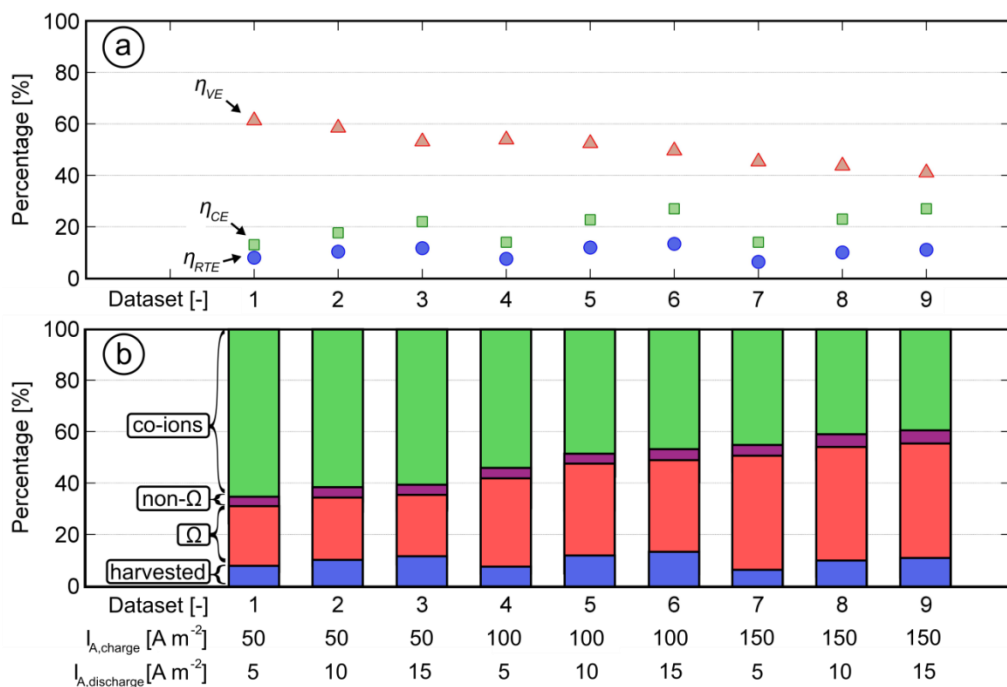


Figure 5.4. (A) The voltage efficiency (η_{VE}), coulombic efficiency (η_{CE}) and round-trip efficiency (η_{RTE}) for 9 different combinations of charge currents and discharge currents. (B) Distribution of energy dissipation and amount of energy harvested for 9 different combinations of charge currents and discharge currents. Each combination is called a dataset and is numbered 1-9. The actual charge ($I_{A,charge}$) and discharge ($I_{A,discharge}$) current densities used in each dataset are listed below panel B.

5.5 Conclusions

We have demonstrated that by deep charge and discharge (up to 1 M of acid and base), the AB-FB can reach power densities up to $3.7\ W\ m^{-2}$ per membrane, energy densities up to $2.9\ Wh\ kg^{-1}$ and round-trip efficiencies up to 13.5%.

The measured coulombic efficiencies are moderate (13-27%). This is mainly caused by unwanted proton transport and hydroxyl ion transport. We observed that coulombic efficiency reaches higher values at higher charge and discharge current densities. This is attributed to the shorter contact period of the solutions at high current density. The total energy lost by co-ion transport is estimated to be 39-65% and therefore development of proton and hydroxyl blocking membranes is timely and needed.

Reported voltage efficiencies are modest (41-63%) and this is a result of a relatively high internal resistance caused by thick solution compartments and membranes. Key performance parameters (specific energy, power density and round-trip efficiency) can be improved by reducing the internal resistance by using thinner solution compartments and membranes. By applying higher discharge current densities, higher power densities will be achieved. In addition, because of

lower contact time of the solutions, lower proton and hydroxyl ion leakage will occur and thus higher round trip efficiencies would be obtained.

This work shows improved AB-FB performance and identifies routes for further improvement. In view of the potential environmental benefits of a mature AB-FB energy storage system, further investigation of the AB-FB system as future technology for large-scale electricity storage is considered justified.

Acknowledgements

This work was performed in the cooperation framework of Wetsus, European Centre of Excellence for Sustainable Water Technology (www.wetsus.nl). Wetsus is co-funded by the Dutch Ministry of Economic Affairs and Ministry of Infrastructure and Environment, the Province of Fryslân and the Northern Netherlands Provinces. The authors like to thank the participants of the research theme “Blue Energy” for the fruitful discussions and their financial support. In addition, the authors like to thank researchers Laura Tabernero Cogul, Eline Jagtenberg, Mei Nelissen and Lotte van der Velde for their efforts in performing preliminary experiments.

5.6 References

- (1) Dunn, B.; Kamath, H.; Tarascon, J.-M. *Science* (80-.). **2011**, 334 (6058), 928–935.
- (2) Hirth, L. *Appl. Energy* **2016**, 181, 210–223.
- (3) Hameer, S.; van Niekerk, J. L. *Int. J. Energy Res.* **2015**, 39 (9), 1179–1195.
- (4) Dincer, I.; Acar, C. *Int. J. Energy Res.* **2015**, 39 (5), 585–606.
- (5) Larcher, D.; Tarascon, J. M. *Nat Chem* **2015**, 7 (1), 19–29.
- (6) Sternberg, A.; Bardow, A. *Energy Environ. Sci.* **2015**, 8 (2), 389–400.
- (7) Carbajales-Dale, M.; Barnhart, C. J.; Benson, S. M. *Energy Environ. Sci.* **2014**, 7 (5), 1538–1544.
- (8) Barnhart, C. J.; Dale, M.; Brandt, A. R.; Benson, S. M. *Energy Environ. Sci.* **2013**, 6 (10), 2804–2810.
- (9) Tucker, M. C.; Phillips, A.; Weber, A. Z. *ChemSusChem* **2015**, 8 (23), 3996–4004.
- (10) McKerracher, R. D.; Ponce de Leon, C.; Wills, R. G. A.; Shah, A. A.; Walsh, F. C. *Chempluschem* **2015**, 80 (2), 323–335.
- (11) Huskinson, B.; Marshak, M. P.; Suh, C.; Er, S.; Gerhardt, M. R.; Galvin, C. J.; Chen, X.; Aspuru-Guzik, A.; Gordon, R. G.; Aziz, M. J. *Nature* **2014**, 505 (7482), 195–198.
- (12) Kingsbury, R. S.; Chu, K.; Coronell, O. *J. Memb. Sci.* **2015**.
- (13) van Egmond, W. J.; Saakes, M.; Porada, S.; Meuwissen, T.; Buisman, C. J. N.; Hamelers, H. V. M. *J. Power Sources* **2016**, 325, 129–139.

- (14) Sáez, A.; Montiel, V.; Aldaz, A. *Int. J. Hydrogen Energy* **2016**, *41* (40), 17801–17806.
- (15) Ludwig, F. A. Acid-base concentration cell for electric power generation. EP 0613199 A1, 1994.
- (16) Rydh, C. J. *J. Power Sources* **1999**, *80* (1), 21–29.
- (17) Tarascon, J.-M. *ChemSusChem* **2008**, *1* (8–9), 777–779.
- (18) Bresser, D.; Paillard, E.; Passerini, S. In *Advances in Batteries for Medium and Large-Scale Energy Storage*; 2015; pp 125–211.
- (19) Ulaganathan, M.; Jain, A.; Aravindan, V.; Jayaraman, S.; Ling, W.C.; Lim, T.M.; Srinivasan, M.P.; Yan, Q.; Madhavi, S. *J. Power Sources* **2015**, *274*, 846–850.
- (20) Barnhart, C. J.; Benson, S. M.; Cui, Y.; McGregor, P. G.; Mulheran, P. a.; Hall, P. J.; Zavadil, B. *Energy Environ. Sci.* **2013**, *6* (4), 1083.
- (21) Emrén, A. T.; Holmström, V. J. M. *Energy* **1983**, *8* (4), 277–282.
- (22) Chen, H.; Cong, T. N.; Yang, W.; Tan, C.; Li, Y.; Ding, Y. *Prog. Nat. Sci.* **2009**, *19* (3), 291–312.
- (23) Kear, G.; Shah, A. A.; Walsh, F. C. *Int. J. Energy Res.* **2012**, *36* (11), 1105–1120.
- (24) Chatzivasileiadi, A.; Ampatzi, E.; Knight, I. *Renew. Sustain. Energy Rev.* **2013**, *25*, 814–830.
- (25) Luo, X.; Wang, J.; Dooner, M.; Clarke, J. *Appl. Energy* **2015**, *137*, 511–536.
- (26) Park, J.-H.; Kim, C.-G.; Lee, Y.-H. *Int. J. Energy Res.* **2016**, *40* (5), 685–691.
- (27) Ramp, F. L. *Nature* **1979**, *278* (5702), 335–337.
- (28) Zholkovskij, E. K.; Müller, M. C.; Staude, E. *J. Memb. Sci.* **1998**, *141* (2), 231–243.
- (29) Pretz, J.; Staude, E. *Berichte der Bunsengesellschaft für Phys. Chemie* **1998**, *102* (4), 676–685.
- (30) Kim, J.-H.; Lee, J.-H.; Maurya, S.; Shin, S.-H.; Lee, J.-Y.; Chang, I. S.; Moon, S.-H. *Electrochem. commun.* **2016**, *72*, 157–161.
- (31) Walther, J. F. *US Patent 4311771*. 1982.
- (32) Strathmann, H. *Ion-exchange membrane separation processes*; Elsevier: Amsterdam, 2004; Vol. 9.
- (33) Wang, Q.; Wu, B.; Jiang, C.; Wang, Y.; Xu, T. *J. Memb. Sci.* **2017**, *524*, 370–376.
- (34) Wilhelm, F. G.; Pünt, I.; van der Vegt, N. F. A.; Strathmann, H.; Wessling, M. *Ind. Eng. Chem. Res.* **2002**, *41* (3), 579–586.
- (35) Huang, C.; Xu, T. *Environ. Sci. Technol.* **2006**, *40* (17), 5233–5243.
- (36) Xu, T.; Huang, C. *AIChE J.* **2008**, *54* (12), 3147–3159.

- (37) Galama, A. H.; Saakes, M.; Bruning, H.; Rijnaarts, H. H. M.; Post, J. W. *Desalination* **2014**, *342*, 61–69.
- (38) Galama, A. H.; Daubaras, G.; Burheim, O. S.; Rijnaarts, H.; Post, J. W. *J. Memb. Sci.* **2014**, *452*, 219–228.
- (39) van Egmond, W. J.; Starke, U. K.; Saakes, M.; Buisman, C. J. N.; Hamelers, H. V. M. *J. Power Sources* **2017**, *340*, 71–79.
- (40) Wilhelm, F. G.; Vught, F. A. Bipolar Membrane Electrodialysis Membrane Development and Transport Characteristics, Twente University: Enschede, 2001.
- (41) Kariduraganavar, M. Y.; Kittur, A. A.; Kulkarni, S. S. In *Ion Exchange Technology I: Theory and Materials*; 2012; pp 233–276.
- (42) Bazinet, L. *Crit. Rev. Food Sci. Nutr.* **2005**, *45* (4), 307–326.
- (43) Simons, R. *Nature* **1979**, *280* (5725), 824–826.
- (44) Strathmann, H.; Krol, J. J.; Rapp, H. J.; Eigenberger, G. *J. Memb. Sci.* **1997**, *125* (1), 123–142.
- (45) Zabolotskii, V. I.; Gnusin, N. P.; Pis'menskaya, N. D.; Shel'deshov, N. V. *Elektrokhimiya* **1986**, *21* (8).
- (46) Sheldeshov, N. V.; Zabolotskii, V. I.; Pis-menskaya, N. D.; Gnusin, N. P. *Elektrokhimiya* **1986**, *22* (6).
- (47) Wang, W.; Wei, X.; Choi, D.; Lu, X.; Yang, G.; Sun, C. In *Advances in Batteries for Medium and Large-Scale Energy Storage*; Skyllas-Kazacos, M., Lim, T. M., Eds.; Woodhead Publishing, 2015; pp 3–28.
- (48) Lu, R.; Yang, A.; Xue, Y.; Xu, L.; Zhu, C. In *EVS 2010 - Sustainable Mobility Revolution: 25th World Battery, Hybrid and Fuel Cell Electric Vehicle Symposium and Exhibition*; 2010.
- (49) Veerman, J.; De Jong, R. M.; Saakes, M.; Metz, S. J.; Harmsen, G. J. *J. Memb. Sci.* **2009**, *343* (1), 7–15.
- (50) Veerman, J.; Post, J. W.; Saakes, M.; Metz, S. J.; Harmsen, G. J. *J. Memb. Sci.* **2008**, *310* (1–2), 418–430.
- (51) Veerman, J.; Saakes, M.; Metz, S. J.; Harmsen, G. J. *J. Appl. Electrochem.* **2010**, *40* (8), 1461–1474.
- (52) Vermaas, D. A.; Saakes, M.; Nijmeijer, K. *Electrochim. Acta* **2014**, *117*, 9–17.
- (53) Sizat, P.; Pourcelly, G. *J. Memb. Sci.* **1997**, *123* (1), 121–131.
- (54) Tuckerman, M. E.; Marx, D.; Parrinello, M. *Nature* **2002**, *417* (6892), 925–929.
- (55) Robinson, R. A.; Stokes, R. H. *Electrolyte solutions*, 2nd ed.; Courier Corporation: Armidale, 2002.

- (56) Kingsbury, R. S.; Coronell, O. *Environ. Sci. Technol.* **2016**.
- (57) Skyllas-Kazacos, M.; Kazacos, G.; Poon, G.; Verseema, H. *Int. J. Energy Res.* **2010**, *34* (2), 182–189.
- (58) Vermaas, D. A.; Saakes, M.; Nijmeijer, K. *J. Memb. Sci.* **2014**, *453*, 312–319.

Chapter 6

General discussion and outlook

Chapter 1 discussed that there is a need for sustainable large scale electrical energy storage and it was found that no technology exists that is sustainable, safe and politically favourable. The concentration gradient flow battery (CGFB) was introduced as possible solution to this need as it stores energy in plain NaCl solutions. Chapter 2 till 5 discussed technological aspects of a CGFB and found that is indeed possible to store energy in salinity gradients. Current systems are limited by undesirable mass transport and high internal resistance but these issues can partly be overcome by improvements suggested such as proper operating conditions or meshed membranes. This chapter aims to discuss whether a CGFB can fulfil the requirements for future large scale EES as discussed in chapter 1 from a societal and commercial point of view. A cost analysis is performed followed by a sensitivity analysis showing key parameters that are interesting to improve. Subsequently, sustainability, safety and size of the CGFB are analysed and discussed in more detail.

6.1 Theory of energy flow, revenue and costs of a storage system

In order to compare a CGFB with other storage systems and to make calculations for profitability, first theory of energy flow, revenue and costs is discussed in this section. Figure 6.1 shows an energy flow diagram of a full charge/discharge cycle of a battery system.

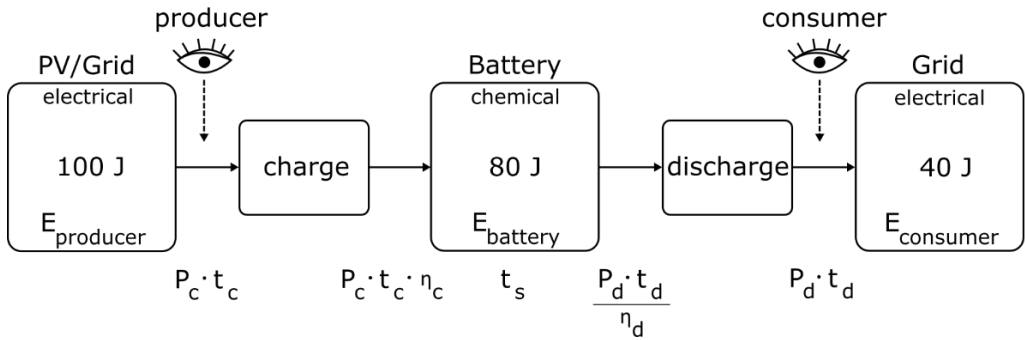


Figure 6.1. Flow diagram of energy during a charge/discharge cycle of a battery system. The two eyes show what is most interesting from the perspective of a producer and a consumer. Equations below the arrows show the magnitude of energy transferred.

The input of energy of a battery can be derived from different sources (e.g. photovoltaics or the electricity grid). The input energy is represented in figure 6.1 by $E_{producer}$ and is set at 100 Joules as example value. The source of energy supplies energy for a certain amount of time (charging time t_c) at a certain power (charge power P_c). Input energy ($E_{producer}$) is calculated by

$$E_{producer} = P_c t_c \quad \text{eq. (6.1)}$$

For a producer looking at ways for selling/delivering energy these parameters are of most interest. The perspective of the producer is represented by the eye symbol ‘producer’ in figure 6.1. The charging process is a dissipative process, a fraction of input energy is lost. The total

amount of energy left over after charging is calculated by multiplying the input energy with the charge efficiency (η_c).

$$E_{battery} = P_c t_c \eta_c \quad \text{eq. (6.2)}$$

After charging, electrical energy ($E_{producer}$) has been converted into chemical energy in the battery ($E_{battery}$) where it can reside for a certain amount of time (storage time, t_s). The CGFB has no storage loss. The chemical energy stored is set at 80 Joules as example value. When power is needed, discharge is initiated. Importantly, the consumer of electricity is only interested in the amount of electric power actually delivered (P_d) and the period of time of delivery (discharge time, t_d). The eye symbol ‘consumer’ shows the parameters most interesting from the perspective of the consumer. The energy supplied to the consumer ($E_{consumer}$) is calculated by

$$E_{consumer} = P_d t_d \quad \text{eq. (6.3)}$$

and set at 40 Joules as example. Energy density of a storage system is defined from the perspective of the consumer as well. Energy density can be calculated by

$$E_{density} = \frac{E_{consumer}}{V_s} \quad \text{eq. (6.4)}$$

where V_s is the volume of storage. During the discharge process, also energy is dissipated. The chemical energy drawn from the battery system ($E_{battery}$) is calculated by dividing the actual amount of energy delivered, $E_{consumer}$ by the discharge efficiency, η_d . Assuming full discharge, eq. 6.2 can thus alternatively also be written as

$$E_{battery} = P_c t_c \eta_c = \frac{P_d t_d}{\eta_d} \quad \text{or} \quad t_c = \frac{P_d t_d}{P_c \eta_c \eta_d} \quad \text{eq. (6.5)}$$

In literature, round trip efficiency is an often used parameter. Round trip efficiency (η_{RT}) is the fraction of energy actually delivered ($E_{consumer}$) compared to the total amount of energy input ($E_{producer}$) and is calculated by

$$\eta_{RT} = \frac{E_{consumer}}{E_{producer}} = \eta_c \eta_d \quad \text{eq. (6.6)}$$

From eq. 6.5 the energy density can be derived in an alternative way. Dividing $E_{battery}$ by the volume of the battery, V_s , gives the theoretical energy capacity of the battery system. Dividing eq. 6.5 by the volume, rearranging and substitution of eq. 6.4 gives

$$E_{density} = \frac{E_{battery}}{V_s} \eta_d \quad \text{eq. (6.7)}$$

Eq. 6.7 shows that the energy density of a battery system is improved when discharge efficiency improves. This is especially interesting for the CGFB which has a relatively low energy density and round-trip energy efficiency. Improvement of the discharge efficiency will help to improve both the round-trip efficiency (eq. 6.6) and energy density (eq. 6.7).

To assess whether a CGFB system can compete with existing technologies on an economic level, a metric is often used. Here, the price is expressed in € kWh⁻¹, where the capital costs of the battery are divided by the amount of kWh a battery delivers in a single discharge ($E_{consumer}$). For an operator of a battery this is not a very useful metric since it does not take into account the amount of cycles a battery can sustain or the round-trip efficiency. A more useful metric is the costs per kWh per cycle (€ kWh⁻¹ cycle⁻¹). Here, total costs of a battery are spread out over the total amount of kWh a storage system delivers in its entire lifetime, taking into account the round trip efficiency, operational costs and charging costs as well ¹⁻⁴. This metric is also known as Levelized Cost of Storage (LCOS). When the price of electricity delivered is higher than the LCOS, profitable operation is possible. In section 6.3 the LCOS is calculated for a CGFB and compared to other storage technologies. Calculating the costs (and revenues) per unit of energy per cycle is not only useful for comparing different storage technologies, it is also useful for calculating overall profitability of a storage system and studying how different parameters affect profitability.

The net income per charge/discharge cycle can be expressed as

$$profit = R - LCOS \quad \text{eq. (6.8)}$$

where R is the revenue of a storage system expressed per kWh discharged and is equal to p_d , the price of a unit of energy (e.g. kWh) when the battery ‘sells’ it to the consumer (e.g. a battery operator delivers energy to the grid when demand is high). The LCOS of a system is calculated by (e.g. ⁵⁻⁷)

$$LCOS = \frac{\sum (C_{CAP} + C_{O\&M} + C_c - R_s)(1+i)^{-t}}{\sum E_{consumer,t}(1+i)^{-t}} \quad \text{eq. (6.9)}$$

where C_{CAP} are the capital costs in year t , $C_{O\&M}$ the operational and maintenance costs in year t , C_c the charging costs in year t , $E_{consumer,t}$ total actual electricity delivered to a consumer in year t and i the interest rate. Capital costs are the costs for the initial investment in battery system and includes for example costs for the power components (stack with membranes in case of a CGFB), the energy storage part (reservoirs with water in case of a CGFB) and ancillary equipment. Operational and maintenance costs, $C_{O\&M}$, are yearly returning costs. Charging costs, C_c , are yearly costs for buying the electricity when the battery charges. Finally, at the end of system life,

there might be some residual value left. In this case residual value R_s is a revenue and is subtracted from the costs. Combining eqs. 6.5, 6.8 and 6.9 yields

$$profit = R - LCOS = p_d - \frac{\sum \left(C_{CAP} + C_{O\&M} + \frac{P_d t_d P_c}{\eta_c \eta_d} n_y \right) (1+i)^{-t}}{\sum P_d t_d n_y (1+i)^{-t}} \qquad \text{eq. (6.10)}$$

For a given selling price p_d , equation 6.10 shows how much profit can be made with a given battery system (e.g. when $R=LCOS$, the system reaches break-even in terms of costs). The next section discusses sources of revenue for storage systems. The section after that calculates the LCOS of the CGFB and compares it to other storage technologies. Subsequently a sensitivity analysis is performed on the LCOS to identify what are valuable research directions for commercial improvement of a CGFB system.

6.2 Sources of revenue for an energy storage system

In creating a profit, both revenue and costs are of interest. Although the primary incentive to study the CGFB is the need of large scale EES, there is no need to ignore the many other sources of revenue for a storage system. This section introduces the possible sources of revenue of an energy storage system. Figure 6.2 shows the sources of revenue for an entire electricity chain as has been extensively analysed by Rastler et al. ⁸.

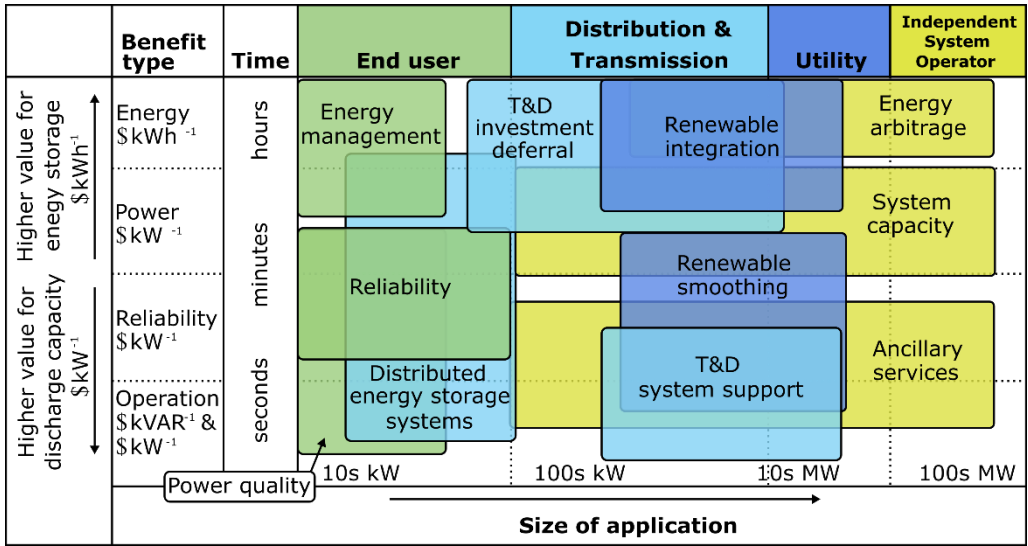


Figure 6.2. Different uses of energy storage and revenue sources. Figure adapted from the work of Rastler et al.⁸. The x-axis shows application from small scale (end-user) to large scale (utility/grid operators). The y-axis differentiates application of storage based on the value of energy storage (€ kWh⁻¹) and value of power (€ kWh⁻¹).

The x-axis in figure 6.2 shows different places along the energy supply chain, from small scale (left, end-user) to large scale (right, utility and system operator). The size of the storage

application increases also from left to right from ~10 kW to ~>100 MW. All storage technologies have a certain energy storage capacity (measured in kWh) and a certain discharge capacity (measured in kW). Depending on the application, in some cases the energy storage capacity is more important and adds more value whereas in other cases the discharge capacity is more important. The y-axis shows four different general categories of benefit types. The four different categories (energy, power, reliability and operations) are ordered depending on the relative importance of either energy storage capacity (towards top) or discharge capacity (towards bottom). As example, for renewable energy integration it is valuable to be able to discharge for multiple hours at a certain power. In this case energy storage capacity is especially important so ‘renewable integration’ is located at the top of the y-axis. Another example is power quality. Here the storage system helps to stabilize the frequency and voltage. In this case energy storage capacity is not very important since the discharge and charge times are in the order of seconds⁹. In this case discharge capacity is valued over energy storage capacity and therefore ‘power quality’ is located more towards the bottom of the y-axis. Next to the column with benefits, a time frame showing typical discharge times is given. The most common revenue streams will be discussed.

Power quality is typically related to the wave form of the voltage and frequency. Voltage, frequency and waveform should comply with standards to protect devices⁹. Energy storage systems help to meet these standards. Power reliability means that batteries make sure that power is always available. Examples include uninterruptible power supplies (UPS) or emergency power systems (EPS) which can be used in data centres or hospitals¹⁰. Energy management is related to homes, offices or industries that shift energy usage and supply to maximize revenue or decrease costs⁸. An example would be storing solar energy during day time for use during the evening. Another category is related to generating revenue by reducing investment costs or “T&D investment deferral” (where T&D means transmission and distribution)^{1,8}. An example could be that for example a smaller power line is constructed to a new wind park because an energy storage system is installed adjacent to it. The battery system absorbs peak output and therefore the power line can be made less expensive. Battery systems can also help to stabilize the energy grid when wind and solar energy is added to the grid. The batteries can act as voltage support and frequency control or as rapid response to wind or solar energy spikes^{8,11,12}. On the larger scale an example of a system capacity application would be a battery system that delivers or accepts power to or from the grid when supply and demand do not match (balancing) due to poor forecasting or some technical failure¹³. Another example would be the service of providing power to reboot energy infrastructure in case of a system wide malfunction, named ‘black start’ or system restoration^{8,13}. Finally, trading energy on the electricity market is also a source of revenue. This type of trade is referred to as “energy arbitrage”. Battery owners (which need to be eligible for market access) can buy and sell blocks of energy on the markets. This can be done day-ahead but also on intraday basis. Renewable energy time shift trading is a subset of energy trading. It involves buying excess renewable electricity at a low price and selling it later a higher price. Interesting to note is that although consumers are not yet trading electricity, in the future

this could become the case. At the moment home owners with solar panels installed typically have power purchase agreements which guarantees that they can sell their energy at a fixed rate. In the future however, with increased intermittent sources of energy connected to the grid, it is uncertain whether these agreements will remain. If not and consumers need to start paying and delivering for actual electricity prices, home owners would benefit from installing a battery next to their solar panels. In this case they can trade electricity in a similar way as a battery owner can do now on a large scale. The Tesla Powerwall is a well-known example for such battery system. As discussed in chapter 1, large scale energy storage is likely to become increasingly important. This will also have a large effect on the energy trading markets (e.g. during sunny hours electricity prices could drop significantly). Energy arbitrage is a straightforward way of generating a revenue and therefore the next subsection (6.2.1) will explore this revenue source in more detail. Important to note is that tapping into multiple revenue streams with a single storage system is not only possible but encouraged ^{1,14–18} for increasing total revenue. Section 6.5 will discuss this option with examples in more detail and here we first focus on arbitrage.

6.2.1 Large scale energy trading

This subsection shows actual electricity trading prices of the German electricity market to explore energy arbitrage as possible revenue source for the CGFB. Germany is chosen since it has a large well-developed economy and energy infrastructure and it also already has a significant fraction of renewable power generation because of their ‘Energiewende’ policy.

Because of addition of renewable energy to the German electrical grid, electricity in bulk on the German electricity spot market (EPEX SPOT) is now traded in blocks of 15 minutes instead of hours to better facilitate supply and demand. Figure 6.3 shows the averaged maximum and minimum electricity spot price in Germany and Austria for each day in 2015 ¹⁹.

Just as on the stock market, you would like to buy low and sell high. It is of interest to see how that turns out with the data in figure 6.3. All energy is traded in blocks of 15 minutes. At the end of each 15 minutes the average price against which the energy was traded is calculated. This value represents the value or price of electricity of that moment of the day. There are 96 quarters of hour during the day, this means that each day generates 96 prices. For each day, both the lowest (blue dots) and highest (red dots) price are displayed in figure 6.3. Ideally, as in a stock market, a trader would like to buy at the price level of the blue dot and sell at the price level of the red dot. This method is the most straightforward way of making a profitable trade. The grey bars show exactly how much revenue this method generates each day and it is called maximum daily arbitrage. Note that the revenue here (arbitrage or $p_d - p_c$) is not the same as the revenue in section 6.1 (p_d). This has to do with the fact that some energy which is bought by the battery owner is lost because of energy dissipation ($\eta_{RT} < 100\%$).

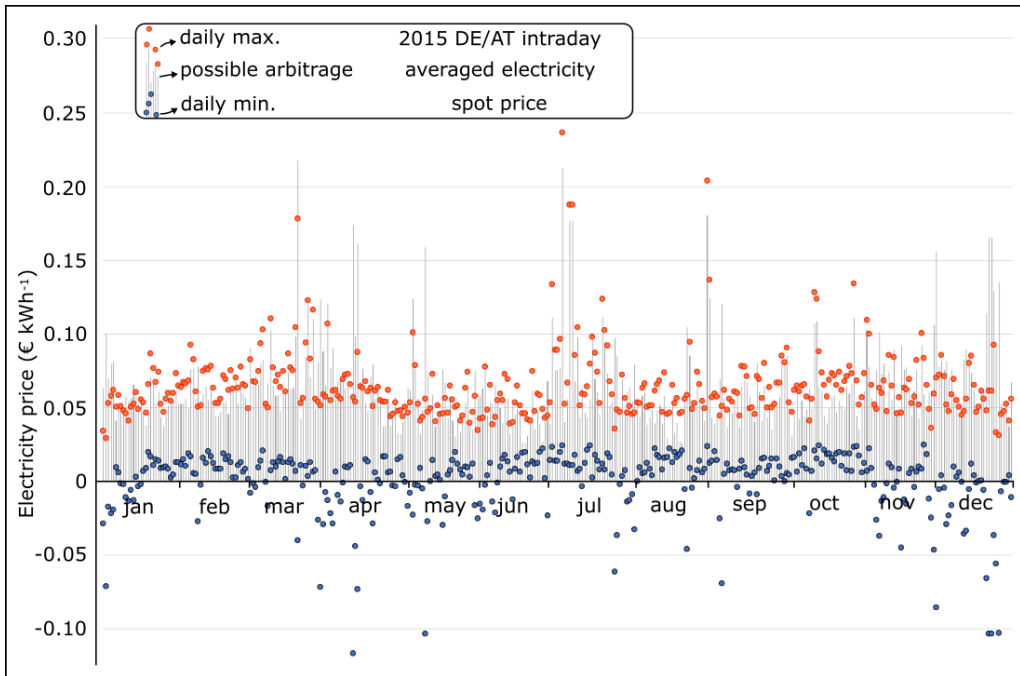


Figure 6.3. Electricity prices from the German and Austrian electricity market for a complete year (EPEX SPOT, 2015¹⁹). For each day, only the quarter of an hour with the lowest averaged traded price (blue dots) and the quarter of an hour with the highest averaged traded price (red dots) are shown. The difference between the high and low prices represent the highest possible arbitrage that day (grey bars).

One of the interesting things to notice in figure 6.3 is that many times per year the electricity price is zero or negative. This occurs often when it is very sunny or wind is strong and demand is low. For a wind or solar park owner this is not ideal, it means that they do not earn money for their delivered energy at these moments (assuming that there are no subsidies or fixed price delivery agreements involved). For them it would be interesting to store that energy and sell it later that day for a high price. Not only wind or solar park owners can trade electricity like this. It is also possible for a third party to use a battery and actively trade electricity in a similar manner. Maximum daily energy arbitrage varies throughout the year but from figure 6.3 it becomes clear that for the majority of days, the maximum arbitrage remains between the 0.04 and 0.08 € kWh^{-1} . Averaged over the whole year, the averaged electricity price (not shown) was 0.032 € kWh^{-1} . The average buy price (blue dots) was 0.00 € kWh^{-1} , the averaged sell price (red dots) was 0.065 € kWh^{-1} and the averaged arbitrage (grey bars) was 0.064 € kWh^{-1} . Note the word maximum in maximum daily arbitrage. The actual profit will be lower for three reasons. The first is that this method assumes that the trader has perfect foresight (it knows beforehand when it should sell or buy the energy to generate the highest revenue). The second reason why it is called maximum arbitrage is because we ‘cherry picked’ the lowest buying price and highest selling price. The second-best trade will involve a (slightly) less attractive buying and selling price and will be therefore less profitable. The third best trade will be even less profitable and so

on until there are no possible trades left for generating revenue. The third reason is that for energy storage, part of the energy is lost. So, when a battery owner buys 1MWh of electricity, it could be that he only sells back 0.5MWh (η_{RT} of 50%). In this case the actual arbitrage would be lower than the maximum arbitrage. There is one exception. If the electricity price is negative, a low energy efficiency is a good thing in financial terms. A battery system with a low energy efficiency is able to absorb and dissipate more energy than energy efficient systems. This dissipation capacity in combination with negative electricity prices means that one could actually make more profit with an energy inefficient system. Although this might be interesting from a financial point of view, the question remains whether this is interesting from an environmental point of view as a portion of potentially useful energy is wasted.

Finally, there is one more remark to make. If the capacity of the battery system allows it, besides daily storage, it would be of course also possible to store energy for multiple days. It could be for example that there is a lot of wind during the weekend and low demand. This means that it might be possible to increase revenue to buy excess power during that weekend and sell it on Monday and Tuesday. The maximum daily arbitrage does not account for this. The downside of storing energy for multiple days is that it reduces the amount of cycles a battery makes. This in turn has a negative impact on the LCOS as will be shown and explained in section 6.4 and will increase the LCOS. Therefore, storing energy for multiple days could be more profitable than daily storage but depends on the effect on the LCOS.

6.2.2 Externalities in electricity prices

Interestingly, the real costs of electricity are actually higher than shown in figure 6.3 as some costs of the production of energy are not charged to the end-user. In economics these type of costs are referred to as externalities²⁰. Burning fossil fuels for example causes a decline in air quality and this could incur additional health costs. These types of costs are not paid by the consumer of the electricity but are now borne by society as a whole. Multiple studies have been performed to estimate the size of the externalities of production of electricity using different energy sources^{21–25}. Also the European Union is interested in the magnitude of the externalities and funded a series of projects (lasting ten years, at a cost of 10 million euros) under the acronym ‘Extern-E’ to estimate the external costs²⁶. Although absolute values fluctuate, in general studies find that power production from renewable energy sources have much lower external costs than power production from fossil fuel sources^{21–26}. As example values, table 6.1 shows results from the Extern-E project.

If external costs would be included in the electricity prices, possible revenue from electricity storage could increase (assuming a high η_{RT}). Yet, in our revenue projection we do not take into account external costs in electricity prices because we assume a future where the majority of electrical power originates from a renewable source. Since externalities of renewable energy sources are estimated to be low, as result the effect of omitting the externalities from our revenue analysis will therefore likely be low as well.

Table 6.1. Estimated external costs figures for electricity production in Germany by different energy sources according to the European Extern-E research project ²⁶.

Type of energy generation	External costs € kWh ⁻¹
Wind	0.0005
PV	0.006
Gas	0.01-0.02
Coal and lignite	0.03-0.06
Oil	0.05-0.08

6.3 Costs of storage technologies

Besides revenue, costs determine possible profits. In section 6.1 the LCOS was introduced as a useful metric for comparing different storage technologies. This section will explore the LCOS of both the CGFB (analysed in chapters 2-4) and acid base flow battery (ABFB, analysed in chapter 5). In addition, it will compare these LCOS to competitors and a sensitivity analysis is performed to explore how the LCOS of the CGFB and ABFB respond to changing parameters so that useful future research directions can be outlined.

6.3.1 Costs of a CGFB and ABFB system

As discussed in chapters 1 to 5, a CGFB system and an ABFB system are composed of reservoirs with salt water, pumps, membranes, electrodes and a housing. Additionally, auxiliary equipment is necessary such as piping, wiring, electronics and connectors. Table 6.2 shows the main cost components of a large scale CGFB and ABFB with an educated guess of costs of different components. To enable an apple-to-apple comparison in section 6.3.2, the LCOS is calculated in a similar manner as is done in the work of Zakeri et al. ²⁷.

There are two scenarios in table 6.2; the energy arbitrage (or bulk energy storage) scenario and the transmission and distribution support scenario. Please also refer to figure 6.4 (and 6.2) where they are also shown. Depending on the assumptions in the scenario either power (kW) or energy (kWh) is most important. For the energy arbitrage scenario energy is most important because of the relatively long discharge time (8h). Yet, for the T&D support scenario, power is more important since discharge times are short (2h). This can also be seen in figure 6.2 where the importance of power vs. energy is shown on the y-axis. For the calculation of capital costs of the CGFB and ABFB systems it is assumed that large scale manufacturing of modules has become possible and that the size of each module is in the order of magnitude of a few kW. It is also assumed that some parts (for example membranes and housing) have become cheaper than they are now since we assume they are mass produced as well. These predicted values are based on industry estimates. The values in table 6.2 are given as costs per kW, to allow easy cross

reference with other sources. Note that the total energy delivered ($E_{consumer}$) is not a round number. This is caused by the discount factor in equation 6.10.

Table 6.2. Cost estimation of a more developed (future) CGFB and ABFB for two different business cases. The business cases with respective case assumptions are equal to the work of Zakeri et al. ²⁷ and outlined in the table. Assumed battery specifics are: (CGFB) P_d of 2 W m⁻² of membrane area, a η_{RT} of 40% and an $E_{density}$ of 0.5 kWh m⁻³. (ABFB) P_d of 15 W m⁻² of membrane area, a η_{RT} of 40% and an $E_{density}$ of 2 kWh m⁻³.

Type of costs	Component	CGFB		ABFB	
		Energy arbitrage	T&D support	Energy arbitrage	T&D support
		>10 MW, $t_d = 8h$, $n_y = 250$, $i = 8\%$, $p_c = 0.05$	1-10MW, $t_d = 2h$, $n_y = 400$, $i = 8\%$, $p_c = 0.05$	>10 MW, $t_d = 8h$, $n_y = 250$, $i = 8\%$, $p_c = 0.05$	1-10MW, $t_d = 2h$, $n_y = 400$, $i = 8\%$, $p_c = 0.05$
Capital costs (C_{CAP} kW ⁻¹)	Power part	3456	3456	1340	1340
	Storage part	201	50	204	51
	Manufacturing and other	880	880	880	880
Operational costs ($C_{O\&M}$ kW ⁻¹)		216	216	216	216
Charging costs (C_c kW ⁻¹)		2439	976	2439	976
Lifetime costs (€ kW ⁻¹)		7192	5578	5079	3462
Energy delivered (eq. 6.10, kWh)		19636	7855	19636	7855
LCOS (€ kWh ⁻¹ cycle ⁻¹)		0.366	0.710	0.259	0.441

Importantly, as can be seen in table 6.2, energy storage is cheap for both the CGFB and ABFB (reservoirs with salt water) compared to the power part (stack) which is relatively expensive. From figure 6.2 and from the scenarios in table 6.2 we would expect that the scenario with most emphasis on energy storage would be most cost-effective for the CGFB and ABFB. This is also what the LCOS in table 6.2 shows. For both the CGFB and ABFB, the energy arbitrage scenario outperforms the T&D support scenario significantly. Therefore, when designing a business case for a CGFB or ABFB, it is most profitable to have a relatively large importance on energy storage capacity relative to power. In the calculation of the LCOS a fixed charging price p_c , is assumed

(0.05 € kWh⁻¹). In reality however, the actual charging will probably be lower since the current average electricity price in 2015 in Germany was 0.032 € kWh⁻¹ ¹⁹ (section 6.2.1). This already shows that a charging price of 0.05 € kWh⁻¹ is on the high side. Therefore, the LCOS of storage systems including that of CGFBs and ABFBs might become lower than calculated based on the assumption done by Zakeri et al. ²⁷. The effect of the charging price on the LCOS is shown amongst other variables in section 6.3.2 and section 6.3.3.

6.3.2 Costs comparison of the CGFB and ABFB with other storage systems

Section 6.3.1 estimated the LCOS of both the CGFB and ABFB. It is of interest to compare these values to other known energy storage systems. Figure 6.4 shows the LCOS for different storage technologies compared with the estimated LCOS of the CGFB and ABFB.

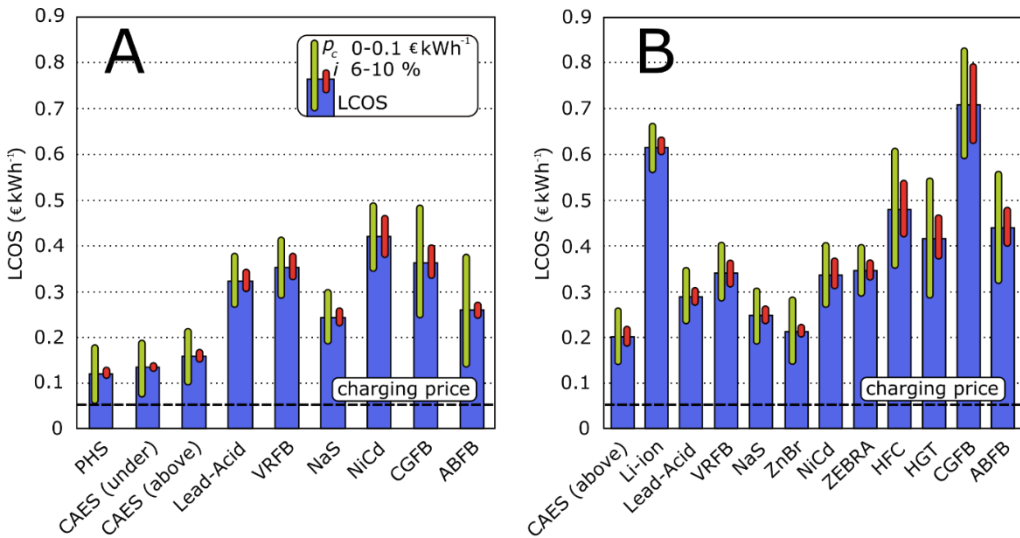


Figure 6.4. Levelized cost of storage (LCOS) for different storage technologies. Graph and data from Zakeri et al. ²⁷. The CGFB and ABFB are added to allow comparison. (A) The LCOS (in blue) for the case of bulk energy storage (250 cycles per year, discharge time of 8 hours, an interest rate of 8% and cost of electricity of 0.05 € kWh⁻¹). (B) The LCOS for the case of T&D support (400 cycles per year, discharge time of 2 hours, an interest rate of 8% and cost of electricity of 0.05 € kWh⁻¹). (A and B) A sensitivity analysis on the charge electricity costs (green bars) and interest rate (red bars) is performed and plotted on top of the LCOS (0-0.1 € kWh⁻¹ for p_e and 6-8% for i).

The data and method of presenting of the LCOS of storage technologies other than CGFB and ABFB is from the work of Zakeri et al. ²⁷. The assumptions which the authors used can be found in table 6.2. The calculated LCOS (blue bars) from section 6.3.1 for the CGFB and ABFB are plotted in figure 6.4A and 6.4B at the right. The assumed charging price is marked as a dashed black line. Figure 6.4A shows the energy arbitrage scenario (high energy capacity) and figure 6.4B shows T&D support scenario (low energy capacity). Considering figure 6.4A (250 cycles y⁻¹, 8 h discharge time) the ranking of LCOS from low to high is PHS < CAES (underground) <

CAES (above ground) < NaS < ABFB < Lead-Acid < Vanadium Redox Flow Battery < CGFB < NiCd. Intuitively one would think that using cheap, abundantly available materials would lead to a low LCOS. In fact, this seems the case looking at this order. The technologies using abundantly available, cheap materials reach the lowest LCOS compared to technologies using less abundant materials (e.g. Nickel, Cadmium, Vanadium). This can be explained by the fact that it is relatively cheap to add extra capacity to this type of system as this does not require expensive materials (water, salt, air). Total capital costs can then be divided by a large amount of energy delivered, thus leading to a low LCOS. The CGFB is an exception however. Although it is cheap to add extra capacity, the LCOS of the CGFB is relatively high. This is caused mainly by the low power density of the system leading to high capital costs even when the costs are spread across a relatively large energy capacity. The effect of this will be explained in section 6.4 in more detail.

Looking at figure 6.4B (400 cycles y^{-1} , 2 h discharge time) the CGFB and ABFB are now amongst the worst LCOS together with the two other water based technologies HFC (hydrogen fuel cell) and HGT (hydrogen gas turbine). The reason that the LCOS of these water based technologies is high at such short discharge times (2 h) is due to the relative high costs for the power part²⁸⁻³⁰. Li-ion technology is performing remarkably poor in this study. A possible reason for this is the high replacement costs²⁷ and also the relatively short discharge period of 2 hours. The green bars on top of the blue bars show the sensitivity to the charging price for electricity p_c . The bottom of the green bar represents the LCOS of the respective technology at a charging price of 0 € kWh⁻¹, while the top of the green bar represents the LCOS at a charging price of 0.10 € kWh⁻¹. From figures 6.4A and 6.4B it is clear that, as expected, the technologies with a relatively poor round trip efficiency η_{RT} (HGT, HFC, CGFB and ABFB) are sensitive to the fluctuating charging costs. For a future with low charging prices p_c , these technologies would gain in competitiveness. Similar to the green bars, the red bars show the effect of a changing interest rate. Especially technologies with relatively high capital costs (NiCd, HGT, HFC, CGFB and ABFB) are affected.

6.4 Sensitivity analysis

From sections 6.3.1 and sections 6.3.2 it became clear that the LCOS for both the CGFB and ABFB are on the high end. To make the CGFB and ABFB commercially more attractive the LCOS should be decreased. This section deals with the question how to do this. By performing a sensitivity analysis on the LCOS study of section 6.3.1. it is possible to identify what parameters can strongly influence the LCOS - and should be focused on during further development - and what parameters do not. Figure 6.5 shows the results of the sensitivity analysis (SA).

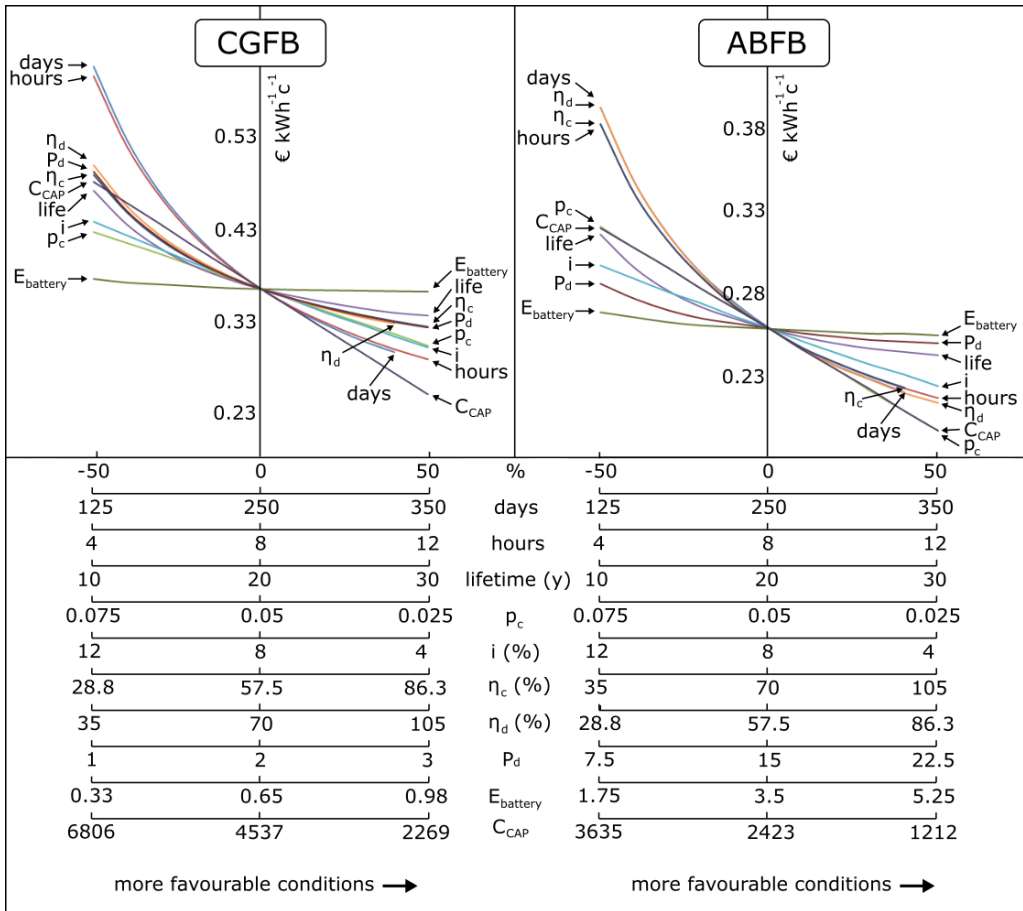


Figure 6.5. Sensitivity analysis on the LCOS (€ kWh⁻¹ cycle⁻¹) of both the CGFB and ABFB. Each varied parameter is given its own x-axis with corresponding values. From top to bottom: days (no. of operating days per year), hours (no. of discharging hours per day), lifetime (years), charging price p_c (€ kWh⁻¹), interest rate i (%), charge efficiency η_c (%), discharge efficiency η_d (%), power density (W m⁻² of membrane), $E_{battery}$ (kWh m⁻³), C_{CAP} (€ kW⁻¹). Note that values for p_c , i and C_{CAP} are mirrored on their axis. In this way all curves move from less favourable conditions (lhs) to more favourable conditions (rhs).

On the left side of figure 6.5 the SA of the CGFB is shown and on the right side the SA of the ABFB. Below both graphs the x-axis shows the change in percentages. Different variables have been changed from -50% to +50% of its original value and the corresponding LCOS is calculated. All the variables which have been changed are listed below the graphs. For easy reference, each variable has been given its own x-axis, so one can see what absolute value corresponds with what total LCOS. For example, the first changed variable is days. The original LCOS calculation accounted for 250 operational days per year (see x-axis below 0%). Decreasing the number of operating days with 50% would mean 125 operating days (see x-axis below -50%). Looking to the graph at this point (of the line with the arrow with 'days' next to it) we can see that this variable has a very large effect. The LCOS increased from 0.366 to 0.608

€ kWh⁻¹ cycle⁻¹. Similarly, increasing the operating days with 40% to 350 days (there are not enough days in a year to increase it with 50%), the LCOS decreases to 0.297 € kWh⁻¹ cycle⁻¹. In the same way the effect of all the other variables can be read from this plot. Since all parameters are changed with the same percentage, the parameters which show the greatest increase or decrease of the LCOS, relatively have the largest impact on the LCOS and are considered the most important ones to research and develop. When reading this graph there is one additional remark to make. To be able to see at once the order of importance of the parameters, some x-axes of parameters are mirrored, so that all graphs move from unfavourable (left) to more favourable conditions (to the right). This is the case for the price of electricity p_c , interest rate i , and the C_{CAP} . For example, in the case of C_{CAP} the value on the left (€ 6806) is not a decrease of 50% in C_{CAP} but an increase of 50% (so 50% less favourable).

Looking at the left plot of figure 6.5 we see that decreasing both ‘days’ and ‘hours’ (number of discharge hours per day) have detrimental effect on the LCOS of the CGFB. This can be explained by considering the denominator of equation 6.9. By decreasing the number of operating days and number of discharge hours, total delivered energy decreases and the LCOS increases. For this reason, we would also expect that decreasing the lifetime of the battery has a similar impact. Yet, looking at the impact of decreasing the lifetime (10 years), although it has a negative effect it is not as negative as changing the number of days or hours. The same effect is seen at the right plot (ABFB). Although all three parameters effectively affect the number of discharge hours (and therefore can be grouped in category ‘total operating hours’), the LCOS does not respond equally. This is explained as follows. First of all, when decreasing the number of discharge hours per day, the needed size of the reservoir is smaller. So, in this case this means that the required C_{CAP} is lower. This explains why decreasing the ‘hours’ has a bit better LCOS then decreasing the ‘days’. Decreasing the lifetime however seems to have the least detrimental effect on the LCOS. This can be explained by the O&M costs. For a decreased lifetime, total O&M costs are lower causing the limited increase of LCOS. More interesting of course is to see how to best improve the LCOS by changing the total number of operating hours. For similar reasons just mentioned, it is of highest interest to first increase the number of operating days. Just increasing the amount of operating days to 350 days, leads to a decrease of LCOS from 0.366 to 0.297 € kWh⁻¹ cycle⁻¹ (CGFB) and from 0.259 to 0.220 € kWh⁻¹ cycle⁻¹ (ABFB). The next best parameter to improve within the category ‘total operating hours’ is the number of operating hours per day (because of increased costs of a larger reservoir) and the least interesting parameter to improve would be the lifetime (because of additional O&M costs). If the market allows for it, it would perfectly possible of course to stack advantages. For example, increasing both the operating days per year and operating hours per day would be beneficial as it would lead to much lower LCOS.

For both the CGFB and ABFB, the capital costs C_{CAP} is a very interesting parameter to improve as it has a major effect on decreasing the LCOS. A decrease of C_{CAP} of 50% yields a LCOS of 0.251 and 0.197 € kWh⁻¹ cycle⁻¹ respectively. There are several ways to decrease the (net) capital

costs. Mass automated manufacturing, finding cheaper components, decrease of material consumption by optimized design and increasing residual value are a few options. There are also indirect ways to decrease the capital costs. One way is to increase the power density of the systems. If the same size stack delivers more power, the capital costs per kW decrease. Figure 6.5 shows the effect of increasing (and decreasing) the power density P_d has on the LCOS of both systems. For the CGFB, the effect is strongest. Increasing the power density by 50% yields a decrease of LCOS from 0.366 to 0.324 € kWh⁻¹ cycle⁻¹. For the ABFB, only a decrease of from 0.259 to 0.250 € kWh⁻¹ cycle⁻¹ takes place. The difference in effect is caused by the low power density of the CGFB (2 W m⁻² of membrane area) compared to the ABFB (15 W m⁻² of membrane area). At low power density the cost of membranes is a relatively large fraction of the total costs. At increasing power density, the membrane costs become a smaller portion and the effect of increasing power density on LCOS diminishes. Another indirect way of decreasing C_{CAP} is the increase in $E_{battery}$. Given a certain amount of discharge hours per day, if more energy is stored in the solutions, a smaller reservoir is required. This means that capital costs would be smaller. Figure 6.5 shows that increasing (or decreasing) $E_{battery}$ has negligible effect. The reason for the insensitivity of the LCOS to $E_{battery}$ is because the reservoirs only make up a small portion of total C_{CAP} . The interest rate is also related to the capital costs C_{CAP} . Figure 6.5 shows the effect of changing the interest rate from 12 to 4%. For the CGFB the LCOS drops from 0.366 to 0.302 € kWh⁻¹ cycle⁻¹ and for the ABFB the LCOS drops from 0.259 to 0.224 € kWh⁻¹ cycle⁻¹. The effect on the LCOS of the ABFB is smaller compared to that of the CGFB because of the ABFB has a smaller C_{CAP} . Considering the effect of the interest rate on total LCOS (a reduction of 0.035 to 0.064 € kWh⁻¹ cycle⁻¹) it is obviously worthwhile to look for investment capital with a lower interest rate.

Considering table 6.2, next to capital costs, total lifetime charging costs represent a significant portion of total lifetime costs. There are different ways to reduce charging costs; reduce charging price p_c , increase charge efficiency η_c , and increase discharge efficiency η_d . Decreasing the p_c by 50% yields an LCOS of 0.304 (CGFB) and 0.197 (ABFB) € kWh⁻¹ cycle⁻¹. Figure 6.5 shows that for the ABFB, p_c is even the parameter with the highest impact on decreasing the LCOS. The reason that p_c is relatively more important to the ABFB, is because the C_{CAP} of the ABFB is smaller (and so is its effect on the LCOS) compared to the C_{CAP} of the CGFB. The fact that p_c has such a high impact on the LCOS of both technologies is caused by the fact that reducing the electricity price not only reduces the LCOS directly, but also indirectly because of the relatively low charge and discharge efficiencies of both systems. A low charge efficiency means that total charge time t_c is longer, leading to higher charge costs. A low discharge efficiency means that relatively little energy is actually derived from the reservoirs. This means that in order to get a kWh of energy out of the battery, a larger reservoir is needed which in turn requires more time to charge, also increasing total charge time t_c . So, both the η_c and η_d have an effect on total charging time t_c , which is also shown by eq. 6.5. Increase of both efficiencies will lead to less energy dissipation and therefore reduced charging costs. Looking at figure 6.5 however, we see that the effect on the LCOS of η_c and η_d (although very similar) are not equal. Figure 6.5 shows

that increasing the discharge efficiency η_d is slightly better than increasing the charge efficiency η_c . This is because η_d affects the energy density of the battery. When the η_d is higher, more chemical energy is converted to electricity from the same volume. This means that the total size of the reservoirs can be decreased if the η_d increases. So, improving η_d is not only interesting from a commercial point of view, it is also of interest when discussing the practicality of the total size of a CGFB system (section 6.7) since it can reduce total size. The exact relation between $E_{density}$ and η_d is given by eq. 6.7.

As this section shows the LCOS can be reduced in multiple ways. Adding up of different types of LCOS discounts is also possible to a certain degree. As example consider the ABFB, where for sake of argument a reduction of 50% the C_{CAP} and an increase of 40% of the operating days is achieved simultaneously. The LCOS would drop from 0.259 to 0.176 € kWh⁻¹ cycle⁻¹. Note however that the individual discounts do not stack completely. So, in the example a total LCOS reduction of 0.259 - 0.176 = 0.083 € kWh⁻¹ cycle⁻¹ is achieved. If discounts would add up completely, based on the individual discounts shown in figure 6.5 a total LCOS reduction of 0.101 € kWh⁻¹ cycle⁻¹ would be expected. Therefore, when adding up discounts, figure 6.5 can be used to make a rough estimation of the overall effect on the LCOS, but one should keep in mind that the actual LCOS reduction is somewhat more modest.

6.5 Making a profit

It is of interest to know when the battery will start to make a profit. From eq. 6.10 it is clear that when the selling price of electricity p_d is equal to the LCOS, the battery breaks even. Looking at figure 6.3, the red dots represent the maximum selling price each day. The average maximum selling price in 2015 was calculated at 0.064 € kWh⁻¹ (section 6.2.1). In the LCOS study a charging price of 0.05 € kWh⁻¹ cycle⁻¹ was assumed. But as we can see from the data in section 6.2.1., the minimum average buying price was 0.00 € kWh⁻¹ cycle⁻¹. If we would assume that both the maximum selling price and minimum buying price would be valid not just for 15 minutes that day but for the whole charge period and discharge period (e.g. 8 hours) it is possible to calculate what the profit would be. For sake of argument, we will also increase the amount of operating days to 365 days, as the prices mentioned are the average values for all days in a year. The resulting profit for the CGFB would be 0.064-0.113= -0.049 € kWh⁻¹ cycle⁻¹ and the profit for the ABFB would be 0.064-0.092= -0.042 € kWh⁻¹ cycle⁻¹). Although not wildly off, it means that by energy arbitrage only (2015 values), it is not yet possible to create a profit with salinity gradient technology. Besides reducing costs or improving performance, another strategy to improve the profitability of a CGFB is to increase revenue. It is widely acknowledged that the profitability of storage systems increases when multiple revenue streams are stacked^{1,14-18,31}. One example could be to use the battery for both energy arbitrage but also to act as reserve on the ancillary market^{13,16,18,31,32}. Operating on the ancillary market is an easy way of increasing revenue as it is cheap to add an extra reservoir in a half-charged state. In this way it possible to act on the ancillary market for both accepting power (for prolonged periods of time, >h) or delivering power (>h). The value for acting on the ancillary market can change depending on

country, time of day and year and other factors. It would be interesting to know an estimate of the revenue however. Staffell et al.¹³ estimates a premium for having reserved power ready of about 22 € kW⁻¹ yr⁻¹ (UK). Drury et al.³² found added value of 20 to 24 € kW⁻¹ yr⁻¹ for CAES systems. Sioshansi et al.³³ estimated the added value between 20-60 € kW⁻¹ yr⁻¹. To know how this extra revenue source affects profit, we assume that for a CGFB and ABFB, the extra revenue is roughly 22 € kW⁻¹ yr⁻¹. To be able to compare this with earlier calculations in the base scenario in section 6.3.1, it is necessary to transform this value. Given the power of the CGFB and ABFB and the number of cycles per year we could express the additional revenue as 0.011 € kWh⁻¹. An estimate of the net profit for the arbitrage + reserve scenario would become -0.038 € kWh⁻¹ cycle⁻¹ (-0.049+0.011) and -0.031 € kWh⁻¹ cycle⁻¹ (-0.042+0.011). Other examples of sources of revenue could be to provide 'black start' service or transmission and distribution investment deferral.

Another aspect worth investigating is the profitability of each cycle on individual basis. It might be for example that some days do not offer low cost charging prices. In that case it might be worthwhile to not use the battery that day. This however would also decrease the amount of operation days which in turn would have a negative effect on the LCOS. Another interesting case would be the case of storage for multiple days. In section 6.2.1 an example scenario was discussed where a windy weekend caused low charging prices for multiple days in a row. In this case it would be of interest to add some (cheap) storage capacity to the battery system to profit from the cheap electricity and sell the electricity the next Monday or Tuesday. However, in this case, also extra capital costs are involved for construction of additional reservoirs causing an increase in LCOS. To calculate the optimal profit a system could make, the used model could be expanded to include the possibility for many different scenarios. Also, until now only historical data were considered and the high and low data points were selected. In reality, the highest and lowest prices are not yet known beforehand and therefore implementation of price forecasting of some sort^{17,34,35} would help to optimize profits.

So far, we have seen that future CGFB and ABFB are not yet capable to make a profit but given that the CGFB and ABFB reach the performance mentioned in table 6.2 and that the membrane prices drop (section 6.3.1) there are certain strategies to improve profitability. The first strategy would focus on reducing costs. In this case focus should be on reducing capital costs, increase the number of operating days per year and operating hours per day and the discharge and charge efficiency of the batteries. Another strategy would be to increase the revenue. Stacking multiple revenue sources is a smart way to increase revenue already today. When designing a business case, it is necessary to remember that extra storage capacity is cheap and power is relatively expensive. Also, multiple day energy arbitrage is a possible way of increasing revenue. As a conclusion to the profitability analysis of a CGFB and ABFB system, we conclude that they are not yet profitable but they have the potential to become profitable if performance is increased, costs reduced and revenues are stacked.

6.6 Sustainability

There are several drivers for the transition to renewable energy sources wind and solar. An important reason is to avoid carbon dioxide emissions and the reduction of other types of air pollution such as NO_x , SO_x or particulates. Also, mining fossil fuels can be damaging to the environment. Next to this, fossil fuels are not evenly dispersed among all nations. Some nations have plenty of fossil resources whereas others have little, leading to political tensions. Also, per unit of produced energy, wind and photovoltaic solar energy consume much less water compared to fossil fuels which could help reducing pressure on scarce water resources ^{36–38}. Assuming the wind turbines and solar panels are produced in a sustainable way themselves, transition to renewable energy sources can tackle these problems. As discussed in chapter 1, electrical energy storage is needed to make a full transition. Obviously, it would make no sense to go through great effort to make energy generation completely sustainable but make energy storage polluting and unsustainable. The importance of sustainability of energy storage systems is already recognized ^{39–50}. This section discusses how a CGFB compares to alternative energy storage systems from a sustainability point of view.

A sustainable energy storage system should at least comply with two demands: It uses little energy and uses sustainable materials. The use of energy is of particular importance to energy storage systems since they will become part of the energy production chain ⁴⁴. After considering all energy costs associated to the production, use and recycling of both the energy generation components (e.g. solar panels) and connected energy storage systems (e.g. batteries), there should be a net surplus of energy produced. The ratio between energy produced over energy consumed by the combined system over its lifetime is known as the energy return on energy invested (EROI). To determine overall EROI, first the EROI of the energy generation itself is determined. Afterwards the energy consumption and capacity of energy storage systems is determined. Finally, both contributions are combined to one overall EROI. Barnhart et al. ⁴¹ analysed 49 different LCA studies on PV panels and wind turbines and found the following average EROIs: photovoltaic wafer technology (8), photovoltaic thin film technology (13), wind on-shore (86) and wind off-shore (89). This means that a photovoltaic solar panel produces eight to thirteen times as much energy during its lifetime than it costs during its entire lifetime. However, these numbers assume no energy storage is connected yet. The overall EROIs for energy generation plus storage will be lower since the addition of a storage device will consume energy but not generate it. To understand the effect of energy expenditure by energy storage systems on overall EROI, another study based on multiple sources by Barnhart et al. ⁵⁰ reports a metric called the energy stored on invested, or ESOI. This is the ratio of energy stored during the lifetime of an energy storage system to the amount of energy required to construct the system. It takes into account the effect of round trip efficiency, cycle life and depth-of-discharge. Table 6.3 shows ESOIs for different well-known energy storage technologies ⁵⁰. Note that these are cradle-to-gate values, so energy for recycling is not taken into account.

Table 6.3. Energy stored on invested (ESOI) for several energy storage technologies. ESOI is ratio of total electrical energy stored by a storage technology over its entire life to the total amount of primary energy it consumed for its production (cradle-to-gate) ⁵⁰.

Type of storage	ESOI (-)
PHS	210
CAES	240
Li-ion	10
Lead-acid	2
VRFB	3
Na-S	6
Zn-Br	3

A high ESOI means that the technology has a low impact on the overall EROI, since it consumes only little energy but can store a lot of energy. Electrochemical storage technologies perform not so well compared to the geological storage technologies (PHS and CAES). Lead acid batteries perform the worst (ESOI of 2). This is mainly because of their poor cycle life and the fact that their production and transport consumes relatively a lot of energy ^{47,50,51}. The other electrochemical technologies are relatively less energy intensive to produce and their round trip efficiency is dominating their ESOI ^{50,51}. Li-ion has a very high energy density and round-trip efficiency which could help explain its relatively high ESOI compared to other electrochemical storage technologies. The lower efficiencies of flow batteries and NaS batteries explain their lower ESOI compared to Li-ion batteries. PHS and CAES perform very well (EROIs of 210 and 240). This is explained by the fact that they use readily available, cheap, abundant materials such as air and water which require very little energy to prepare ⁵⁰.

Now the EROI of solar panels and wind turbines is known and now the ESOI of several storage technologies is known, it is of interest to combine the two metrics for specific use cases in an overall EROI (generation plus storage). Assuming we would like to avoid curtailment of renewable energy and we would like to store all of the surplus energy, the overall EROI is reported in figure 6.6 (Barnhart et al. ⁴¹).

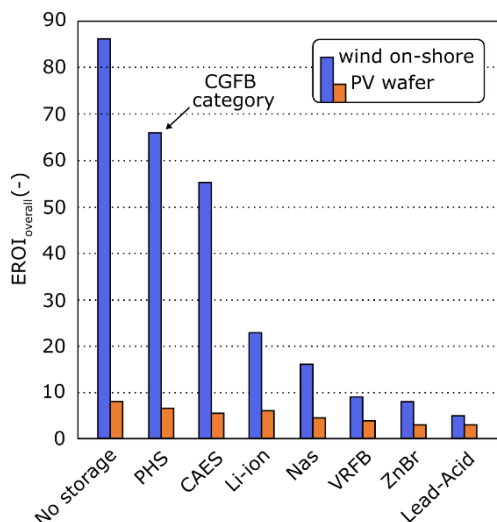


Figure 6.6. Overall EROI for wind or solar combined with several energy storage technologies for the case of no curtailment from Barnhart et al. ⁴¹.

In figure 6.6 both PHS and CAES stand out with the highest overall EROI. This is mainly because the energy costs for producing the storage device are inherently low and they have a long lifetime ^{41,49}. A CGFB is very much like a PHS system. The bulk of the energy storage system comprises large reservoirs of water. Instead of powerful pumps, turbines and a concrete dam, a CGFB has low-pressure pumps and stacks with many membranes. In theory, a CGFB has the potential to reach similarly high overall EROI values as PHS and CAES systems have since it also mainly consists of cheap, readily available (salt) water. High overall EROI values are beneficial to society since surplus energy is converted to wealth and therefore are worth pursuing. For a CGFB to reach its maximum potential in terms of EROI, there are a few important considerations. First of all, the round-trip efficiency of PHS and CAES systems is higher than CGFB systems (chapter 1). A low round trip efficiency results in a direct energy loss and a reduction of overall EROI. From an energy sustainability point of view, round trip efficiency of the CGFB should be improved. Secondly, the lifetime of a storage system is very important for reaching high overall EROI values. Therefore, a CGFB system should have a long lifetime as well. Next to salt water, ion exchange membranes are the most important component of a CGFB system and they determine the lifetime of the CGFB. In commercial electrodialysis plants membranes have lifetimes up to around 5-10 years ⁵²⁻⁵⁴ while the other components (pumps, valves etc.) have lifetimes up to 20 years ⁵². The main reason for membrane degradation in electrodialysis are fouling and scaling ⁵⁵. A CGFB however is a closed system so both fouling and scaling are minimized. The life expectancy of membranes is therefore expected to be much longer. As a result, the lifetime of a CGFB might not be limited by the lifetime of the membranes but by other components. Of course, the only way to know for sure is to test this hypothesis and test a CGFB for a prolonged period of time.

Important to add is the fact that the energetic costs of recycling are not yet taken into account in the determination of the overall EROI reported in figure 6.6. For most energy storage systems, the main materials are obvious (lead in lead-acid batteries, vanadium in VRFB etc.). However, often there are also other materials necessary, for example cobalt or manganese in Li-ion batteries ⁵⁶ or antimony or calcium in lead-acid batteries ⁵⁷. Recycling of these materials inflict heavy energetic costs ⁴⁵. In any case, the actual overall EROI will be somewhat lower than shown in figure 6.6 since in reality also the energetic costs of recycling should be accounted for. Therefore, it is of extra interest to make energy storage systems which are made of homogeneous or easy to separate materials to obtain a high overall EROI. This argument also holds for a CGFB and should be taken into account when selecting materials and designing a system. As an example, the spacers used in (reverse) electrodialysis are often made of a plastic netting (PE, PVC or similar) in which silicone rubber is integrated. It is difficult to recycle this material since it is difficult to separate the silicone rubber from the plastic. It would therefore be better to either switch to a homogeneous spacer made of a single material ⁵⁸ or completely avoid using spacers at all by using profiled membranes ⁵⁹. Another example is the use of carbon electrodes ⁶⁰ instead of titanium electrodes coated with Pt or Ir.

6.7 Size of a CGFB

One of the weak points of a CGFB is its relatively low energy density compared to batteries. This section discusses whether the size of a future CGFB would be manageable. In section 6.2 a future energy density of 0.5 kWh m^{-3} of solution is assumed. Next to the reservoirs also the stacks with membranes require space. The amount of space the power component requires can be calculated by making some assumptions. If the power density is assumed to be 2 W m^{-2} (section 6.2, power per membrane area), the compartment thickness $150 \text{ }\mu\text{m}$ and the membrane thickness $50 \text{ }\mu\text{m}$, a cubic meter can deliver 10 kW . Furthermore, the housing and auxiliary equipment also consume space and it should also be possible for technicians to access the stacks for maintenance. Therefore, assume that the installation becomes twice as large. In that case a power density (power per m^3) of 5 kW m^{-3} is more realistic. We now consider whether these two metrics (0.5 kWh m^{-3} and 5 kW m^{-3}) are acceptable or unrealistic.

As mentioned in chapter 1 and 2, the vast majority of stationary energy storage is provided by PHS systems. Besides these PHS installations, no significant energy storage installations exist yet. Because PHS systems are geographically limited and few in number, not many people are familiar with the size or impact of these installations. To assess whether the size of a CGFB is acceptable to the general public it is of interest to compare the size of a future CGFB with some installation or site that the public is familiar with. Coal plants will disappear in the future and they also resemble the power component of the CGFB in the sense that both transform energy and deliver power. It is therefore interesting to see if the power component of the CGFB would fit on the terrain of current coal plants. The “Amercentrale” ($51^\circ 42' 34'' \text{N}$ $4^\circ 50' 36'' \text{E}$) in Geertruidenberg is a coal fired, 1.2 GW power plant in the Netherlands. The surface area of the coal plant is 450.000 m^2 . This area only includes buildings and the spaces between them, but

does not include the harbour required to deliver the coal, the coal storage areas or surrounding fields. Currently, the highest chimney is 85 meters. People generally prefer the view of trees over chimneys or industrial buildings. Therefore, the height of the power component of the CGFB could be limited to 6 meters so that from a distance the new building would not be visible. The maximum volume available in that case is 2.7 million m³. When fully utilized this equates to a CGFB power component able to deliver 13.5 GW. From this simple calculation it is possible to see that the CGFB would fit on the terrain of the coal plant with ease. The volumetric power density of the CGFB is in a reasonable range and close to that of the coal plant. Most of the volume in a CGFB is taken up by the reservoirs of water however. The most commonly known form of a reservoir of water would likely be a lake. How large would an artificial lake of an CGFB need to be to buffer electric power for the entire Netherlands? In a study by Sternberg et al.⁴³ the authors explore three future case studies where three different countries (Germany, Australia and Ireland) have a high penetration of intermittent energy sources (up to 88%). From these three cases the highest amount of electrical storage required was 22% of the country's total generated electricity. In 2015 the consumption of electricity in the Netherlands was 426 PJ or 118 TWh⁶¹. If we would apply the 22% storage ratio calculated by Sternberg et al. for the Netherlands as a first approximation, we would need to be able to store 26 TWh. Taking into account the number of days in a year and the energy density of a CGFB, the total reservoir size to store this amount of energy would be 142 million m³. Therefore, a reservoir or lake with a size of 4 km by 4 km and 10 m deep would be able to store the surplus energy on a daily basis for the entire Netherlands. Although this is a total volume of appreciable size, it is not an insurmountable issue. So far, we assumed that all storage is done on a diurnal basis. In reality, most energy is produced during the summer months. Therefore, it is of interest to also calculate the size of a similar CGFB in the case it is used for seasonable storage only. The most extreme case would be that all of the previously calculated required energy storage (26 TWh) is necessary for seasonal storage. Energy would be accumulated in a CGFB for six months and subsequently discharged for 6 months. The total required reservoir size would become 72 km by 72 km and 10 m deep. Reasonably this is assessed to be too large. Summarizing, concerning the size of the CGFB, the reservoirs are by far the largest component. Although the CGFB will be spacious, daily storage is within practical range (given we achieved the performance shown in table 6.2) but seasonal storage is not possible until much higher energy densities are achieved. One solution to this issue could be to use the ABFB configuration as introduced in chapter 4. The ABFB reached energy densities up to 1-3 kWh m⁻³, which is 2-6 times higher than the near-future 0.5 kWh m⁻³ of a CGFB. The ABFB system still has plenty of room to be improved in terms of energy density. Also, the power component of an ABFB would consume less space compared to the CGFB. Although it would require continued research effort, considering size, a more mature ABFB system has potential to be used in the future for not only daily storage but for monthly energy storage as well. The safety of large acid and base reservoirs are an important point of attention however. A final option to make the size of a CGFB more acceptable is to blend in the water reservoirs with the environment.

6.8 Concluding remarks

Chapter 2-5 discussed technological aspects of the CGFB and ABFB. This chapter discussed the economic viability, sustainability and size of the CGFB and ABFB. In summary, the technologies are both proven to work. Yet, they suffer from a low coulombic efficiency. In the CGFB this is caused by water transport and in the case of the ABFB this is caused by proton and hydroxyl ion transport. Energy efficiency could be improved dramatically if coulombic efficiency is improved. The energy density of the ABFB is larger compared to the energy density of the CGFB. For both systems, the high capital costs are a drawback. Reduction of capital costs is possible though and the ABFB is from an economical point of view the best option. Charging costs are relatively high, but reduction is possible and the development of charging prices are in favour of both technologies. Yet, although technical performance and costs are very important, the biggest advantage of both technologies are the environmental benefits and their safety. Currently great effort is placed in making energy generation renewable, clean and sustainable. It is only logical that accompanying energy storage should be renewable, clean and sustainable as well and these features are more than just 'nice-to-have'. Especially in that case, concentration gradient (flow) batteries have potential to play a part in the worlds energy transition and continued research and efforts for commercialization are encouraged.

6.9 References

- (1) Lazard. *Lazard's Levelized Cost of Storage Analysis 2.0*; New York, 2016.
- (2) Pawel, I. *Energy Procedia* **2014**, 46, 68–77.
- (3) Gardner, P. *World Energy Resources - E-storage: Shifting from cost to value. Wind and solar applications*; London, 2016.
- (4) Lai, C. S.; McCulloch, M. D. *Arxiv* **2016**.
- (5) Belderbos, A.; Delarue, E.; D'haeseleer, W. In *Energy: Expectations and Uncertainty*; International Association for Energy Economics: Bergen, 2016.
- (6) Obi, M.; Jensen, S.M.; Ferris, J.B.; Bass, R. B. *Renew. Sustain. Energy Rev.* **2017**, 67, 908–920.
- (7) Kost, C.; Mayer, J.; Thomson, J.; Hartmann, N.; Senkpiel, C.; Philipps, S.; Nold, S.; Lude, S.; Saad, N.; Schlegl, T. *Levelized Cost of Electricity Renewable Energy Technologies*; Freiburg, 2013.
- (8) Rastler, D. *Electricity Energy Storage Technology Options A White Paper Primer on Applications, Costs, and Benefits*; Palo Alto, 2010.
- (9) Schoenung, S. M. *Characteristics and Technologies for Long-vs. Short-Term Energy Storage*; Albuquerque, 2001.
- (10) Nasiri, A.; Hamidi, S. A. In *Power Electronics Handbook*; Elsevier, 2018; pp 641–657.
- (11) Nock, D.; Krishnan, V.; McCalley, J. D. *Renew. Energy* **2014**, 71, 396–400.

- (12) Luo, X.; Xia, S.; Chan, K. W. *J. Power Sources* **2014**, *248*, 604–614.
- (13) Staffel, I.; Rustomji, M. *J. Energy Storage* **2016**, *8*, 212–225.
- (14) Lazard. *Lazard's Levelized Cost of Storage Analysis 1.0*; New York, 2015.
- (15) Krishnan, V.; Das, T. *Energy* **2015**, *81*, 175–188.
- (16) Berrada, A.; Loudiyi, K.; Zorkani, I. *Energy* **2016**, *115*, 1109–1118.
- (17) Mc Connell, D.; Forcey, T.; Sandiford, M. *Appl. Energy* **2015**, *159*, 422–432.
- (18) Cho, J.; Kleit, A. N. *Appl. Energy* **2015**, *147*, 176–183.
- (19) EPEX. EPEX Spot Intraday Continuous, DE/AT <https://www.epexspot.com/en/market-data/intradaycontinuous/intraday-table/2015-01-01/DE> (accessed May 29, 2017).
- (20) Varian, H. R. *Intermediate Micro Economics*, 7th ed.; Repcheck, J.; Frenkel, L.; Tedoff, R.; White, A.H.; Awake, M., Ed.; W.W. Norton & Company, Inc.: New York, 2006.
- (21) Rafaj, P.; Kypreos, S. *Energy Policy* **2007**, *35* (2), 828–843.
- (22) Wronski, R.; Fiedler, S.; Jansen, L. *Was strom wirklich kostet*; Hamburg, 2017.
- (23) Zhang, Q.; Weili, T.; Yumei, W.; Yingxu, C. *Energy Policy* **2007**, *35* (8), 4295–4304.
- (24) Roth, I.F.; Ambs, L. *Energy* **2004**, *29* (12–15), 2125–2144.
- (25) Nguyen, K. *Energy* **2008**, *33* (5), 740–746.
- (26) Friedrich, R. et al. *External Costs - Research results on socio-environmental damages due to electricity and transport*; Brussels, 2003.
- (27) Zakeri, B.; Syri, S. *Renew. Sustain. Energy Rev.* **2015**, *42*, 569–596.
- (28) Tsuchiya, H.; Kobayashi, O. *Int. J. Hydrogen Energy* **2004**, *29* (10), 985–990.
- (29) Staffel, I.; Green, R. *Int. J. Hydrogen Energy* **2013**, *38* (2), 1088–1102.
- (30) Elmer, T.; Worall, M.; Wu, S.; Riffat, S. B. *Renew. Sustain. Energy Rev.* **2015**, *42*, 913–931.
- (31) Das, T.; Krishnan, V.; McCalley, J. D. *Appl. Energy* **2015**, *139*, 104–118.
- (32) Drury, E.; Denholm, P.; Sioshansi, R. *Energy* **2011**, *36* (8), 4959–4973.
- (33) Sioshansi, R.; Denholm, P.; Jenkin, T. *Energy Econ.* **2011**, *33* (1), 56–66.
- (34) Kaldellis, J. K. . Z. D. *Energy* **2007**, *32* (12), 2295–2305.
- (35) Sioshansi, R.; Denholm, P.; Jenkin, T.; Weiss, J. *Energy Econ.* **2009**, *31* (2), 269–277.
- (36) Mekonnen, M. M.; Gerbens-Leenes, P. W.; Hoekstra, A. Y. *Environ. Sci. Water Res. Technol.* **2015**, *1* (3), 285–297.
- (37) Mekonnen, M. M.; Gerbens-Leenes, P. W.; Hoekstra, A. Y. *Sci. Total Environ.* **2016**,

1282–1288.

- (38) Buisman, C. J. N. *De mens is geen plaag*, 1st ed.; 20 Leafdesdichten en in liet fan wanhoop: Bornmeer, 2018.
- (39) Larcher, D.; Tarascon, J. M. *Nat Chem* **2015**, 7 (1), 19–29.
- (40) Kang, D. H. P.; Chen, M.; Ogunseitan, O. A. *Environ. Sci. Technol.* **2013**, 47 (10), 5495–5503.
- (41) Barnhart, C. J.; Dale, M.; Brandt, A. R.; Benson, S. M. *Energy Environ. Sci.* **2013**, 6 (10), 2804–2810.
- (42) Dunn, J. B.; Gaines, L.; Sullivan, J.; Wang, M. Q. *Environ. Sci. Technol.* **2012**, 46 (22), 12704–12710.
- (43) Sternberg, A.; Bardow, A. *Energy Environ. Sci.* **2015**, 8 (2), 389–400.
- (44) Poizot, P.; Dolhem, F.; Venkatesha, T. V.; Faber, K.; Kelly, K.; Eckert, C. A.; W. J. Frederick, J.; Hallett, J. P.; Leak, D. J.; Liotta, C. L.; Mielenz, J. R.; Murphy, R.; Templer, R.; Tschaplinski, T.; Ypersele, J.-P. *Energy Environ. Sci.* **2011**, 4 (6), 2003.
- (45) Tarascon, J.-M. *ChemSusChem* **2008**, 1 (8–9), 777–779.
- (46) Denholm, P.; Kulcinski, G. L. *Energy Convers. Manag.* **2004**, 45 (13), 2153–2172.
- (47) Rydh, C. J. *J. Power Sources* **1999**, 80 (1), 21–29.
- (48) Baumann, M.; Peters, J. F.; Weil, M.; Grunwald, A. *Energy Technol.* **2017**.
- (49) Carbajales-Dale, M.; Barnhart, C. J.; Benson, S. M. *Energy Environ. Sci.* **2014**, 7 (5), 1538–1544.
- (50) Barnhart, C. J.; Benson, S. M.; Cui, Y.; McGregor, P. G.; Mulheran, P. a.; Hall, P. J.; Zavadil, B. *Energy Environ. Sci.* **2013**, 6 (4), 1083.
- (51) Rydh, C. J.; Sandén, B. A. *Energy Convers. Manag.* **2005**, 46 (11), 1957–1979.
- (52) Strathmann, H. *Ion-exchange membrane separation processes*; Elsevier: Amsterdam, 2004; Vol. 9.
- (53) Sata, T. *Ion Exchange Membranes: Preparation, Characterization, Modification and Application*; The Royal Society of Chemistry: Cambridge, 2004.
- (54) Strathmann, H. *Desalination* **2010**, 264 (3), 268–288.
- (55) Burn, S.; Hoang, M.; Zarzo, D.; Olewniak, F.; Campos, E.; Bolto, B.; Barron, O. *Desalination* **2015**, 364, 2–16.
- (56) Bresser, D.; Paillard, E.; Passerini, S. In *Advances in Batteries for Medium and Large-Scale Energy Storage*; 2015; pp 125–211.
- (57) Sullivan, J. L. *A Review of Battery Life-Cycle Analysis: State of Knowledge and Critical Needs*; Argonne, 2010.

- (58) Post, J. W. Blue Energy: Electricity Production from Salinity Gradients by Reverse Electrodialysis, Wageningen University, 2009.
- (59) Vermaas, D. A.; Saakes, M.; Nijmeijer, K. *J. Memb. Sci.* **2011**, 385–386, 234–242.
- (60) Vermaas, D. A.; Bajracharya, S.; Sales, B. B.; Saakes, M.; Hamelers, B.; Nijmeijer, K. *Energy Environ. Sci.* **2013**, 6 (2), 643–651.
- (61) Centraal Bureau voor de Statistiek. *Energie; verbruiken producent en prijs naar energiedrager*; Den Haag/Heerlen, 2017.

Summary

The total amount of energy derived from wind turbines and solar panels is rapidly growing. Since these sources of energy are intermittent in nature, supply and demand of energy show an increasing mismatch. To accommodate efficient, large scale use of intermittent renewable energy sources such as wind and sun, energy storage systems are necessary. One of the primary drivers for the increasing use of renewable energy sources is concern about the quality of our environment. Therefore, it is vital that energy storage systems storing sustainable energy, are sustainable themselves. Creating storage systems using abundant, environmentally friendly materials is therefore an important prerequisite for a sustainable energy supply. This thesis aims to explore the potential of the Concentration Gradient Flow Battery (CGFB) as large-scale electricity storage technology. A CGFB stores energy in aqueous solutions of salt (typically NaCl) and uses ion exchange membranes to extract energy from the solutions.

Chapter 1 (Introduction) introduces the need of energy storage. Available energy storage technologies are compared in terms of technical performance but also in terms of safety, environment and political aspects. The CGFB is introduced and explained. Finally, a theoretical background on how a salinity gradient can create a useable voltage across ion exchange membranes is presented.

In **Chapter 2** (The Concentration Gradient Flow Battery as electricity storage system: Technology potential and energy dissipation) a working prototype is constructed and tested. This chapter explains how a CGFB works in more detail and the theoretical maximum energy density of the battery is explored ($\sim 3.2 \text{ kWh m}^{-3}$ for NaCl). The maximum energy density is shown to vary as function of salt concentrations, volume ratio between salt and fresh solution and salt type. A model is introduced which includes the major dissipation factors; internal resistance, water transport and co-ion transport. Experimental work is performed to validate the model. A wide range of salt concentrations (0-3 m NaCl) and current densities (-49 to $+33 \text{ A m}^{-2}$) is chosen. From this work, an optimal working range is identified where the concentrate concentrations preferably do not exceed the 1 m. At higher concentrate concentrations water transport and co-ion transport are found to increase heavily decreasing the energy efficiency of the battery.

In chapter 2 it was shown that the CGFB works best at low ($<1 \text{ m}$) concentrations. At low concentrations, internal resistance and water transport are shown to be the most important dissipation factors. In **chapter 3** (Energy efficiency of a Concentration Gradient Flow Battery at elevated temperatures), a more specific working range (0-1 m) is explored in more detail. Mass transport is measured accurately and an improved experimental approach allows to determine losses by water transport, internal resistance and co-ion transport in more detail. Chapter 3 shows

for both the charge and discharge step the energy efficiency and quantifies the losses at each moment in time. The effect of current density and state-of-charge on power density and energy efficiency is analysed. It is shown that it is not efficient to either completely discharge or charge a CGFB. An optimal working domain is identified ($\Delta m > 0.5$ and $\eta > 0.4$) where the CGFB delivers best performance in terms of energy efficiency (max. discharge η of 72%) and power density (max. discharge power density, 1.1 W m^{-2}). Tests are also performed at different temperatures (10, 25 and 40°C) to measure the effect of temperature on mass transport, internal resistance and power density. Finally, it is shown that water transport is a major issue in the operation of a CGFB where it causes hysteresis (after discharge the battery does not return to its original state), lower efficiency and leads to decreased energy density.

To improve the performance of a CGFB, it is necessary to decrease water transport across the membranes. **Chapter 4** (Tailoring ion exchange membranes to enable low osmotic water transport and energy efficient electrodialysis) introduces modified membranes with a polymer mesh inside with a very small open area (2, 10, 18 and 100% open area). The membranes are prepared by casting an ionomer solution over a polymeric mesh. The material, open area and surface properties of the mesh are changed and the effect on electrical resistance, water transport properties and the efficiency of the charge process are investigated. Comparing a meshed membrane with a homogeneous membrane, the osmotic water transfer coefficient of the meshed membrane is shown to be reduced up to a factor eight. Decreasing the open area of the mesh decreases the water permeability of the membrane but adversely increases electrical resistance. The membranes are tested at different current densities ($5\text{--}47.5 \text{ A m}^{-2}$). Chapter 4 shows that at low current densities ($5\text{--}25 \text{ A m}^{-2}$) the meshed membranes outperform the homogeneous membranes in terms of energy efficiency (at a Δc of 0.7 M , maximum energy efficiency $\eta = 67\%$ for the meshed membranes and $\eta = 50\%$ for the homogeneous membranes). Also, the meshed membranes outperform the homogeneous membranes in terms of diluate yield across all tested current densities (diluate yield of 78–87% for the meshed membranes, 43–76% for the homogeneous membranes). Using a meshed membrane in a CGFB will lead to less issue with hysteresis. In addition, the relation between material and surface property of the mesh and the ionomer resin is investigated. The type of material (PA or PET) is shown to affect the water permeability of the meshed membrane. It is shown that in some cases, compared to a non-treated mesh, a chemically treated mesh (2 M NaOH treatment) yields lower water permeability membranes. Finally, when optimized ion exchange resin is used it is expected that the water permeability can be reduced even further.

Chapter 2 and chapter 3 show that the CGFB is able to store energy in NaCl solutions which has significant environmental benefits. The measured power density is relatively low and energy density is limited because high concentrations cannot be used. In **chapter 5** (Performance of an environmentally benign Acid Base Flow Battery at high energy density) the process is changed to significantly improve power density and energy density while maintaining the environmental benefits. The adjusted system uses three energy storage solutions instead of two and stores most

energy in a proton and hydroxyl ion concentration gradient. To create protons and hydroxyl ions (during charge) and to let the ions recombine to pure water again (during discharge) a bipolar membrane is added. Chapter 5 shows that the theoretical maximum energy density of the adjusted system (called Acid Base Flow Battery, ABFB) is over three times higher than the theoretical maximum of the original CGFB (chapter 2, maximum energy density of the CGFB is $\sim 3.2 \text{ kWh m}^{-3}$ and $\sim 11.1 \text{ kWh m}^{-3}$ for the ABFB). In addition, experiments demonstrate that the ABFB reaches a power density which is about a factor four higher compared to the original CGFB (3.7 W m^{-2} compared to 0.9 W m^{-2} of membrane area). The main dissipation sources are identified and quantified (energy lost by; co-ion transport 39-65%, ohmic resistance 23-45% and non-ohmic resistance 4-5%). The low selectivity of the membranes to protons and hydroxyls lead to a low coulombic efficiency (13-27 %). The ABFB has potential to be improved significantly. Development of better proton blocking anion exchange membranes and hydroxyl ion blocking cation exchange membranes would increase ABFB performance. Also decreasing the thickness of membranes and compartments would increase ABFB performance as it would lead to lower internal resistance energy losses. In addition, higher current densities would help reduce energy losses by co-ion transport.

Chapter 6 (General discussion and outlook) discusses important aspects of CGFB technology from a societal and commercial point of view. Costs and revenues of energy storage systems are very important drivers and can largely determine the chance of success for a storage technology. First a theoretical background of costs calculations for energy storage systems is presented. Next, the costs of future CGFB systems is calculated and compared to competing technologies. In terms of costs, the ABFB outperforms the CGFB system (0.259 and $0.366 \text{ € kWh}^{-1} \text{ cycle}^{-1}$ respectively). Also, possible revenue sources are discussed. Stacking of multiple revenue streams is possible and recommended to increase profitability. Both systems cannot yet generate a profit as costs are too high and single revenue streams are low. However, although difficult, based on the costs calculations, when performance is increased, costs can be reduced and multiple revenue streams are stacked, a commercially viable CGFB/ABFB system is estimated to be feasible. Besides technical and costs aspects, also sustainability of energy storage systems is of major importance. The energy consumption of the production and use of storage systems over their lifetime is analysed and the potential of a CGFB system is discussed. Also, choice in material and system design is discussed. Finally, the size of storage technologies is important. Therefore, the size of a future CGFB system is estimated and discussed with the help of case studies. For diurnal energy storage, the size of a CGFB/ABFB is deemed acceptable given that performance is increased. Seasonal energy storage is not feasible in terms of size without significant technological improvement.

Energy storage with CGFB systems is shown possible. There is a clear need for increased technical performance and reduced costs to create a profitable CGFB. Yet, because of the exciting benefits across different aspects such as safety, environment and politics, CGFB technology is worth continued research.

Samenvatting

De totale hoeveelheid energie afkomstig van windmolens en zonnepanelen groeit hard. Omdat deze bronnen van energie niet constant zijn, komen vraag en aanbod van energie steeds moeilijker bij elkaar. Om efficiënte en grootschalige toepassing van duurzame energie, zoals dat afkomstig is van de wind of zon, mogelijk te maken is energieopslag nodig. Een van de belangrijkste redenen om over te stappen op duurzame energieopwekking, is de zorg om de kwaliteit van ons milieu. Het is daarom van vitaal belang dat energieopslag systemen die duurzame energie opslaan, zelf ook duurzaam zijn. Een energieopslag systeem maken dat veelvoorkomende, milieuvriendelijke materialen gebruikt is daarom een belangrijke vereiste voor een duurzame energievoorziening. Dit proefschrift onderzoekt het potentieel van de concentratie gradiënt flow batterij (CGFB) als grootschalig energieopslag systeem. Een CGFB slaat energie op in waterige zoutoplossingen (meestal NaCl of 'keukenzout') en gebruikt ion uitwisselingsmembranen om de energie uit de oplossingen te onttrekken.

Hoofdstuk 1 (Introductie) introduceert de behoefte aan energieopslag. Beschikbare energieopslag systemen worden met elkaar vergeleken in termen van technische prestaties, maar ook in termen van veiligheid, duurzaamheid en politiek. De CGFB wordt geïntroduceerd en de werking ervan wordt uitgelegd. Tot slot wordt er een theoretische achtergrond gegeven over hoe een concentratieverschil een bruikbaar voltage kan opleveren met behulp van een ion uitwisselingsmembraan.

In **hoofdstuk 2** (The Concentration Gradient Flow Battery as electricity storage system: Technology potential and energy dissipation) wordt een werkend prototype gebouwd en getest. Dit hoofdstuk legt in meer detail uit hoe een CGFB werkt en de theoretisch maximaal haalbare energiedichtheid wordt onderzocht ($\sim 3,2 \text{ kWh m}^{-3}$ voor NaCl). Er wordt aangetoond dat de maximale energiedichtheid varieert met de gekozen zoutconcentraties, ratio van de volumes van het zoete en zoute water en zouttype. Een model wordt geïntroduceerd dat de belangrijkste bronnen van energieverlies beschrijft, namelijk interne weerstand, watertransport en co-ion transport. Experimenteel werk wordt uitgevoerd om het model te valideren. Voor dit experimenteel werk wordt een uitgebreid bereik in zoutconcentraties (0-3 m NaCl) en stroomdichtheden (-49 tot $+33 \text{ A m}^{-2}$) gebruikt. Uit de resultaten van dit werk worden optimale proces omstandigheden geïdentificeerd waarbij de zoutconcentratie bij voorkeur niet hoger is dan 1 m. Bij hogere zoutconcentraties stijgt het ongewenste watertransport en co-ion transport en daalt de efficiëntie van de batterij ernstig.

In hoofdstuk 2 was aangetoond dat de CGFB het beste werkt bij relatief lage ($<1 \text{ m}$) zoutconcentraties. Het hoofdstuk liet ook zien dat bij lage zoutconcentraties, de interne

weerstand en het ongewenste watertransport de belangrijkste bronnen van energieverlies zijn. In **hoofdstuk 3** (Energy efficiency of a Concentration Gradient Flow Battery at elevated temperatures), wordt een meer specifiek bereik in concentratie verschil (0-1 m) onderzocht. Massatransport wordt nauwkeurig gemeten en een verbeterde experimentele aanpak staat toe om de energieverliezen veroorzaakt door watertransport, interne weerstand en co-ion transport te meten met grotere nauwkeurigheid. Hoofdstuk 3 laat voor zowel de laad- als ontladestap de energie efficiëntie zien en kwantificeert de energieverliezen op ieder moment in de tijd. Het effect van de stroomdichtheid en state-of-charge van de batterij op vermogensdichtheid en energie efficiëntie wordt geanalyseerd. Er wordt aangetoond dat het niet efficiënt is om een CGFB compleet op te laden of om een CGFB compleet te ontladen. Optimale proces condities worden geïdentificeerd ($\Delta m > 0,5$ en $\eta > 0,4$) waar de CGFB het beste presteert in termen van energie efficiëntie (max. ontlad η van 72%) en vermogensdichtheid (max. ontlad vermogensdichtheid, $1,1 \text{ W m}^{-2}$). Ook worden experimenten uitgevoerd bij verschillende temperaturen (10, 25 en 40°C) om het effect van temperatuur op massa transport, interne weerstand en vermogensdichtheid te onderzoeken. Tot slot wordt aangetoond dat watertransport een belangrijk probleem is in de operatie van een CGFB omdat het hysteresis (na een volledige laad- en ontlad cyclus keert de CGFB niet terug naar zijn oorspronkelijke staat), een lagere energie efficiëntie en een lagere energiedichtheid veroorzaakt.

Om de prestaties van een CGFB te verbeteren is het nodig om watertransport door het membraan te verminderen. **Hoofdstuk 4** (Tailoring ion exchange membranes to enable low osmotic watertransport and energy efficient electrodialysis) introduceert aangepaste membranen waarin een kunststof net met hele kleine openingen (2, 10, 18 en 100% open oppervlak) is aangebracht. De membranen worden bereid door ionomeer oplossing uit te gieten over het kunststof net. Het materiaal, open oppervlak en de chemische oppervlakte eigenschappen van het kunststof net worden gevarieerd en het effect ervan op de elektrische weerstand, watertransport eigenschappen en de efficiëntie van de oplaad stap wordt onderzocht. Er wordt aangetoond dat het aangepaste membraan in vergelijking met een homogeen membraan (100% open oppervlak), de osmotische watertransport coëfficiënt kan verlagen met een factor 8. Het kleiner maken van het open oppervlak van het kunststof net leidt tot een lagere water permeabiliteit maar heeft ook nadelig effect op de elektrische weerstand van het membraan. De membranen worden getest bij verschillende stroomdichtheden ($5\text{-}47,5 \text{ A m}^{-2}$). Hoofdstuk 4 laat zien dat bij lage stroomdichtheden ($5\text{-}25 \text{ A m}^{-2}$), de aangepaste membranen beter presteren dan de homogene membranen in termen van energie efficiëntie (bij een Δc van 0.7 M, maximale energie efficiëntie $\eta = 67\%$ voor de aangepaste membranen en $\eta = 50\%$ voor de homogene membranen). Daarnaast tonen de aangepaste membranen ook een hogere diluaat opbrengst in vergelijking met de homogene membranen (diluaat opbrengst van 78-87% voor de aangepaste membranen, 43-76% voor de homogene membranen). Het gebruik van een aangepast membraan in een CGFB leidt tot minder problemen met hysteresis. De relatie tussen het materiaal en de oppervlakte eigenschappen van het kunststof net en het ionomeer materiaal wordt ook onderzocht. Het type materiaal (PA of PET) heeft effect op de water permeabiliteit van het aangepaste membraan. Er

wordt aangetoond dat, in vergelijking met een homogeen membraan, in sommige gevallen een chemisch behandeld kunststof net (2 M NaOH behandeling) een aangepast membraan oplevert met een lagere water permeabiliteit. Tot slot verwachten we dat als de ionomeer oplossing wordt geoptimaliseerd, de water permeabiliteit van de aangepaste membranen nog verder omlaag kan worden gebracht.

Hoofdstuk 2 en hoofdstuk 3 laten zien dat de CGFB in staat is om energie op te slaan in NaCl oplossingen wat significante milieuvoordelen met zich meebrengt. De gemeten vermogensdichtheid is relatief laag en de energiedichtheid is beperkt omdat de hoge zoutconcentraties niet benut kunnen worden. In **hoofdstuk 5** (Performance of an environmentally benign Acid Base Flow Battery at high energy density) wordt het proces aangepast om de vermogensdichtheid en energiedichtheid significant te verbeteren terwijl de milieuvoordelen behouden blijven. Het aangepaste systeem gebruikt drie oplossingen in plaats van twee en slaat het merendeel van de energie op in een verschil in concentratie van protonen en hydroxyl ionen. Om protonen en hydroxyl ionen te kunnen maken uit water (tijdens de oplaadstap) en om ze weer gecontroleerd te kunnen laten recombineren tot water (tijdens de ontladstap), wordt een bipolair membraan toegevoegd aan het systeem. Hoofdstuk 5 laat zien dat de theoretisch maximaal haalbare energiedichtheid van het aangepaste systeem (genaamd Zuur Base Flow Batterij, of Acid Base Flow Battery, ABFB) meer dan drie keer zo hoog is dan de originele CGFB (hoofdstuk 2, maximale energiedichtheid van de CGFB is $\sim 3,2 \text{ kWh m}^{-3}$ en $\sim 11,1 \text{ kWh m}^{-3}$ voor de ABFB). Ook laten experimenten zien dat de ABFB een vermogensdichtheid bereikt die ongeveer een factor vier hoger is in vergelijking met de originele CGFB (3.7 W m^{-2} in vergelijking met 0.9 W m^{-2} membraan oppervlak). De belangrijkste bronnen van energieverlies worden geïdentificeerd en gekwantificeerd (energie verloren door: co-ion transport 39-65%, ohmse weerstand 23-45% en niet-ohmse weerstand 4-5%). De lage selectiviteit van de membranen tegen protonen en hydroxyl ionen leidt tot een lage coulombische efficiëntie (13-27 %). De ABFB kan potentieel aanzienlijk verbeterd worden. Het ontwikkelen van betere, protonen blokkerende anion uitwisselingsmembranen en hydroxyl ion blokkerende kation uitwisselingsmembranen zou een belangrijke bijdrage kunnen leveren aan het verbeteren van de prestaties van de ABFB. Ook het reduceren van de dikte van de membranen en compartimenten kan leiden tot verbeterde ABFB prestaties omdat het leidt tot een lagere interne weerstand. Daarnaast helpen de hogere stroomdichtheden om de energieverliezen door co-ion transport tegen te gaan.

Hoofdstuk 6 (General discussion and outlook) bespreekt belangrijke aspecten van de CGFB-technologie vanuit een maatschappelijk en commercieel oogpunt. Kosten en opbrengsten van energieopslag systemen zijn belangrijke factoren die grotendeels de kansen op succes van een energieopslag systeem kunnen bepalen. Eerst wordt een theoretische achtergrond van kostenberekeningen van energieopslagsystemen gegeven. Daarna worden de kosten van een toekomstig CGFB systeem en ABFB systeem uitgerekend en worden deze kosten vergeleken met concurrerende technologieën. In termen van kosten, presteert de ABFB beter dan de CGFB

(0,366 en 0,290 € kWh⁻¹ cyclus⁻¹ respectievelijk). Ook worden mogelijke bronnen van opbrengst besproken. Het opeenstapelen van meerdere bronnen van opbrengsten is mogelijk en wordt aangeraden om de winstgevendheid te vergroten. Beide systemen kunnen nog geen winst maken omdat de kosten te hoog zijn en de opbrengsten van opbrengstenbronnen te laag is. Toch, alhoewel erg moeilijk, lijkt het op basis van de kostenberekeningen mogelijk om een commercieel haalbare CGFB/ABFB te maken indien de prestaties van de batterijen omhoog klimt, de kosten nog verder kunnen worden gereduceerd en meerdere opbrengstenbronnen worden gestapeld. Naast de technische en commerciële aspecten is ook de duurzaamheid van energieopslag systemen van groot belang (hoofdstuk 1). Het verbruik van energie gedurende de productiefase en gebruiksfase van verschillende opslagsystemen gedurende de complete levensduur wordt geanalyseerd en het potentieel van de CGFB met betrekking hiertoe wordt besproken. Daarnaast wordt ook de materiaalkeuze en systeemontwerp besproken. Tot slot is ook het formaat van de batterij van belang. Het formaat van een toekomstig CGFB systeem wordt geschat en besproken aan de hand van casestudies. Voor dagelijkse energieopslag wordt het formaat van een CGFB/ABFB acceptabel geacht, gegeven dat de prestaties van de batterij worden verbeterd. Seizoensopslag lijkt nog niet mogelijk in termen van formaat zonder significante verbetering in de technologie.

Energieopslag met CGFB systemen is aangetoond mogelijk. Er is een duidelijke behoefte aan verbeterde technologische prestaties en kostenreductie om een winstgevende CGFB te maken. De mogelijk grote voordelen in termen van veiligheid, duurzaamheid en politiek maakt het waard om CGFB-technologie verder te ontwikkelen.



*Netherlands Research School for the
Socio-Economic and Natural Sciences of the Environment*

D I P L O M A

For specialised PhD training

The Netherlands Research School for the
Socio-Economic and Natural Sciences of the Environment
(SENSE) declares that

***Willem Johannes van
Egmond***

born on 27 August 1984, in Leiden, the Netherlands

has successfully fulfilled all requirements of the
Educational Programme of SENSE.

Wageningen, 11 April 2018

the Chairman of the SENSE board

Prof. dr. Huub Rijnaarts

the SENSE Director of Education

Dr. Ad van Dommelen

The SENSE Research School has been accredited by the Royal Netherlands Academy of Arts and Sciences (KNAW)



K O N I N K L I J K E N E D E R L A N D S E
A K A D E M I E V A N W E T E N S C H A P P E N



The SENSE Research School declares that **Mr Willem Johannes van Egmond** has successfully fulfilled all requirements of the Educational PhD Programme of SENSE with a work load of 48.6 EC, including the following activities:

Specialised PhD Courses

- o Bioreactor Design (2016)
- o Environmental research in context (2016)
- o Research in context activity: 'Presenting and communicating research outcomes on various occasions to a wide audience of stakeholders, course participants, parliament and cabinet members' (2015-2017)

Other PhD and Advanced MSc Courses

- o Water Treatment, Wageningen University (2015)

Management and Didactic Skills Training

- o Supervising three MSc students with thesis entitled 'The Blue Battery; Using mixed ion exchange resin in the diluted compartment to decrease the ohmic resistance of the diluted compartment' (2015), 'Salinity gradient energy storage; Quantification of the influence of temperature on salinity gradient flow battery performance' (2016) and 'Blue Energy; Waste heat conversion in electrical power (2016)
- o Organisation of 7th European Summer School Electrochemical Engineering (2015)
- o R&D at start-up company AquaBattery B.V. (2015-present)

Selection of Oral Presentations

- o *Large scale electricity storage in salinity gradients*. Members Only Congress Wetsus, 23 January 2014, Leeuwarden, The Netherlands
- o *Blue Energy – Gebruik van zoutgradiënten voor electriciteitsproductie en andere nieuwe applicaties*. Het Technisch Symposium, 8 May 2015, Leiden, The Netherlands
- o *Energy storage in NaCl solutions – The Concentration Gradient Flow Battery for grid energy storage*. Wetsus Congress, 4 October 2016, Leeuwarden, The Netherlands

Awards

Best presentation: *Energy storage in NaCl solutions – The Concentration Gradient Flow Battery for grid energy storage*. STREAM Conference, 11 July 2017, Leeuwarden, The Netherlands.

SENSE Coordinator PhD Education

Dr. Peter Vermeulen

Dankwoord

‘Met de kennis van nu, zou je het weer doen?’ vraagt mijn moeder over mijn onderzoek gedurende de afgelopen vier jaar. Het antwoord is zonder twijfel Ja. Meer dan 1500 dagen, 50.000 km rijden en 600 opgewarmde maaltijden verder kom ik tot de conclusie dat hoewel er moeilijke momenten waren, ik met zo ontzettend veel plezier heb gewerkt aan dit project dat ik het direct over zou doen. Ik heb erg veel geleerd, gedaan en gelachen en bovendien heb ik veel ideeën vrijelijk uit kunnen proberen in het laboratorium, een van mijn favoriete tijdsbestedingen. Dit is het moment voor mij om een flink aantal mensen te bedanken.

Allereerst wil ik mijn copromotor bedanken. Bert, ontzettend bedankt voor je input, creativiteit, kennis, geduld en vasthoudendheid in het streven naar kwaliteit. Het is die vasthoudendheid die mij – toegegeven – kan frustreren maar die uiteindelijk keer op keer mijn werk tot een hoger niveau tilt. Bedankt voor de ontelbare uren overleg, WhatsAppjes en leuke brainstormsessies. Ik zou geen andere begeleider gewild hebben. Michel, wat ben ik blij dat ik ook jou heb leren kennen. Je bent een wandelende elektrochemische databank. Ontzettend bedankt voor je kennis, je praktische hulp, input en humor. Ik vond het ook heel bijzonder om je enthousiasme voor onze technologie te delen. Ook wil ik heel graag Slawek bedanken. Slawek, je oog voor detail, je geduld, doorzettingsvermogen, concrete verbeteringen en aanpakmentaliteit hebben mij erg geholpen bij het schrijven van mijn papers. Ook dankzij jou heb ik een groei doorgemaakt in mijn schrijfvaardigheid. Bovendien ben je ook nog eens een hele geschikte kerel. Ik wil graag Wetsus en Wageningen Universiteit bedanken. Cees, bedankt dat je mijn onderzoek hebt mede mogelijk gemaakt en mij de mogelijkheid hebt geboden om voor Wageningen Universiteit en Wetsus te werken. Ik ben ontzettend blij dat Wetsus bestaat en blij met de gemoedelijke sfeer die er hangt. Ernst, Harm, Jan, Harry, Wim, Jan-Jurjen, Piet, John, Rienk, Gerrit, Wiebe en alle overige staf, grote dank voor jullie input, behulpzaamheid, ondersteuning en vakmanschap. Bedankt voor jullie geduld en bereidheid om te helpen als ik weer eens sneller vooruit wilde. Ook mijn studenten verdienen een eervolle vermelding. Tom, Ulrich, Laura, César, Imtisal, Frederico, Lini en Jan, dank voor jullie bijdrage aan mijn onderzoek. Ik was verbaasd over jullie grote inzet, zelfstandigheid en interesse in het onderwerp. Een enkeling van jullie werd zelfs met regelmaat ’s avonds laat uit het kantoor gezet door de beveiliging die het pand wilde afsluiten. Maar weinig collega’s kunnen zeggen dat ze met dergelijk gemotiveerde studenten hebben mogen werken. Ook wil ik de bedrijven en haar werknemers binnen het thema ‘Blue Energy’: Alliander, REDstack, Fujifilm, A. Hak, Landustrie en W&F technologies bedanken. Wat bijzonder om na al die jaren nog steeds zoveel interesse en inzet te zien. Dank jullie voor de kritische vragen, suggesties, goodwill en alle hulp. Het heeft mijn onderzoek beter gemaakt. Daarnaast wil ik iedereen binnen AquaBattery bedanken, Jan, David, Emil, Jiajun, Maurits, Juan-

Sebastian, Jelle, wat een avontuur. Ook wil ik mijn lieve vrouw Elise bedanken. Ik ben veel nachten van huis geweest, kwam vaak erg laat thuis, was veel vermoeid en soms gefrustreerd. Wat ben ik dankbaar voor je geduld en voor je vele ‘care-packages’ – lees maaltijden in bakjes –!. Mam, pap, Janet, bedankt dat jullie er zijn. Tot slot wil ik God danken voor Zijn goedheid, alles wat Hij mij heeft geschonken en dat Hij er altijd voor mij is.

This work was performed in the cooperation framework of Wetsus, European Centre of Excellence for Sustainable Water Technology (www.wetsus.nl). Wetsus is co-funded by the Dutch Ministry of Economic Affairs and Ministry of Infrastructure and Environment, the Province of Fryslân and the Northern Netherlands Provinces. Funding was also provided by the participants of the research theme “Blue Energy”.

Cover by Jan Willem van Egmond

This thesis is printed using environmental friendly ink and FSC certified paper

